Medical Terahertz Pulsed Imaging in Reflection Geometry

HUANG, Shengyang

A Thesis Submitted in Partial Fulfillment of the

Requirements for the Degree of

Doctor of Philosophy

in

Electronic Engineering

The Chinese University of Hong Kong

September 2009

ProQuest LLC.
789 East Eisenhower Parkway
P.O. Box 1346
Ann Arbor, MI 48106 - 1346

Abstract

The terahertz band lies between the microwave and infrared regions of the electromagnetic spectrum. This radiation has very low photon energy and thus it does not pose any ionization hazard for biological tissues. It is strongly attenuated by water and very sensitive to water content. Unique absorption spectra due to intermolecular vibrations in this region have been found in different biological objects. These distinctive advantages over other techniques like x-ray and ultrasound make terahertz very attractive for medical applications. In fact, terahertz imaging and spectroscopy techniques have only a history of about two decades for a previous lack of terahertz sources. Due to strong water absorptions, terahertz radiation cannot penetrate very far into biological samples with high water content. The majority of the limited reported terahertz studies in biomedicine were carried out in transmission mode. In contrast, imaging and spectroscopy in reflection mode remain even less mature. However, if terahertz imaging is to be used in the future for medical purposes, it is likely to be more feasible if conducted in reflection geometry.

Consequently, the objective of this thesis was to develop systematic methods to improve the accuracy of terahertz pulsed imaging based on theoretical calculations, and to further verify them with experimental results. Meanwhile, we have initiated pilot studies for tissue characterization. First of all, algorithms were refined to analytically extract the frequency dependent optical parameters including refractive index and absorption coefficient from measured electric fields. It incorporated the angle of incidence to improve the calculations.

Optical parameters are very sensitive to background noise and other artefacts. The system performances were evaluated and a 5% variation over the raster scanning plane was observed. By comparing the distribution of the intensities measured from homogeneous samples, a new data acquisition protocol and a general data processing algorithm were proposed to solve this problem. With this improvement, the system's percentage variation over different locations was successfully reduced by a factor of 3. To further study the impact of noise on the calculation of optical parameters, simulation work was performed and a method was developed to quantitatively assess the accuracy from the dynamic ranges of the sample signal. Ringing artefacts are introduced by the lower surface of the sample window required in many reflection imaging and spectroscopy systems, thus we devised a new baseline approach to account for this effect. The straightforward protocol in our method

enables the reference measurements to be taken reliably and easily such that ringing effects can be determined and excluded in our calculations.

Based on theoretical calculations and experiments, the time of flight formula in our system was established, by which the relationship between layer thickness, optical delay and the refractive index was correctly given. For those samples with layered structures, the thickness information can be readily determined with this formula. In this regard, an *in vivo* experiment with Tegaderm plaster and the palm of a hand was designed to study the feasibility for burn wound assessment using this time of flight technique.

Finally, to better understand the origin of image contrast as well as for starting potential medical applications, terahertz imaging was applied to study healthy and diseased biological tissues. To this end, protocols and methods were designed for facilitating THz measurements of fresh tissue samples. Using them we first investigated the ability of TPI to differentiate between healthy tissue types from laboratory rats. Parameters in both the time domain and frequency domain were quantified, including their percentage differences and the 95% confidence intervals. Two sample *t*-tests were used to assess their statistical significance. In the second step, TPI was further employed to quantitatively characterize the difference between healthy and diseased liver samples. Histological examinations were performed to confirm and understand the differences.

In summary, we have refined the algorithms for extracting the optical parameters in reflection geometry. The system performance has been evaluated and several original approaches have been developed to improve the accuracy of the calculation. Thirdly, the time of flight equation in our system has been established and it can be further employed to characterize samples with layered structure. Finally, healthy and diseased tissues have been investigated and protocols for fresh tissue measurements have been studied.

摘要

太赫茲（THz）波是一種介於遠紅外和微波之間的電磁波譜，其頻率範圍爲 0.1—10THz。THz 技術是近年來發展起來的一個新型的交叉前沿領域，其重要學術價值已得到國際科學界公認。

THz 輻射光子能量極低（1THz 約 4.2eV），因而不會對人或生物有機體造成電離傷害。THz 波極易被水等極性液體吸收，對生物組織體內的水成份非常敏感。THz 相幹檢測技術能夠同時獲取樣品與 THz 脈衝波相互作用產生的電場強度和相位信息隨時間的分佈，進而能精確提取樣品在 THz 波段的光學、電學及介電特性。此外，生物大分子的振動和轉動頻率均在 THz 波段，因而不同分子結構在 THz 波段會呈現不同的吸收譜。上述這些特質使得 THz 波非常適合用於醫學診斷與成像。由於水對 THz 波的強吸收特性，THz 波在生物活體組織中穿透深度比較有限，目前絕大多數研究都集中在利用相對成熟的 THz 透射技術來分析生物組織切片。而 THz 技術最終能被用於臨床檢測，最可行的方式將是通過檢測反射波，然而，目前 THz 反射成像技術相關方面的研究還十分欠缺。

因而，本論文的主要目的將致力於完善 THz 反射成像理論與方法，在現有基礎上進一步探索 THz 成像技術在生物組織檢測方面的應用，將 THz 成像技術向靈床运用方向推進。本文首先對已有光學參數提取算法進行了改進，在算法中引入了 THz 波入射角，給出了折射率和吸收率的解析表達。測試表明，修正後算法獲取結果與其它標準數據具有很好的一致性。

本文對所用實驗設備進行了有效評估並提出了新的算法來減小噪聲影響。通過檢測 THz 信號的時域強度，發現設備在光柵掃描過程中具有明顯的波動，爲此，本文改進了實驗方案中參照（reference）信號和基線（baseline）信號的測量方法，在改進算法中，將掃描獲取的樣品信號，參照信號和基線信號在位置上嚴格對齊，此新算法有效地將系統波動降低了三倍。此外，論文通過仿真實驗研究了噪聲對光學參數計算結果的影響，並提出了一種新方法，利用樣品信號動態範圍來評估光學參數計算誤差。在反射系統設備中，被測樣品一般都放在一個石英窗口上，該石英窗口的下表面產生的反射波會對主反射波（即來自樣品與石英窗口分界面的反射波）造成幹擾，即基線僞影 (baseline artefacts)。由於這類基線僞影不能被直接檢測，其影響在以往算法中沒有被有效解決。本文通過對水和空氣的測量，提出了一種新的算法來估算系統中的基線僞影。運用這種新算法，所檢測的樣品光學參數精度得到了顯著提高。

在 THz 反射成像中，飛行時間差技術（TOF， time of flight）能夠被用來獲取樣品內部的結構信息，本文對此進行了研究。首先，通過理論推導與實驗測試，在 TOF 算法中修正了脉衝時

間差、折射率及深度信息之間的關係，并對具有層結構的樣品進行了研究，獲取了樣品不同層內的深度和折射率信息。此外本文還設計了實驗來研究 TOF 技術在皮膚燒傷領域內的應用前景。

本文開展了 THz 成像在檢測生物組織應用實驗，在實驗中系統研究了測量新鮮組織的樣品準備、數據採集及數據處理等有關實驗方案。通過測量一系列老鼠器官組織樣品，分析了 THz 反射波的時域和頻域參數。統計分析表明 THz 成像技術能有效地鑒別這些不同組織，所獲取差異具有可靠的顯著性。此外，本文還檢測了正常肝臟組織和肝硬化組織，數據顯示，硬化區域與正常肝組織相比具有較高的折射率和吸收率。

綜上所述，本文對已有 THz 反射成像理論及數據處理方案進行了修正，并建立了幾種新的算法來提高設備的測量精度。在此基礎上，開展了 THz 成像檢測技術在生物組織內的應用研究。

Acknowledgments

I am greatly indebted to my supervisor Prof. Emma Pickwell-MacPherson. Her continuous support and her input in this work are invaluable. It has been a pleasure to work with her.

I am also greatly indebted to my supervisor Prof. Yuan-ting Zhang for his guidance and support throughout this study.

I am very grateful to Dr. Yi-xiang Wang at the Department of Diagnostic Radiology and Organ Imaging. He has offered me a lot of invaluable help with my experiments and paper writing.

I would like to thank Dr. Vincent P Wallace at University of Western Australia for his insightful suggestions to my thesis proposal and my papers. Special thanks also to Mr. Philip C. Ashworth from Cavendish Laboratory for his collaboration.

I am also grateful to Dr. Yanlin Sun, Dr. Xiangyan Chen and Mr. Jacky Wong for their help in sample preparation.

I would like to thank all the colleagues in JCBME for their help, especially Ms. Yiwen Sun, Ms. Kanis Kan and Dr. Yang Chen.

Finally I would like to thank my family and friends for their support.

Table of contents

List of abbreviations

AC	Absorption Coefficient
CW	Continuous Wave
DR	Dynamic Range
EM	Electromagnetic Spectrum
EC	Extinction Coefficient
FDHM	Full Duration at Half Maximum
FWHM	Full Width at Half Maximum
HCC	Hepatocellular Carcinoma
KHS	Krebs-Henseleit Solution
MAD	Maximum Absolute Differences
MPD	Maximum Percentage Difference
RI	Refractive Index
RMS	Root Mean Square
SC	Stratum Corneum
SNR	Signal to Noise Ratio
STD	Standard Deviation
THz-TDS	Terahertz Time Domain Spectroscopy
TPI	Terahertz Pulsed Imaging
TPS	Terahertz Pulsed Spectroscopy

List of figures

List of tables

List of publications

Journal articles

- **S.Y. Huang**, P. C. Ashworth, K. W. C. Kan, Y. Chen, V. P. Wallace, Y. T. Zhang, and E. Pickwell-MacPherson, "Improved sample characterization in terahertz reflection imaging and spectroscopy," *Optics Express,* vol. 17, pp. 3848-3854, 2009.
- **S. Y. Huang**, Y. X. J. Wang, D. K. W Yeung, A. T. Ahuja, Y. T. Zhang, and E. Pickwell-MacPherson, "Tissue characterization using terahertz pulsed imaging in reflection geometry," *Physics in Medicine and Biology,* vol. 54, pp. 149-160, 2009.
- E. Pickwell-MacPherson, **S. Y. Huang**, K. W. C. Kan, Y. W. Sun, and Y. T. Zhang, "Recent Developments of Terahertz Technology in Biomedicine," *Journal of Innovation in Optical Health Sciences,* vol. 1, pp. 29-44, 2008.

Conference articles:

- **S. Y. Huang**, Y. X. Wang, J. Yu, A. T. Ahuja, V. P. Wallace, Y. T. Zhang, and E. Pickwell-Macpherson, "Terahertz pulsed imaging of liver cirrhosis," Accepted by *34rd International Conference on Infrared, Millimeter and Terahertz Waves*, Busan, 2009.
- **S. Y. Huang**, Y. X. Wang, D. K. W. Yeung, V. P. Wallace, Y. T. Zhang, and E. Pickwell-MacPherson, "Characterizing rat tissue samples using terahertz pulsed imaging," in *Proc. 33rd International Conference on Infrared, Millimeter and Terahertz Waves*, Vols. 1 and 2, pp. 642-642, California, 2008.
- **S. Y. Huang**, E. MacPherson, and Y. T. Zhang, "A new data processing approach to reduce variations in terahertz pulsed imaging," in *Proc. 5th International Summer School and Symposium on Medical Devices and Biosensors*, pp. 243-245, Hong Kong SAR, 2008.
- **S. Y. Huang**, E. Macpherson, and Y. T. Zhang, "A feasibility study of burn wound depth assessment using terahertz pulsed imaging," in *Proc. 4th IEEE/EBMS International Summer School and Symposium on Medical Devices and Biosensors*, pp. 111-114, Cambridge, 2007.
- E. Pickwell-MacPherson, **S. Y. Huang**, Y. W. Sun, K. W. C. Kan, and Y. T. Zhang, "Terahertz image processing methods for biomedical applications," in *Proc. 30th Annual International Conference of the Ieee Engineering in Medicine and Biology Society*, Vols. 1-8, pp. 3751-3754, Vancouver, 2008.

Chapter 1

Introduction

Medical applications of terahertz imaging and spectroscopy have previously been demonstrated to be promising, yet they are still in their infancies. In this thesis using our reflection terahertz system, we aim to further study terahertz imaging in biological tissues with a view to exploring its potential as a new diagnosis tool. This thesis presents a number of novel analysis techniques and some pilot medical applications. All of them are important steps towards using terahertz radiation for clinical applications.

This chapter starts with some general introductions into terahertz radiation and its key features. Sections 1.2 and 1.3 provide a brief review on the current status of terahertz imaging and spectroscopy techniques, with emphasis on the applications in biomedical fields. In Section 1.4 the motivations and objectives, and in Section 1.5 the structure of this thesis will be mapped out.

1.1 Terahertz radiation

Terahertz radiation, also termed as THz waves, THz light, or T-rays, is situated in the far infrared range of the electromagnetic spectrum (EM), between mid-infrared and microwaves. The terahertz region is typically defined as ranging from 0.1 to 10 THz (1 THz = 10^{12} Hz) in frequency, or 3 mm to 30 μm in wavelength, as shown in Figure 1.1. Experiments with terahertz radiation can date back to measurements of black body radiation using a bolometer in the 1890s [1, 2]. However, for a long time, this region remained less unexplored due to a previous lack of good sources and detectors, and it was commonly referred to as the 'terahertz gap'. In 1975, David Auston at AT&T bell Laboratories developed a photoconductive emitter gated with an optical pulse that led towards bridging this gap - the 'Auston switch' emitted broadband terahertz radiation up to 1 mW [3]. Ever since then many improvements

in the generation and detection of coherent terahertz radiation enabled terahertz time domain spectroscopy and imaging techniques to be pioneered for applications in various fields such as biomedical engineering, physics, astronomy, security screening, communications, genetic engineering, pharmaceutical quality control and medical imaging. Particularly, applications in medical area are believed to be very promising but challenging.

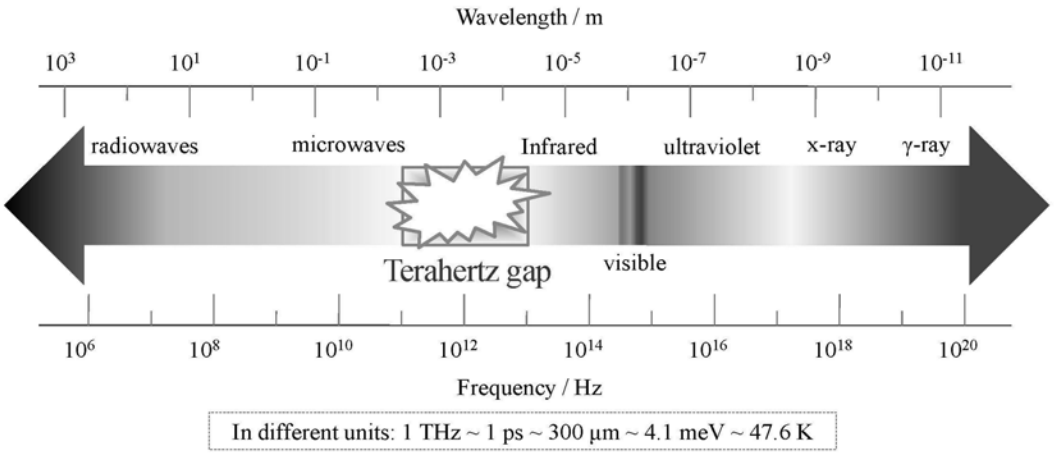

Figure 1.1: The terahertz region of the electromagnetic spectrum lies between the infrared and microwave region, where neither photonic nor optical mechanisms dominate.

1.1.1 Terahertz sources and systems

Over the past two decades, technologies for generating and detecting terahertz radiation have changed considerably. Upon these advances, various terahertz systems have been set up by many groups all over the world and several commercialized systems are available now [4-8]. According to the laser source used, THz systems can be divided into two general classes: continuous wave (CW) and pulsed.

A typical CW system can produce a single fixed frequency or several discrete frequency outputs. Some of them can be tunable. Generation for CW terahertz radiation can be achieved by approaches such as photomixing [9], free-electron lasers [10] and quantum cascade lasers [11]. Since the source spectrum of this kind of system is narrow and sometimes only the intensity information is of interest, the data structures and post-processing are relatively simple. It is possible now to drive a whole CW system by cheap laser diodes and thus it can be made compact and

inexpensive and therefore cost effective. But due to the limited information that CW systems can afford, they are sometimes confined to those applications where only features at some specific frequencies are of interest.

In pulsed systems, broadband spectrum up to several THz can be radiated. Currently, there are a number of ways to generate and detect pulsed THz radiation, such as ultrafast switching of photoconductive antennas [3], rectification of optical pulses in crystals [12], rapid screening of the surface field via photoexcitation of dense electron hole plasma in semiconductors [13] and carrier tunneling in coupled double quantum well structures [14]. Among them, the most established approaches are based on photoconductive antennas, where an expensive femtosecond laser is required. Coherent detection in these techniques can record THz waves in the time domain, including both the intensity and phase information, which can be further used to obtain more details of the target, like spectral and depth information [15]. This key advantage lends coherent THz imaging to a wider range of applications.

More information and detailed comparisons of these two types of systems can be found in reference [16]. Our experimental system is a commercialized imaging platform in a reflection geometry (a full description of this system will be given in Chapter 2). In the remaining chapters of this thesis, our discussion will be based on pulsed type unless otherwise specified.

1.1.2 Key features leading to medical applications

Several unique features make terahertz very suitable for medical applications. For example, it has very low photon energy (1 THz = 0.0041 eV, in comparison, that of visual light is about 2 eV), which is insufficient to cause chemical damage to molecules, or knock particles out of atoms. Thus it will not cause harmful ionization in biological tissues; this makes it very attractive for medical applications. Research into safety effects of THz exposure on biological objects such as keratinocytes [17], skin [18] and blood leukocytes [19] has been investigated, none of which have revealed any adverse effects from exposure. Terahertz radiation is very sensitive to polar substances, such as water and hydration state. For this reason, THz waves sometimes can provide a better contrast for soft tissues than x-rays. Another important feature is that THz time-domain spectroscopic techniques use coherent

detection to record the THz wave's temporal electric fields, which means both the amplitude and phase of the THz wave can be obtained simultaneously. The temporal waveforms can be further Fourier transformed to give the spectra. This allows precise measurements of the refractive index and absorption coefficient of samples without resorting to the Kramers-Kronig relations. Moreover, it has been found that the energy of rotational and vibrational transitions of molecules lies in the THz region and intermolecular vibrations such as hydrogen bonds exhibit different spectral characteristics in the THz range. These unique spectral features could be used to distinguish between different materials, recognize a certain material, and even determine the composition of unknown objects.

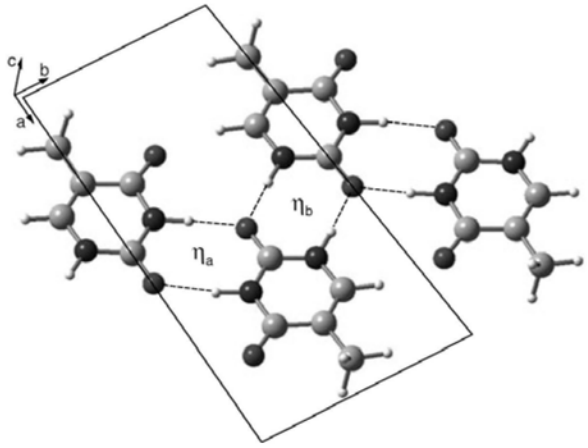

Figure 1.2: Different hydrogen bonds (η_a and η_b, with different motions) in thymine molecules can be probed by terahertz spectroscopy. (Cited from B.M. Fischer's paper [20])

1.2 Terahertz techniques in reflection configuration

1.2.1 Reflection vs. transmission

THz waves can penetrate plastic, paper and many other organic materials, provided that the water content in them is very low. Similar to x-rays, when they propagate in a sample (as shown in Figure 1.3 (b)), there would be some attenuation and therefore the transmitted THz waves could be utilized to analyze the dielectric parameters of the sample. Meanwhile, some of incident light will be reflected off the

sample interface before the THz waves enter the sample (as shown in Figure 1.3 (a)). The reflected pulse is determined by the Fresnel's equation and thus it also can be used to calculate the sample's complex refractive index. The detailed theory of how the complex refractive index is extracted in a reflection system will be presented in Chapter 2.

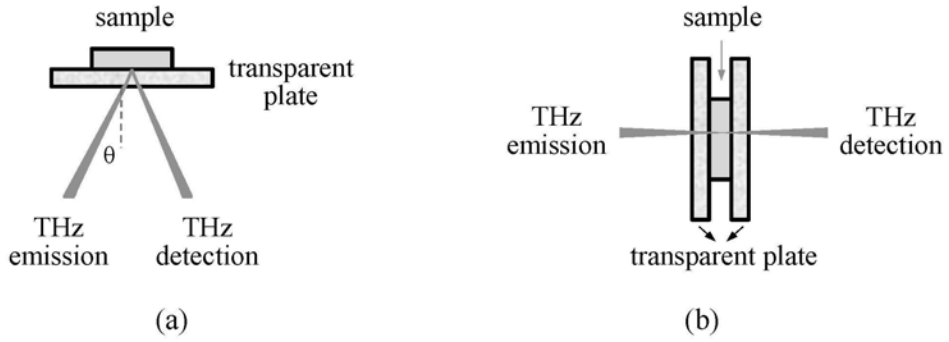

Figure 1.3: Schematic diagrams of terahertz systems in different configurations: (a) reflection (with angle of incidence, θ) and (b) transmission.

In the transmission mode, the emitted THz radiation is collimated to the sample and the transmitted part is detected on the opposite side. Since the THz waves have to travel through the whole sample, a common problem for a conventional transmission system is that it is very difficult to detect signals from samples that strongly absorb terahertz radiation such as fresh tissues [21]. In this case, very thin slices should be prepared. In order to extract the absorption coefficient, an accurate thickness of the object is of vital importance. However, when dealing with samples like excised biological tissues, as they are usually soft and thus easy to suffer from deformation under pressure, direct measurements of their thicknesses can be very difficult.

Terahertz systems in reflection geometry could be an alternative to overcome this limitation, especially for applications in biological tissues. Since the detection in this geometry is from the same side as the incident THz waves, it allows *in vivo* and *ex vivo* measurements without concern for the absorption or thickness measurement of soft samples. In addition, it can be further used to reveal the inner structure of low absorbing samples. This is possible because if the refractive index of the target layer is known, the temporal delay information between the different reflected pulses off the surface and bottom can be used to calculate the thickness of the layer.

1.2.2 Terahertz pulsed imaging and spectroscopy

Terahertz time domain spectroscopy is often shorted as THz-TDS and for convenience sometimes it is also referred to as terahertz spectroscopy or terahertz pulsed spectroscopy in this thesis.

Terahertz pulsed spectroscopy

Terahertz spectroscopy is typically done with a single point measurement (with transmission geometry in most cases) of a homogenous sample and the resulting terahertz electric field can be recorded as a function of time. Thus it can be Fourier transformed to offer meaningful spectroscopic information due to the broadband nature of pulsed THz radiation. Although the spectral resolution is not as good as that with narrowband techniques, coherent detection of THz-TDS can provide both high sensitivity and time-resolved phase information [22]. This spectroscopic technique is primarily used to probe material properties and it is helpful to see where it lies in the electromagnetic spectrum in relation to atomic and molecular transitions.

Terahertz pulsed imaging

Terahertz pulsed imaging actually can be viewed as an extension of the THz-TDS method. In addition to providing valuable spectral information, 2D images can be obtained with THz-TDS by spatial scanning of either the terahertz beam or the object itself. In this way, geometrical images of the sample can be produced to reveal its inner structures [23]. Thus, it is possible to provide three-dimensional views into a layered structure.

Other related techniques

The pioneering terahertz spectroscopy experiment was done by M. v. Exter *et al* in 1989 [24], in which the absorption spectrum of water vapor was studied and nine sharp lines were accurately mapped out in the region from 0.2 to 1.45 THz. Several months later, Grischkowsky *et al* studied the absorption and dispersion of a number of dielectrics and semiconductors [25]. In 1995, terahertz imaging was demonstrated

by Hu and Nuss [26]. Since then, there has been an increasing interest in these two fields and a number of research groups have successfully built their spectroscopy and imaging systems. Meanwhile, great advances have been achieved in various THz techniques including three-dimensional imaging [27], near-field imaging [28, 29], single-shot imaging [30] and time reversal imaging [31]. These progresses have opened up a new prospect for researches in both basic science and applications.

1.3 Current situation on terahertz applications in biomedicine

1.3.1 Previous studies

There has been an increasing interest in terahertz spectroscopy of biologically related applications within the last few years and more and more terahertz spectra are being published.

Biomolecules and pharmaceuticals

Terahertz spectroscopy explores low frequency motions in molecular systems. These motions are either flexing of the individual molecules themselves or intermolecular interactions, either via strong hydrogen bonds or weaker van der Waals bonding between nearest neighbors. These large amplitude vibrations can provide insight into the structural dynamics of biomolecules, such as proteins, or formation of polymorphs and hydrates of crystalline materials; this has opened up possibilities for employing terahertz spectroscopy in genetic engineering and pharmaceutical industry.

Fluorescent labeling [32] is one of the key and traditional methods for genetic analysis by identifying the genetic bases of DNA. However, its slow process and the fluorescent marker may modify the conformation of DNA sequence thus affecting the precision of detection. Therefore, introducing label-free gene sensing with terahertz could be an alternative approach to achieve a more rapid and precise genetic analysis methodology. Bolivar *et al* demonstrated that the label-free sensing technology can be achieved using either free-space or waveguide on-chip THz setups to detect the difference in complex refractive index among hybridized and denatured

DNA samples [33]. Shen *et al* demonstrated that terahertz time domain spectroscopy could be used to distinguish between purine and the DNA base adenine [34]. In their experiments they have observed absorption peaks in the terahertz region for the poly-crystalline nucleosides, and mapped the evolution of these absorption features continuously between 4 and 295 K [35]. Additionally, a recent study conducted by Fischer *et al* showed that ribonucleic acid (RNA) containing different DNA bases can be distinguished by terahertz techniques [36]. They used terahertz time-domain spectroscopy to measure the dielectric function of two artificial RNA single strands, composed of polyadenylic acid (poly-A) and polycytidylic acid (poly-C). They found a significant difference in the absorption between the two types of RNA strands.

Polymorphism is a common issue in the pharmaceutical industry and determining the polymorphic form of a drug is very important as it can significantly affect the bioavailability and physiochemical response [7]. Scientists have been employing terahertz spectroscopy to distinguish between polymorphic forms. Strachan *et al* investigated crystallinity of Carbamazepine and enalapril maleate and their results show that different polymorphic forms of carbamazepine and enalapril maleate exhibit distinct terahertz absorbance spectra [37]. More recently, Zeitler *et al* studied carbamazepine and sulfathiazole [38]. In their experiments, spectroscopy was used to monitor the dynamics during the conversion process of those two drug materials. They found that terahertz spectroscopy was able to reveal distinct spectra for each of the five know polymorphic forms and they related the phase transitions observed to the thermal data. From their investigations we see that terahertz spectroscopy is able to provide complimentary information to other techniques such as Raman spectroscopy, and also be used to detect impurities.

Tissue differentiation

Terahertz radiation can be severely absorbed by polar liquids and biological tissues with high water content. Due to a limited penetration depth in these objects, to date THz applications have been limited to easily accessible parts of the body, for instance, skin, breast tumors and teeth. On the other hand, as outlined earlier, THz attenuation is very sensitive to water content and this has led to great interests in the

investigation of tissue hydration. Recently, a number of applications in this area have been investigated.

Imaging skin with THz radiation has been well studied both *in vivo* and *ex vivo*. For instance measurements of the skin on the forearm and the hand have been used to determine hydration levels [39]. In addition, the thickness of the stratum corneum can be determined from the optical delay between the reflection off the top surface of the stratum corneum and the reflection off the stratum corneum-epidermis interface [40]. In vivo images of basal cell carcinoma have also shown contrast between diseased and healthy tissue [40, 41]. It was found that diseased skin tissue (basal cell carcinoma) had an increased absorption coefficient compared to normal tissue [41]. Breast cancer detection with THz imaging has also been demonstrated. A feasibility study using TPI to map out tumor margins on excised human breast tissue found good correlation between the area and shape of tumor deduced from the terahertz images and that from histology [42]. In addition, the authors determined the optical properties of the excised normal breast skin and breast tumor through transmission spectroscopy and used finite difference time domain methods to illustrate that the optical properties are responsible for the differences seen in the time domain [43]. The detection of dental caries is another potential application [43]. Crawley *et al* presented results for the detection of early stage caries in the occlusal enamel layer of a range of human tooth cross sections using TPI system [44]. Pickwell *et al* then investigated the correlation of the refractive index changes with mineral loss and found that terahertz imaging was also able to measure the depth of more substantial demineralization [43].

To date, *in vivo* measurements of organs other than skin have not been reported and so measurements of excised fresh tissue samples have been the alternative to push THz for pathological diagnostic purposes. Many pilot investigations of excised human and animal tissue have been tried by different research groups worldwide. For instance Mittleman *et al* tested chicken breast tissues and demonstrated that THz imaging may be useful for burn diagnosis [45]. Experiments to identify different tissues with 'fresh' untreated samples were done by Arnone *et al* [46] and Han *et al* [47]. Terahertz transmission images of histo-pathological samples have also revealed contrast between different tissue types [48]. The larynx of a pig was imaged in this

way and contrast between the soft tissue and cartilage was seen at particular frequency windows. Similarly in an image of a histo-pathological human liver sample with metastasis, contrast was observed between the healthy and diseased areas. To make the samples suitable for measurements, the samples have been formalin-fixed, alcohol-dehydrated and paraffin-mounted. Another common method for treating the fresh tissues is lyophilization and investigations of samples with this treatment process includes recent work reported by Png *et al* [49] and Hoshina *et al* [50].

Spectral Database of different tissues

Terahertz imaging and spectroscopy for biological tissues is still a burgeoning research area and there is a lack of standards for sample handling and data processing. Compiling a database to detail the response of different biological tissues in the THz band, for example temporal features and frequency dependant complex refractive index would greatly benefit THz imaging and spectroscopy. Table 1.1 is a survey of previous studies in the area of tissue differentiation with different system configurations, tissue types and presented parameters.

1.3.2 Main challenges

From Table 1.1 it can be seen that the majority of the aforementioned terahertz spectroscopy data were obtained in transmission mode. Terahertz radiation cannot penetrate very far into samples with high water content due to strong water absorptions at terahertz frequencies. This means that very thin slices of biological samples (around 500 um or thinner) are needed for transmission spectroscopy measurements. This is often difficult to achieve in fresh tissue samples. Freezing the sample makes it rigid and easier to slice thinly and uniformly. Recently, fresh and lyophilised tissue samples from a selection of rat organs were measured using terahertz transmission spectroscopy to investigate the impact of hydration changes on the optical properties [49]. It was found that lyophilizing the rat tissue samples reduced the absorption coefficient. This was also consistent with findings by Ashworth *et al* from fresh and frozen excised human breast tissue measurements [51].

Table 1.1: Summary of previous studies on THz applications related with tissue characterization.

Paper	System Geometry	Sample description	Data presented
Arnone *et al* 1999 [46]	Transmission	Muscle, fat and kidney	Temporal waveform and image
Han *et al* 2000 [47]	Transmission	A 0.5-mm pork muscle tissue	Attenuation coefficient
Loffler *et al* 2001 [52]	Transmission	formalin-fixed, alcohol-dehydrated and paraffin-mounted samples from thin-cut canary's head	Time domain intensity, spectral intensity and phase
Knobloch *et al* 2002 [48]	Transmission	The larynx of a pig and a human liver with metastasis	THz image by Spectral power density
Ferguson *et al* 2002 [53]	Transmission	A butterfly sample and a dried chicken tissues with bone	Temporal waveform and image
Woodward *et al* 2003 [54]	Reflection	Basal cell carcinoma samples	Time domain amplitude and reflected power
Berry *et al* 2003 [55]	Transmission and reflection	Nine types of tissues and water	Broadband linear attenuation coefficient (in transmission mode)
Fitzgerald *et al* 2003 [56]	Transmission	Skin, adipose tissue, striated muscle, vein and nerve	RI (broadband) and linear attenuation coefficient (frequency dependent)
Wallace *et al* 2006 [41]	Transmission	Excised normal skin and Basal cell carcinoma	RI and AC
He *et al* 2006 [57]	Transmission	Meat and skin samples from pork and rat	AC
Nakajima *et al* 2007 [58]	Transmission	Paraffin-Embedded Liver tissues	images from RI and EC
Pickwell *et al* 2007 [43]	Reflection	Bovine slabs with artificial caries	Temporal waveform and RI
Png *et al* 2008 [49]	Transmission	Fresh and frozen rat tissues	RI and AC
Hoshina et al 2009 [50]	Transmission	Slices of frozen porcine tissue	RI, AC and THz images

RI – refractive index; AC – absorption coefficient; EC – Extinction coefficient

Therefore to avoid such sample manipulations, it is more feasible to perform measurements in reflection geometry. In this configuration, the THz light reflected by the sample is used to determine the sample properties. Since the reflected light is collected, samples do not need to be very thin. In fact to prevent etaloning and multiple reflections, the sample should be relatively thick (at least 1mm) and be homogenous.

1.4 Motivations and objectives

Terahertz imaging as a novel tool for medical applications is a recently immerging field and it has not been explored much compared with other conventional modalities. Much of the current research has been focused on improving the system hardware. Until now, only a few applications were investigated in the reflection geometry and there is an increasing need for systematic research on the protocols and algorithms.

Therefore, the goal of this thesis is to facilitate terahertz pulsed imaging for future clinical use and the main work will focus on the following aspects:

- ✧ To develop new algorithms that can effectively improve the system accuracy.
- ✧ To develop new techniques that can be used to reveal the sample's structure of properties.
- ✧ To design and verify protocols for studying biological tissues with full-scale investigations.
- ✧ To explore new applications.

1.5 Structure of this thesis

The rest of the thesis is organized as follows: Chapter 2 gives a detailed description of the experimental system, protocols and methodology. The theory of how the optical parameters are extracted in reflection geometry will be discussed and a novel solution is given to incorporate the angle of incidence.

Chapter 3 evaluates the system performance and proposes two original algorithms to improve the accuracy. Our system's variation is reduced effectively and a general

baseline approach for reflection systems is designed. Original simulation work is also performed to show the SNR impacts on refractive index and the absorption coefficient.

Chapter 4 discusses the terahertz time-of-flight technique. The relationship between layer thickness, optical delay and the refractive index of the sample in our system is established and it is originally used to assess the skin burn severity.

In Chapter 5, novel THz applications of healthy and diseased organ tissues are presented. Experiment methods and protocols will also be discussed.

Finally, conclusions and future work are discussed in chapter 6.

Chapter 2

Experimental system and established THz characterization methods

The aim of this thesis is to carry out a systematic study of terahertz pulsed imaging on potential medical applications. Different parameters in both time and frequency domains of the sample will be investigate. In the frequency domain, one important step is to characterize the complex reflective index. In this chapter, I first describe the system we used for this thesis. Then some important concepts and techniques will be covered and after that the detailed theory of extracting the complex refractive index in the reflection geometry will be presented.

2.1 Experimental setup

2.1.1 Optics structure

Our experimental system is a commercial imager, TPI Imaga 1000 (TeraView Ltd, UK). The hardware schematic diagram is illustrated in Figure 2.1. Both the generation and detection for the terahertz radiation are achieved by low-temperature-grown GaAs photoconductive devices and an ultrafast laser (Vitesse, Coherent Inc.), emitting 90 fs pulses centered at a wavelength of 800 nm, with a 80 MHz repetition rate and an average power of about 200 mW. The laser beam is separated into the pump and probe beams by a beam splitter. The pump beam is focused onto the photoconductive switch. As illustrated in Figure 2.2, when the central gap of the biased switch is illuminated by femtosecond laser pulses,

photo-excited carries are accelerated and create an ultra-short current. The relaxation of these carriers produces a broad band terahertz field. The emitted terahertz waves are then focused onto the sample by a silicon lens and a pair of off-axis parabolic (OAP) mirrors. In the detection branch, the terahertz pulses reflected off the sample are re-collimated using another pair of off-axis parabolic mirrors and focused onto the photoconductive receiver, which has the same structure as the emitter antenna. Detection may be viewed as the reverse process of the photoconductive emission.

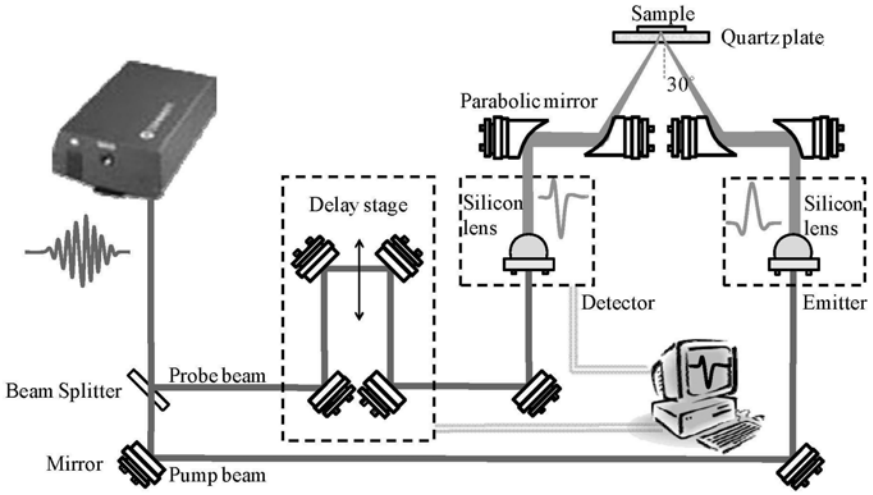

Figure 2.1: Hardware schematic diagram of the TPI^{TM} system.

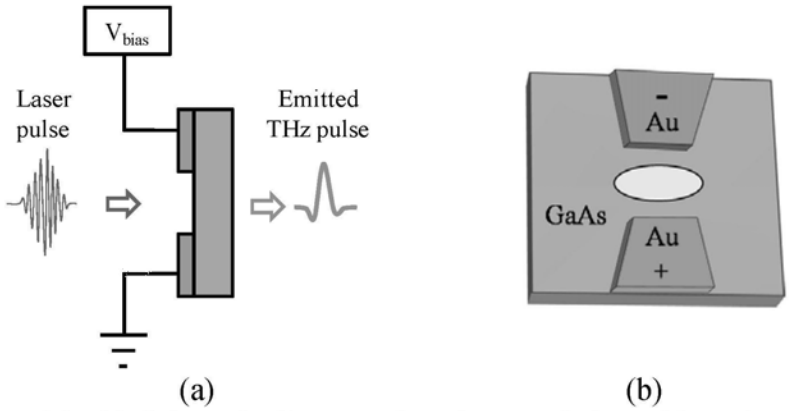

Figure 2.2: (a) Schematic diagram of terahertz emission with a photoconductive switch. (b) Front view of the bow-tie switch. On the GaAs substrate the two gold electrodes define a lateral photoconductive gap of the order of 10 μm.

Rather than applying a biased voltage to the electrodes, the laser pulse is employed to gate the switch, and a current amplifier and ammeter are connected to measure the transient current generated by the laser pulse and the THz electric field. The

measured current is directly proportional to the time-varying electric field of the THz radiation. In this way, both the amplitude and phase of the incident THz wave can be obtained. By sweeping the optical delay through the entire terahertz pulse (at for instance a rate of 15 Hz) the time-domain terahertz waveforms can be obtained.

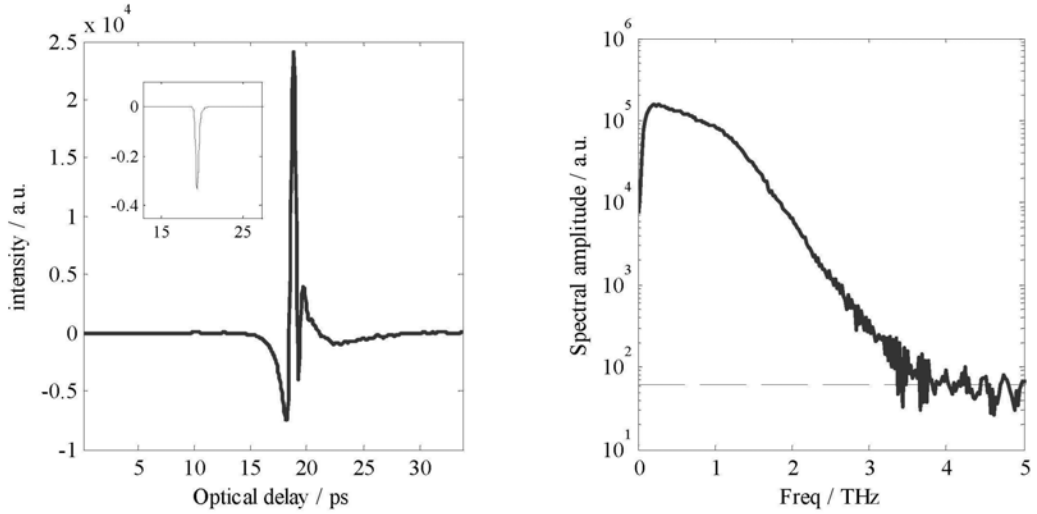

Figure 2.3: (a) Temporal waveform of a mirror sample (drawn by raw data with the inset representing its corresponding processed data). (b) The corresponding spectrum with the noise floor (indicated by dashed line).

2.1.2 Point measurement and raster scanning

Data acquisition in the system can be conducted either by a point measurement or by a full scan of the sample. A point measurement is analogous to an ultrasound A scan and yields a dataset containing 512 data points over around 40 ps (adjustable through a galvometer. In this study it was selected as either 34 ps or 47 ps.) in the time domain, as plotted in Figure 2.3a. This time domain waveform can be Fourier transformed into the frequency domain to obtain spectral information (Figure 2.3b), from which we can see that it hit the noise floor around 3 THz.

By raster scanning in the x-y plane over a defined area, a grid of pixels can be collected. The maximum area that can be allowed is 15 mm by 15 mm. With a raster scan, it gives a three-dimensional dataset, from which 2D or 3D images can be constructed.

2.1.3 Imaging window

The system has a window onto which the sample under investigation can be placed, as depicted in Figure 2.4. To achieve this, a 2 mm thick Z-cut quartz plate is used for its hardness and more importantly, it is transparent to terahertz radiation. Additionally, as the phase information depends on the position of the measured object and it is crucial to place the sample and reference exactly in the same position [59], possibilities of phase error due to a misplacement of the sample and reference can be reduced by fixing the quartz window in the system. The refractive index of the quartz in our system is 2.12, with a negligible absorption coefficient from 0.1 – 3 THz.

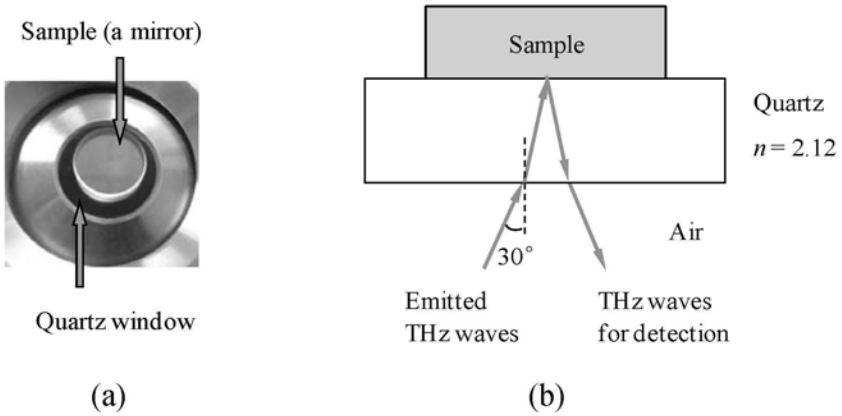

Figure 2.4: The sample holder in the TPI system. (a) Photograph of the image window with a mirror sample on top. (b) Diagram of the reflection configuration with an angle of incidence of 30° in the air. Refractive index of the quartz layer is 2.12.

The photograph and the schematic diagram in Figure 2.4 show the typical reflection configuration with a sample (here it is a mirror) sitting on the quartz plate. The THz lights out of the emitter are collimated to the quartz plate with a fixed angle of incidence, 30 degrees in our case (Figure 2.4b). In practical measurements, the mirror is replaced by other samples of interest. For non-liquid materials like mirror, air and biological tissue samples, in most cases they can be simply placed on top of the quartz window for data collection. For liquid samples like water, a rubber ring is used to contain the liquid.

2.2 Basic THz techniques

2.2.1 Reference and Baseline signals

The incident THz light of the system is unknown, so to determine this, a reference sample with known optical properties is measured. In our study, this is typically done by measuring the air; in other words, from a measurement with nothing on the imaging window.

To introduce the baseline concept, let's look back at the lower surface of the quartz window in Figure 2.4b. There will be a pulse reflected off it when a THz wave is incident on it. This pulse is referred to as the baseline. Ideally it can be obtained by placing an additional quartz plate (the same material as the image window); since the radiation is now effectively passing through a very thick layer of quartz, there are no reflections except for those off the lower surface of the fixed quartz window. Therefore a baseline waveform can be subtracted from both the reference and sample waveforms to remove any back-surface reflection off the quartz/air and quartz/sample interface measurements.

2.2.2 Raw data, processed data and system response function

The data originally recorded by the detector from a point measurement or raster scan is often called raw data. A typical waveform of the raw data acquired from a mirror in our system has already been shown in Figure 2.3a. The terahertz source is very dependent on the photoconductive switch and its alignment. As a result, the raw data shapes from different systems can have significant variations due to differences in generation and detection as well as the imaging geometry. To get comparable results from different terahertz systems, the terahertz community usually uses response functions to describe how targeted samples respond to broadband terahertz radiation. When a targeted sample is placed on the quartz imaging plate, the acquired data would represent the impulse function of the subject convolved with the incident signal, which can be indirectly determined by a reference signal. Thus the impulse function of the sample can be obtained by deconvolving the reference signal as in

(2.1).

$$\text{FFT(impulse function)} = \frac{\text{FFT(sample - baseline)}}{\text{FFT(reference - baseline)}} \times \text{FFT(filter)} \tag{2.1}$$

Dividing the sample by the reference removes the system response but also increases the noise. Several methods could be used to remove the noise, for example using a low pass filter [23]. In this thesis a Gaussian filter function is applied to remove both the low and high frequency noise components. This data processing method has also been described in reference [60]. With (2.1), an inverse Fourier transformation can be used to yield the pulse function in the time domain. Corresponding to the previous raw data, this time response function is called processed data (see the inset in Figure 2.3a).

2.2.3 Signal parameters

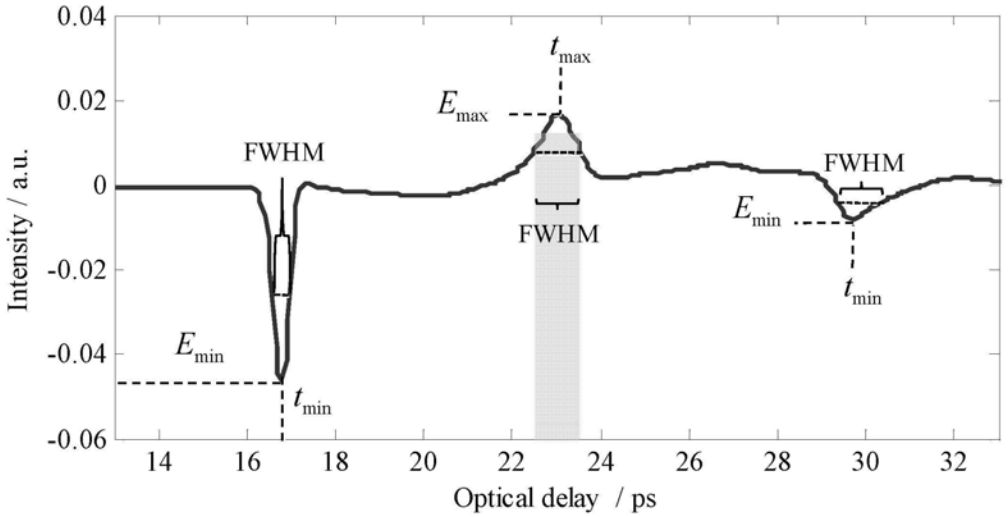

Figure 2.5: Time domain parameters.

The inherent characteristic of coherent detection enables processing THz data in both the time and frequency domains. Various parameters in these two domains can be utilized when investigating an unknown target and thus different choices can be made to meet the study aims. Commonly used parameters in time domain include pulse amplitude, pulse width and pulse delay, all of which can be easily obtained from the acquired temporal waveform. They can immediately provide some rough

profiles of the target; for instance, pulse width represents the average proportion of reflected power, pulse width may reflect some absorbance at different frequency components, and pulse delay is usually related to distance information [61]. An example showing how these parameters are determined in a captured waveform is given in Figure 2.5, in which the amplitude and time delay of an individual pulse are quite straightforward as denoted by E_{max} and t_{max} for a peak or by E_{min} and t_{min} for a trough, whereas pulse width is represented by the full width at half maximum (FWHM). Since this width is actually a time difference, it thus can also be referred to as full duration at half maximum (FDHM).

All the above steps are mostly done in the time domain after completion of data acquisition. Indeed parameters in the frequency domain such as spectra intensity and phase angle at different frequency components can be obtained by simply applying a Fourier transform.

A family of THz images can be constructed from these various parameters in the two domains, for example, by plotting the waveform maximal or minimal values at each pixel (E_{max}, E_{min}, as illustrated in the Figure 2.5) and using a false color scheme to represent the pulse intensity. These parameters can be potentially used to reveal clinically relevant features among tissues [53, 62, 63].

There is also great potential for using frequency dependent optical parameters for identification. In comparison with the easy steps for the above mentioned parameters, calculating the frequency dependent optical parameters is more difficult.

2.3 Evaluation of complex refractive index in reflection geometry

The changes of a light ray caused by its passage through a medium are determined by the complex refractive index of the medium, which is a function of frequency (ω) such that $\tilde{n}(\omega) = n(\omega) - i\kappa(\omega)$, where $n(\omega)$ is the refractive index and $\alpha(\omega)$ is the absorption coefficient which can be calculated as follows,

$$\alpha(\omega) = \frac{2\omega \cdot \kappa(\omega)}{c} \tag{2.2}$$

Here, c is the speed of light in a vacuum.

As we have mentioned many times, TPI can obtain both the amplitude and phase information of the detected THz waves. Therefore, the complex refractive index of a sample can be acquired through the Fresnel's coefficient in a reflection mode. When terahertz waves are collimated to the sample, different angles of incidence may be used. A normal incidence configuration allows extraction of the complex refractive index with an analytical expression. However, in this case it usually requires a beam splitter such that the generation and detection of the THz waves can be spatially separated. The inclusion of the beam splitter will usually cause some undesired loss of the THz power and the resulting signals may suffer from a deteriorated signal to noise ratio [64]. To avoid this problem a possible way is to set a non-normal angle of incidence. The price would be the more cumbersome steps in extracting the dielectric parameters. In the remainder of this section, I will give a detailed explanation on how the complex refractive index is calculated in both the normal and non-normal cases.

2.3.1 Normal incidence

As illustrated in Figure 2.6, consider an interface formed by two mediums, represented by medium i and t respectively, and denote their corresponding complex refractive index as $\tilde{n}_i$ and $\tilde{n}_t$. In the normal incident case, the incident pulse E_i is guided perpendicular to the interface, that is, the angle of incidence θ_i equals to zero.

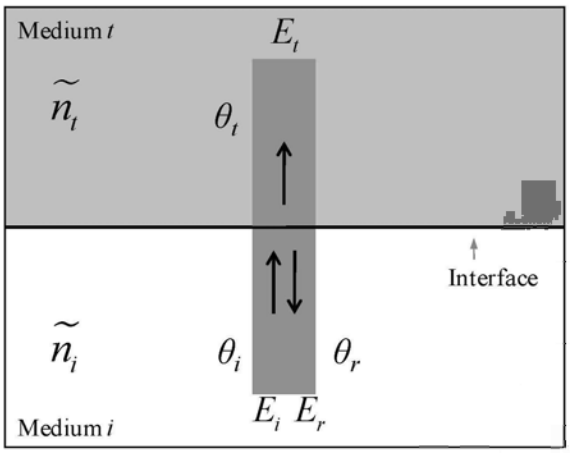

Figure 2.6: Schematic diagram of reflection geometries with normal incidence.

From Snell's law it is easy to get the zero values for the angles of reflection θ_r and

refraction θ_t. The reflected electric field off the interface and transmitted one are denoted by E_r and E_t, and their values are determined by the Fresnel's equations as well as their polarization statuses. Since the incident terahertz light is s-polarized in our system, the reflection coefficient r can be simply defined as in (2.3),

$$r = \frac{E_r}{E_i} = \frac{\tilde{n}_i - \tilde{n}_t}{\tilde{n}_i + \tilde{n}_t} \tag{2.3}$$

With this equation, the complex refractive indices $\tilde{n}_i$ and $\tilde{n}_t$ are related with the measured electric fields. In our case, medium i is usually the quartz window with a known complex refractive index $\tilde{n}_{quartz}$ and medium t is the sample with complex refractive index $\tilde{n}_{sample}$. For the sample, (2.3) can be written as,

$$r = \frac{E_{sample}}{E_i} = \frac{\tilde{n}_{quartz} - \tilde{n}_{sample}}{\tilde{n}_{quartz} + \tilde{n}_{sample}} \tag{2.4}$$

Since E_{sample} can be recorded by the system but E_i is usually unavailable, to obtain $\tilde{n}$ of an unknown sample, an additional measurement of a reference is required. In this work, air is selected as the reference.

$$r = \frac{E_{air}}{E_i} = \frac{\tilde{n}_{quartz} - \tilde{n}_{air}}{\tilde{n}_{quartz} + \tilde{n}_{air}} \tag{2.5}$$

In order to remove the dependence on E_i, from (2.4) and (2.5) we define R as the ratio of the reflection coefficient for the sample over that of the reference such that:

$$R = \frac{E_{sample}}{E_{ref}} = \frac{\tilde{n}_{quartz} - \tilde{n}_{sample}}{\tilde{n}_{quartz} + \tilde{n}_{sample}} \cdot \frac{\tilde{n}_{quartz} + \tilde{n}_{air}}{\tilde{n}_{quartz} - \tilde{n}_{air}} \tag{2.6}$$

Rearranging (2.7), we can finally get $\tilde{n}_{sample}$ as,

$$\tilde{n}_{sample} = \frac{(1-R)\tilde{n}_{quartz}^2 + (1+R)\tilde{n}_{quartz}\tilde{n}_{air}}{[(1-R)\tilde{n}_{air} + (1+R)\tilde{n}_{quartz}]} \tag{2.8}$$

On the right hand side of (2.8), $\tilde{n}_{quartz}$ and $\tilde{n}_{air}$ are known, and R can be calculated by the electric fields measured from the sample and air. In this way, the complex

refractive index of the sample $\tilde{n}_{\text{sample}}$ can be calculated, which can then be further used to yield the refractive index and absorption coefficient.

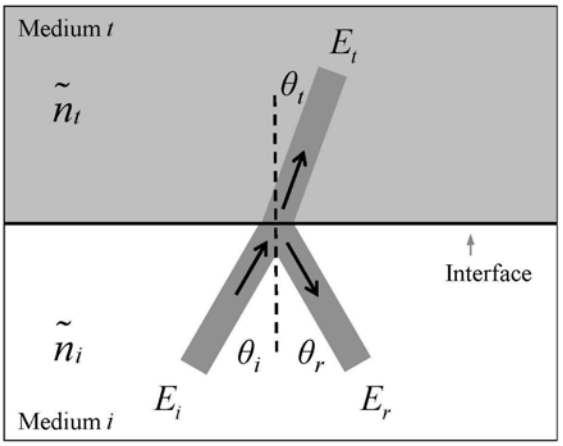

Figure 2.7: Schematic diagram of reflection geometries with non-normal incidence.

2.3.2 Non-normal incidence

The zero value of the angle of incidence in the normal incidence geometry enables analytical extraction of the complex refractive index, whereas in the non-normal case things get tricky due to the involvement of the angles, namely angle of incidence θ_{i}, angle of reflection θ_{r} and angle of refraction θ_{t}, as shown in Figure 2.7. When the trigonometric terms are added, the reflection coefficient r for an s-polarized wave becomes as:

$$r = \frac{E_{\text{r}}}{E_{\text{i}}} = \frac{\tilde{n}_{\text{i}} \cos\theta_{\text{i}} - \tilde{n}_{\text{t}} \cos\theta_{\text{t}}}{\tilde{n}_{\text{i}} \cos\theta_{\text{i}} + \tilde{n}_{\text{t}} \cos\theta_{\text{t}}} \tag{2.9}$$

If we denote the angles in the sample, quartz and air as θ_{sample}, θ_{quartz} and θ_{air}, (2.4), (2.5) and (2.6) can be rewritten as

$$r = \frac{E_{\text{air}}}{E_{\text{i}}} = \frac{\tilde{n}_{\text{quartz}} \cos\theta_{\text{quartz}} - \tilde{n}_{\text{air}} \cos\theta_{\text{air}}}{\tilde{n}_{\text{quartz}} \cos\theta_{\text{quartz}} + \tilde{n}_{\text{air}} \cos\theta_{\text{air}}} \tag{2.10}$$

$$r = \frac{E_{\text{sample}}}{E_{\text{i}}} = \frac{\tilde{n}_{\text{quartz}} \cos\theta_{\text{quartz}} - \tilde{n}_{\text{sample}} \cos\theta_{\text{sample}}}{\tilde{n}_{\text{quartz}} \cos\theta_{\text{quartz}} + \tilde{n}_{\text{sample}} \cos\theta_{\text{sample}}} \tag{2.11}$$

$$R = \frac{E_{\text{sample}}}{E_{\text{ref}}} = \frac{\tilde{n}_{\text{quartz}}\cos\theta_{\text{quartz}} - \tilde{n}_{\text{sample}}\cos\theta_{\text{sample}}}{\tilde{n}_{\text{quartz}}\cos\theta_{\text{quartz}} + \tilde{n}_{\text{sample}}\cos\theta_{\text{sample}}} \cdot \frac{\tilde{n}_{\text{quartz}}\cos\theta_{\text{quartz}} + \tilde{n}_{air}\cos\theta_{\text{air}}}{\tilde{n}_{\text{quartz}}\cos\theta_{\text{quartz}} - \tilde{n}_{air}\cos\theta_{\text{air}}} \tag{2.12}$$

Again, (2.12) can be rearranged. However, this time rather than $\tilde{n}_{\text{sample}}$ only the product $\tilde{n}_{\text{sample}}\cos\theta_{\text{sample}}$ can be extracted.

$$\tilde{n}_{\text{sample}}\cos\theta_{\text{sample}} = \frac{(1-R)\tilde{n}_{\text{quartz}}^2\cos^2\theta_{\text{quartz}} + (1+R)\tilde{n}_{\text{quartz}}\cos\theta_{\text{quartz}}\tilde{n}_{\text{air}}\cos\theta_{\text{air}}}{[(1-R)\tilde{n}_{\text{air}}\cos\theta_{\text{air}} + (1+R)\tilde{n}_{\text{quartz}}\cos\theta_{\text{quartz}}]} \tag{2.13}$$

Since all the values in the right side of (2.13) are either known or can be obtained from recorded signals, now the question becomes how to solve $\cos\theta_{\text{sample}}$. From Snell's law, we know that this angle is actually dependent on the refractive index of the medium where the light propagates. In our system, we can get their relation as,

$$n_{\text{sample}}\sin\theta_{\text{sample}} = n_{\text{quartz}}\sin\theta_{\text{quartz}} = n_{\text{air}}\sin 30° = \frac{1}{2} \tag{2.14}$$

In (2.13) let

$$\tilde{n}_{\text{sample}}\cos\theta_{\text{sample}} = Z \tag{2.15}$$

and take real parts of both sides we can obtain

$$n_{\text{sample}}\cos\theta_{\text{sample}} = \text{Re}(Z) \tag{2.16}$$

Using (2.14) and (2.16), $\cos\theta_{\text{sample}}$ can be expressed as,

$$\cos\theta_{\text{sample}} = \frac{\text{Re}(Z)}{\sqrt{\frac{1}{4} + (\text{Re}(Z))^2}} \tag{2.17}$$

Then substitute (2.17) into (2.13) and we can obtain $\tilde{n}_{\text{sample}}$. Meanwhile, the refractive index and absorption coefficient can also be determined as

$$n_{\text{sample}} = \frac{\text{Re}(Z)}{\cos\theta_{\text{sample}}} \tag{2.18}$$

and

$$\alpha_{\text{sample}} = -\frac{2\omega}{c}\frac{\text{Im}(Z)}{\cos\theta_{\text{sample}}} \tag{2.19}$$

2.3.3 Results

Now all the essential steps for extracting the complex refractive index in reflection geometry have been made clear. Actually, in order to simplify calculations, some of the systems in reflection geometry have been designed with a zero angle of incidence and for those with non-normal incidence, the angle of incidence was sometimes neglected, i.e., simply using the steps as in the normal case. Rønne took this effect into consideration and used an iterative method in their study [65]. In a different way, we managed to get analytical solutions for both n and α, as described in section 2.3.2.

Refractive index and absorption coefficient

To verified our method, we designed two tests on water and air. The frequency dependent n and α calculated using the method proposed in Section 2.3.2 are shown Figure 2.8, indicated by the pink squared line. A comparison with the calculations measured by a transmission system is also provided, represented by blue lines. It can be seen that, both results of n and α from the two different geometries are very close to each other over the whole evaluated frequency band (0.1 – 2 THz). To be noted, a study by Wallace has found that the most interesting frequency range for tissue measurements is from 0.5 to 1 THz [41]. It is clear, our results in this range match well with those from the transmission system, with a small difference. Considering the noise variation induced by the laser fluctuation and dependence on environmental conditions, we think that these calculations in our system are acceptable.

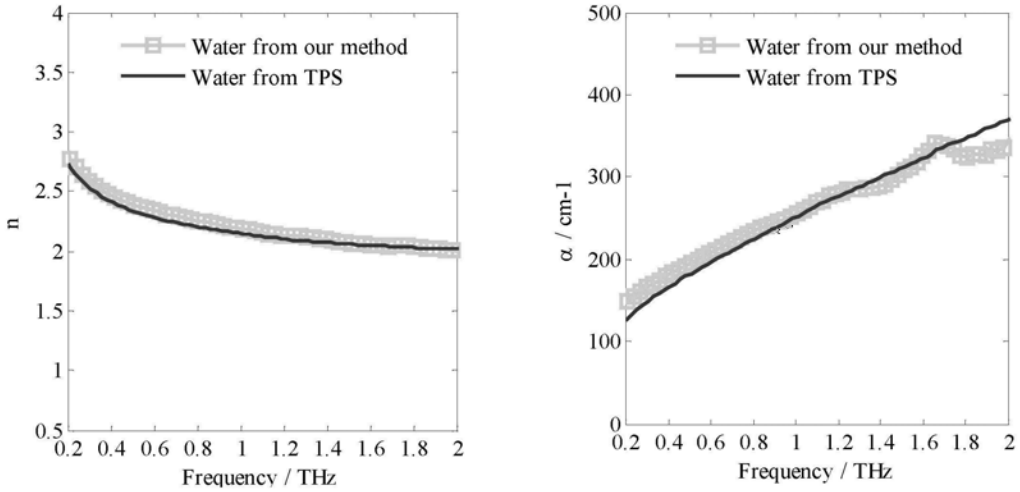

Figure 2.8: Comparison of complex refractive index of water extracted from our method and results from spectroscopy system in transmission geometry (TPS), (a) refractive index and (b) absorption coefficient.

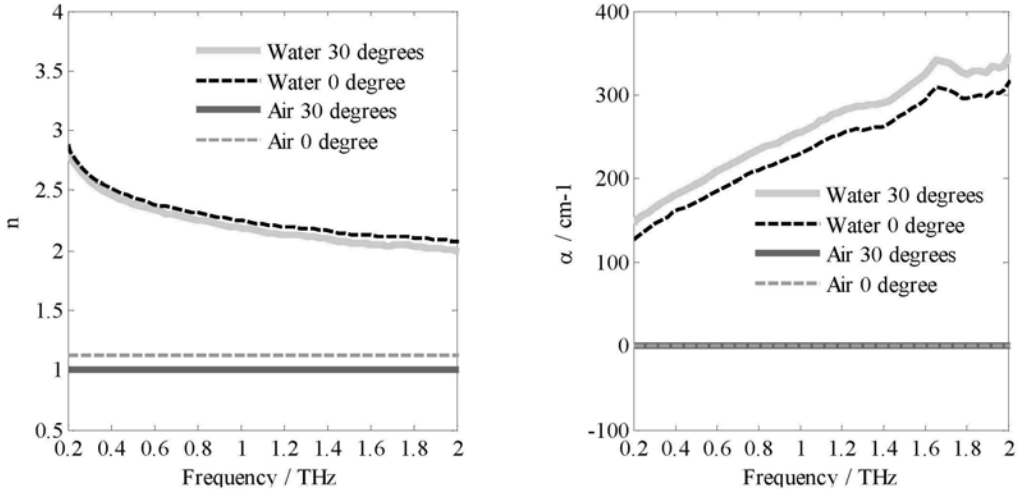

Figure 2.9: Results of (a) refractive index and (b) absorption coefficient with and without accounting the angle of incidence. Plots titled with 0 degree in the legend represent results by neglecting the angle of incidence (i.e., using Equation (2.28)).

To further evaluate the effects of the angle of incidence, we used the same data and repeated the steps to calculate n and α using the equations for normal incidence geometry. The results are shown in Figure 2.9. Calculations without accounting the angle of incidence are indicated by the dashed lines. For both water and air, they are clearly different from those after taking the angle into consideration, except for the absorption coefficient of air. By comparing the two groups (water and air) of the refractive index, we can see a larger discrepancy for the air group. It indicates that

the angle of incidence has a greater influence on the calculations for materials with smaller refractive index. This can also be found in the two refractive index plots of water, which get farther from each other as the refractive index decreases along the frequency axis.

Discussion

Equations in this part do not account for effects due to multiple reflections within the quartz imaging plate because they occur at optical delay times significantly (of the order 25 ps, see the geometry in Figure 1.3 and temporal waveform in Figure 1.4) beyond the sample main reflection. The earlier reflection off the air quartz surface was removed by subtracting the baseline signal from the sample and reference signals. The baseline measurement with an additional quartz plate requires the two quartz windows to be ideally contacted such that no reflections would be generated by their interface. In practice it is very difficult to get a satisfactory baseline and this process sometimes can be rather tedious as the windows need to be cleaned perfectly. It should also be noted that the theory we used was based on the assumption that scattering effects were negligibly small.

For data analysis, the electric fields (E) in all the above equations are manipulated in the frequency domain through Fourier transforms. Therefore, the obtained values of n and α are a distribution over the evaluated terahertz band (For the examples we gave above, the evaluated band is from 0.2 to 2 THz).

In the tests to evaluate our method, we selected water and air as our samples. Both of them are good materials for terahertz measurements as they are easily accessible and can make perfect contact with the quartz window. Indeed, the optical parameters of water can be affected for instance by its temperature [66] and our measurements were done under room temperature which may not necessarily be precisely the same as the one with which we compared. In addition, the water we measured was not purified. These two factors may have led to the minor difference in the optical parameters between our calculation results and those from TPS.

2.4 Summary

In this chapter we first made a general introduction on the hardware structure of our

experimental system, including some information on the photoconductive emission and detection principles. Then we introduced a number of basic concepts and data processing methods that will be frequently used in the following chapters. Based on the reflection geometry in our system, analytical solutions were given to extract the complex refractive index and the angle of incidence has been incorporated in the solutions. Furthermore, water and air were tested and the resulting complex refractive index had a good agreement with those measured by a transmission system. It shows that our system can extract the optical parameters with satisfactory accuracy and this enables us to use the system for practical applications.

Chapter 3

System evaluation and noise reduction

3.1 Introduction

Noise is always a concern as it can affect the accuracy of calculation in signal processing. Main sources of noise in a pulsed terahertz system include fluctuations in the ultrafast femtosecond laser, Johnson noise and shot noise [67-70], and all of them can be seen as stationary Gaussian processes. Due to the relative poor power efficiency of photoconductive antennas, the output power in a typical pulsed system employing photoconductor is low. Although highly sensitive detectors can be used to suppress the background noise, sometimes the data analysis is still very difficult due to a bad signal to noise ratio (SNR), especially when probing objects that strongly absorb THz radiation, for instance biological tissues. To accurately characterize a sample, good quality signals with high SNR are desired. Noise can be reduced by improving the hardware or using classical de-noising methods [71, 72]. In this chapter, we will evaluate our system and propose two algorithms to improve the system's performance. The first one is to reduce the signal variation during the raster scanning process and the second one is a new baseline approach to remove the baseline artefacts.

3.2 Evaluation of the system

3.2.1 SNR and DR

SNR is a common criterion to evaluate the system performance and there are a

number of ways to assess it. It is typically defined as the ratio between the mean magnitude of the signal and that of the noise. Actually, both the signal and noise can be defined in several ways, for example in the time domain or in the frequency domain [73]. Different definitions of the signal and noise sometimes make SNR confusing. In order to estimate the SNR, multiple datasets are required: signal and noise are calculated from mean and the standard deviation of these datasets respectively. In addition, since the signal is broadband in a pulsed system, the SNR values at different frequencies may vary a lot (see Figure 3.1). Another comparable indicator is the system dynamic range (DR). DR at a particular frequency in a pulsed system can be defined as the spectral amplitude in this frequency over the root mean square (RMS) of the noise floor. Similar to SNR, DR in a pulsed system is also dependent on frequency. Sometimes the maximum DR is simply quoted as the system DR.

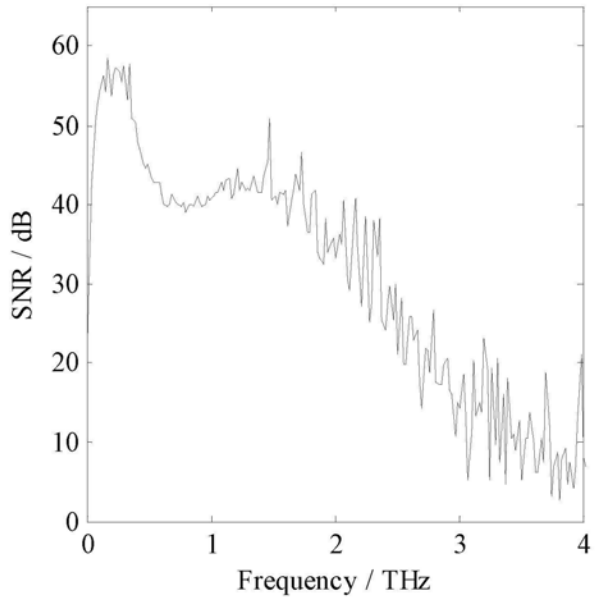

Figure 3.1: SNR distribution (in dB) over frequency from multiple trials. The signal was calculated by the mean value of the FFT spectra and noise was calculated by the standard deviation of the spectra. In this case, the sample was a gold mirror.

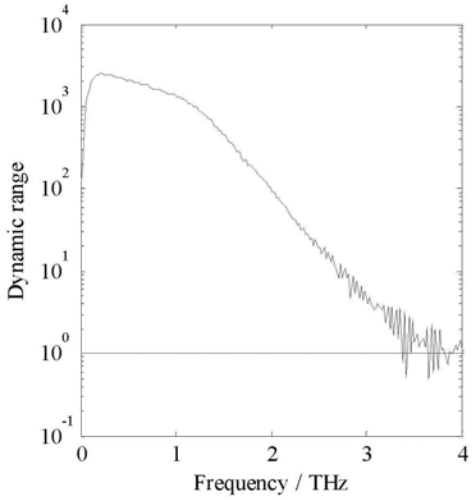

Figure 3.2: Dynamic range distribution over frequency. The spectral data was from a single point measurement and noise floor was estimated by the RMS of spectra greater than 3.5 THz. The spectra in this figure have been normalized to the noise floor (estimated as 61.9, indicated by the horizontal line) with a maximal DR of 2512 around 0.21 THz. In this case, the sample was a gold mirror.

We estimated SNR and DR in the frequency domain and show their results in Figure 3.1 and Figure 3.2, respectively. When evaluating SNR, multiple datasets were obtained by repeatedly measuring the central point of the image window. For DR, only a single dataset was used. It can be seen that both SNR and DR decline gradually in the high frequency band. Compared with DR which changes gently above the noise floor, SNR has shown greater fluctuations. Although there is no direct relationship between the values of SNR and DR [73], the maximum values of SNR and DR appear in the same area, in our case around 0.2 THz. It is worth noting that at frequencies below 2 THz, the SNR can be as high as around 40 dB and is good for signal processing, whereas at higher frequencies, the SNR is deteriorating and becomes unsatisfying. This is also the reason we have limited our frequency analysis to below 2 THz in this thesis. The data presented here is from a gold mirror. Since the mirror is highly reflective to THz light, the reflected light would have a very small loss compared to the incidence. As we are aiming to investigate very absorbing biological tissues, naturally the SNR of the detected waves from those water rich tissues will be worse than that from the mirror. As a result, the effective frequency band would be even narrower. Classical de-noising approaches can be used to counteract this problem to some extent [72]. But in this chapter we aim to

improve the situation from a different perspective – by reducing the system variation and baseline artefacts.

3.2.2 System variation

In section 3.2.1, we evaluated the SNR and DR in the frequency domain by multiple or single measurements from a fixed point. In this section, we would like to evaluate the system performance of the raster scanning by focusing on the time domain parameters. As mentioned in Chapter 2, E_{max} and E_{min} are meaningful characteristics for image reconstruction. Thus, in the analysis of the results, these maximal or minimal values and their locations were checked to evaluate the variation of the images. To achieve this, homogeneous samples were preferred for the measurements to ensure no or negligible variation resulted from the tested objects. For this study, the mirror and air were scanned within a defined area of 1cm by 1cm. As usual, point measurements of air and an additional quartz plate were used for the reference and baseline, respectively.

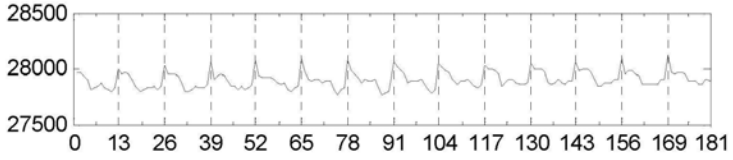

(a)

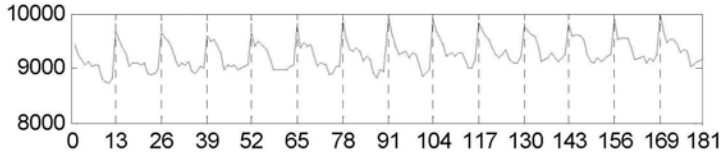

(b)

Figure 3.3: Distribution of the maximal values over the location. (a) From the mirror and (b) from the air. Here the locations are indexed by numbers and the values of the air are absolute. For clarity, the pixels shown here are after downsampling by a factor of 4.

For a perfectly aligned imaging system if we don't consider the fluctuation effects of the laser, since our samples, namely the mirror and air are homogeneous in the examined area, the maximum or minimum amplitudes from the same sample should be expected to be the same. However, we found that there are noticeable variations

over different locations in the x-y plane.

This is illustrated by Figure 3.3, in which we plot the amplitudes (from raw data, arbitrary unit) against the pixel numbers in the horizontal axis (pixel numbers represent the physical locations of the amplitudes). To look more closely at this problem, the same data in Figure 3.3a was used to create an image, in which a false color scheme is used to represent the pulse intensity, as shown in Figure 3.4. Apparent texture can be seen in the figure and it is not as monochromatic as we had expected.

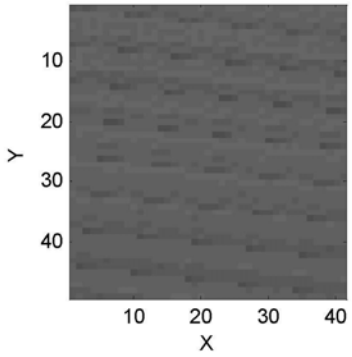

Figure 3.4: E_{min} images from the processed data using the new algorithm.

3.3 A new data processing scheme to reduce the system variation

It is clear that in the proceeding section, the variations during the raster scanning were not negligible. Since biological samples have a natural variation, we must reduce the signal variation due to the system as much as possible in order to reliably determine the terahertz properties of biological samples. To solve the observed problem we have modified the aforementioned deconvolving method (in Chapter 2).

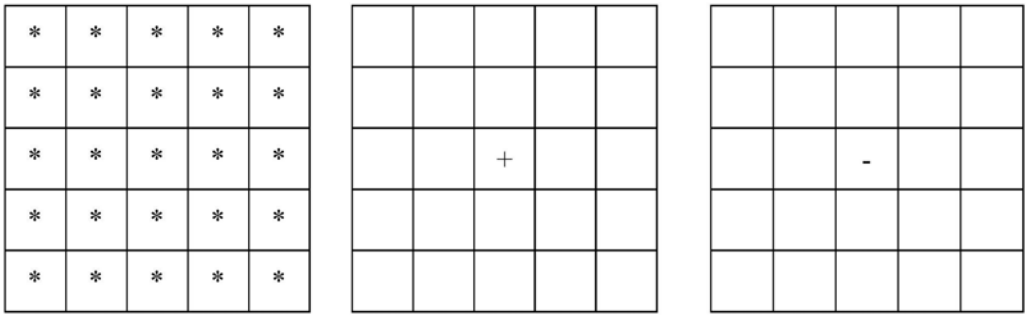

Figure 3.5: Illustration of the old protocol for measurements of (a) sample, (b) reference and (c) baseline. Reference and baseline signals were taken from the fixed point, the central point of the imaging window.

3.3.1 Methodology

The raw data is converted to processed data and the filter function determines the shape of the processed time-domain waveform, removing the dependence on the terahertz device. This is typically done equation by (2.1), where only the sample was raster scanned, while both the reference and baseline were measured once at a fixed point, namely the center of the quartz imaging plate, as illustrated in Figure 3.5. To emphasize this protocol, (2.1) is rewritten as,

$$E_{\text{processed}}(x,y) = \text{ifft}\{\frac{\text{fft}\{E_{\text{Raw}}(x,y) - E_{\text{Baseline}}(0,0)\} * \text{fft}\{\text{filter}\}}{\text{fft}\{E_{\text{Reference}}(0,0) - E_{\text{Baseline}}(0,0)\}}\} \tag{3.1}$$

From their maximal values we can see, although not in linear correlation, the raw data (mirror) and the reference (air) did change in a similar trend over the position. The variations are not due to the samples but due to the scanning process – as the scanning stages move the terahertz beam becomes slightly misaligned and this is exacerbated by any imperfection in alignment of the quartz imaging plate.

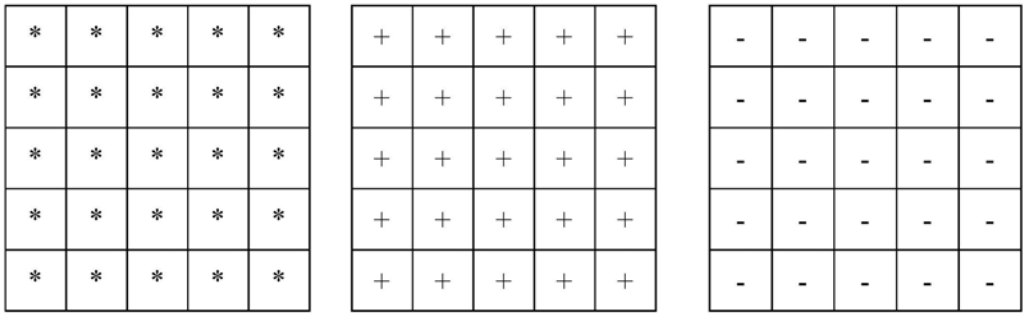

Figure 3.6: Illustration of the new protocol for measurements of (a) sample, (b) reference and (c) baseline. Both reference and baseline were raster scanned as the sample such that all of them can be spatially aligned as in Equation (3.2).

Since both the sample and reference are likely to be similarly affected by the scan position we modify the processing method in (3.1) to include a reference and baseline at each pixel. Image parameters for the reference and baseline were exactly the same as the sample so that all the pixels can be spatially aligned exactly. This new measurement protocol is then illustrated in Figure 3.6. In this way, we can relate the raw data, reference and baseline as,

$$E_{\text{processed}}(x,y) = \text{ifft}\{\frac{\text{fft}\{E_{\text{Raw}}(x,y) - E_{\text{Baseline}}(x,y)\} * \text{fft}\{\text{filter}\}}{\text{fft}\{E_{\text{Reference}}(x,y) - E_{\text{Baseline}}(x,y)\}}\} \tag{3.2}$$

For sample measurements, again 1cm by 1cm area of the mirror was scanned, with 41 and 49 steps in the x and y axes respectively, and totally 2009 pixels (corresponds to 41 by 49) were obtained in a image as before. Air and an additional quartz plate were imaged for the reference and baseline such that (3.2) could be used to recheck the amplitudes of the processed data.

3.3.2 Results

Figure 3.7 shows the results from the different data processing methods. In the time domain, data sets from all the pixels were plotted together, and for clarity we zoomed in near the troughs. Comparing Figure 3.7c with Figure 3.7a we see that the variation in intensity of E_{min} is much lower. Additionally, it is interesting that the waveforms in Figure 3.7c are better aligned, namely the arrival times of the individual minimal values from different pixels sit much closer to each in the time

axis. This is further shown by Figure 3.7b and Figure 3.7d. From them we see that the arrival time of E_{min} in the new processing method is constant throughout the image compared to the range of arrival times seen using the original processing technique.

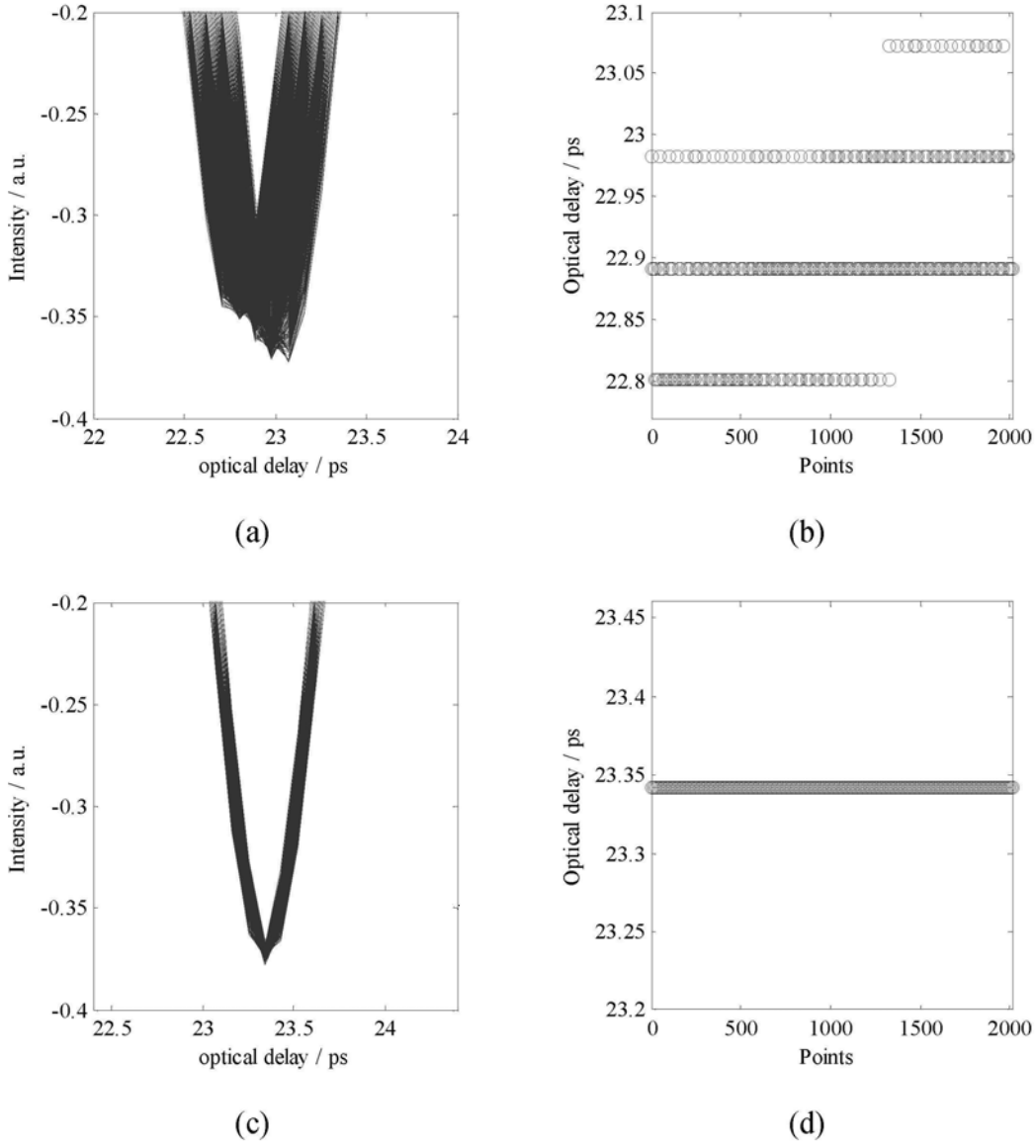

Figure 3.7: Distribution of the minimal values and the arrival time over the location. (a) Minimal values using the old method, (b) arrival time using the old method, (c) minimal values using the new method and (d) arrival time using new method.

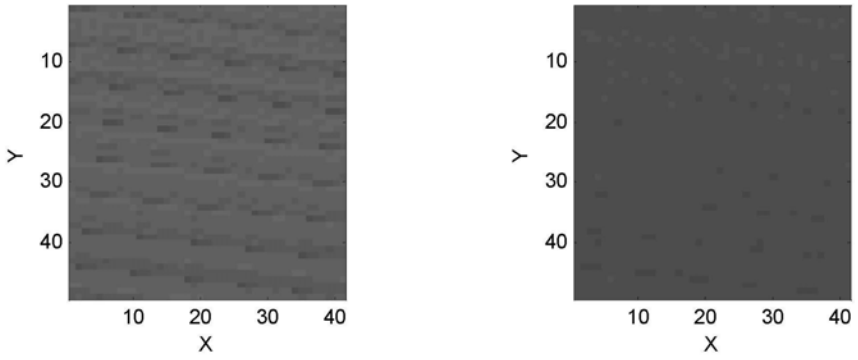

(a) (b)

Figure 3.8: E_{min} images from the processed data using (a) the old algorithm, (b) the new algorithm. Image using the new algorithm was much more homogeneous.

The mean and standard deviation of the E_{min} were also checked and their ratio was defined to quantitatively reflect the variation in different data types. From Table 3.1, it can be seen that the percentage variation of E_{min} was reduced from close to 1.5% to 0.5% by using the new processing method.

To highlight the improvement, again we plot the E_{min} image of the mirror using the original algorithm (Figure 3.8a) and the modified algorithm (Figure 3.8b). We see that Figure 3.8b is much more homogenous than Figure 3.8a, which demonstrates that our new processing method has compensated for and thus reduced signal variation.

3.3.3 Discussion

The exact reason of the observed variation remains to be unknown. We believe it is due to the imperfection of the optics in the system, for example unevenness of the scanning stage during the movement. For the time being, the hardware inside our system is unlikely to be changed. Thus, we managed to minimize its impact by proposing a new algorithm. From Table 3.1 we can see that the new algorithm successfully reduced the percentage variation in E_{min} by a factor of three. In this part, we have limited the data processing in the time domain. In the frequency domain, this idea can also be implemented. For instance, the ratio of the sample spectrum over the reference spectrum is very important for extracting the complex refractive

index (see Chapter 2). Similarly, the sample and reference signals can be spatially aligned to improve the calculations. With reduction of the system variation of the system, better image contrast can be provided.

Table 3.1: Comparison of the Mean and standard deviation of E_{min}

Data type	MEAN	STD	STD/|MEAN| (%)
Raw	8884.7	129.7502	1.4604
Old processed	-0.3512	0.0052	1.4917
New processed	-0.3707	0.0018	0.4886

Averaging is a commonly used approach to remove background noise. Since the temporal resolution for terahertz waveforms is very high, typically less than a hundred femtoseconds, a very small misalignment of the signals can lead to significant error when taking the average. Thus, the terahertz waveforms must be carefully aligned before they are averaged. It is to be noted that the waveforms after the new algorithm was applied were better aligned temporally (see Figure 3.7a and c). This indicates that our proposed approach not only cancels the intensity variation but also can correct the phase information. In this regard, it is useful when the average value of waveforms from a selected area is needed.

3.4 Simulation of noise impact on the complex refractive index

Jepsen *et al* has shown the frequency dependence on the DR may lead to artefacts in the absorption spectrum and obscure the interpretation of the experimental data [74]. In this simulation work, we are going to determine how the SNR affects the both the refractive index and absorption coefficient.

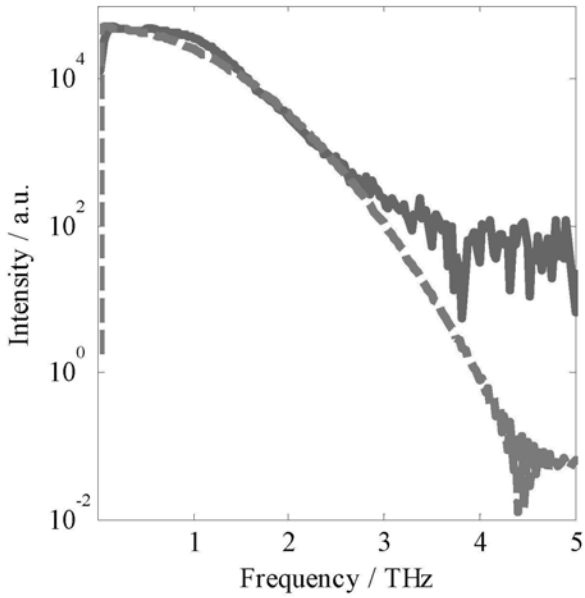

Figure 3.9: Detected spectrum from our system (solid line) and the simulated spectrum (dashed line).

3.4.1 Methodology

In this simulation, the same configuration and parameters as in the system were used. Based on the detected spectra from our system we designed a double Gaussian function to model the incident THz pulse such that the simulated and detected signals can have similar power distributions over the frequency axis. With the air's optical parameters and Fresnel's equation, the spectrum of a reference signal (air) could be calculated and is plotted in comparison with the detected reference spectrum as in Figure 3.9, where we see the two spectra match very well below 2 THz, which was of our interest in this simulation work.

Then we supposed a sample with a broadband refractive index of 2 and a broadband absorption coefficient of 100 (see the dashed lines in Figure 3.10). Similarly, the sample signal could be simulated through Fresnel's theory. From the simulated reference and sample signals, we could extract the sample's complex refractive index to be the same as our supposition.

In the second step, Gaussian white noise was added to both the reference and sample signals. The power of the noise was determined by the sample power (RMS) and a

set value of SNR. Here the SNR was defined in the time domain as the power ratio between the signal (reference or sample) and the Gaussian noise, which was different from our previous discussion in section 3.2.1. By changing the power of the white noise, we generated a series of signals with different SNR values (in dB).

Then these contaminated signals were used to calculate the complex refractive index of the sample. At each noise level, the same step was repeated 50 times.

3.4.2 Simulation results and discussions

In this part, we present the simulated refractive index and absorption coefficient below 2 THz. Based on the SNR value of the signal, the results are divided into 4 groups, namely from 10 dB to 70 dB with a step length of 20 dB, as illustrated in Figure 3.10 to Figure 3.13. In these figures, green solid lines (50 plots in each figure) represent results from simulation, whereas blue dashed lines indicate the supposed complex refractive index of the sample which we defined in the methodology section.

We started from investigating a worst case of signal quality, for example with a SNR of 10 dB and the results are shown in Figure 3.10. In the figure huge differences can be seen between the simulation and the set values (dashed lines). This indicates it would be almost impossible to extract n and α when the signal quality is so bad. When SNR is increased to 30 dB (see corresponding results in Figure 3.11), there is a clear improvement, especially for the lower frequency range, for example below 1 THz where the simulation results are very close to the supposed values. However for the higher frequencies, the deviations are still significant. Thus we conclude that for signals with SNR at the level of 30 dB, the complex refractive index can be resolved in the lower frequency range but the accuracy may not be very good.

Then we continued to increase the SNR to 50 dB and the corresponding results are shown in Figure 3.12. Now we see that the simulation matches quite well with their set values, except for some small deviations in the high frequency end. This indicates that in this case the results can be resolve with a good accuracy.

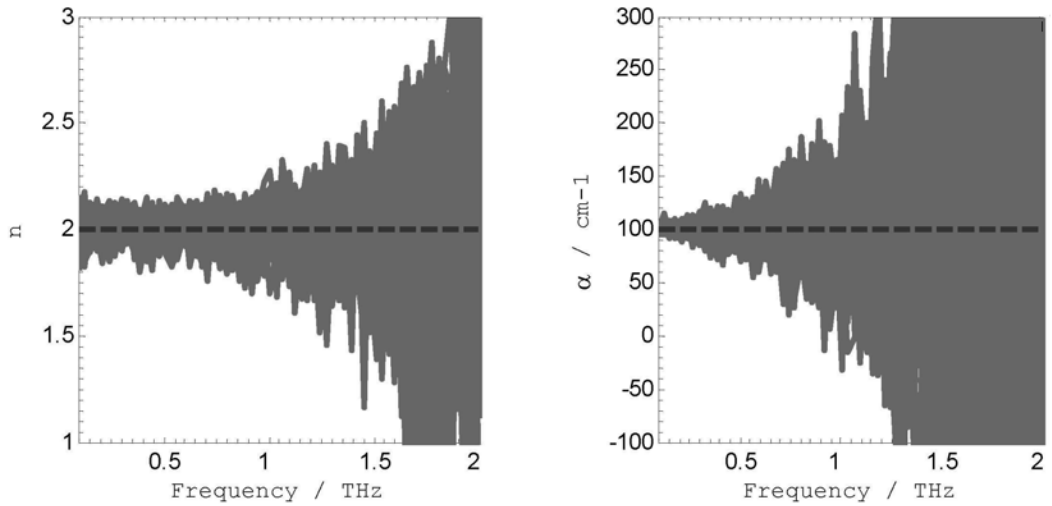

(a) (b)

Figure 3.10: Simulated (a) refractive index and (b) absorption coefficient when the SNR was 10 dB.

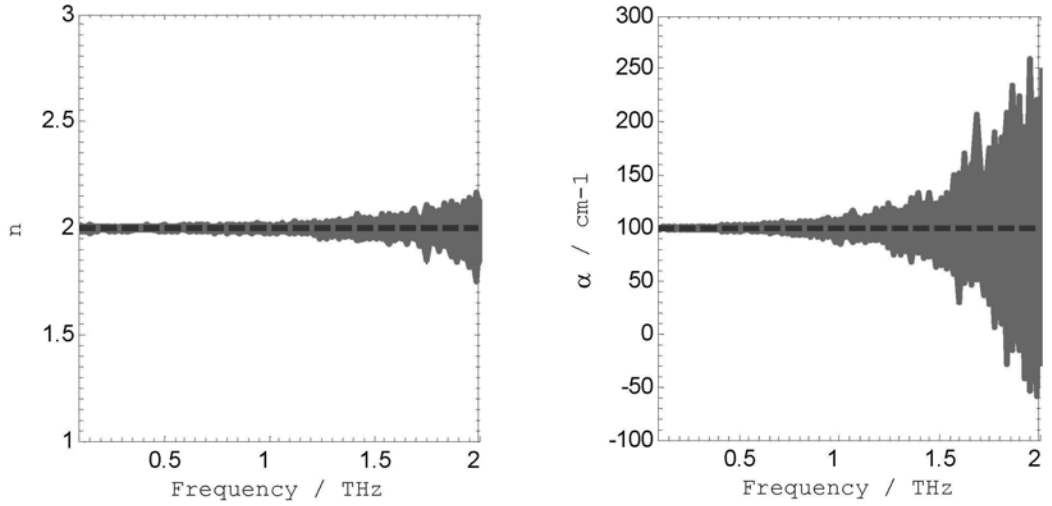

(a) (b)

Figure 3.11: Simulated (a) refractive index and (b) absorption coefficient when the SNR was 30 dB.

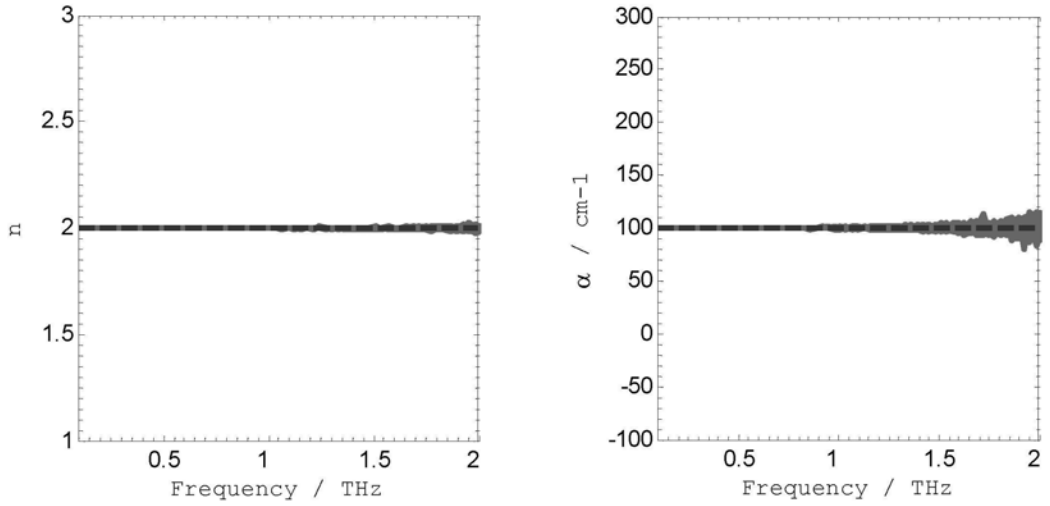

(a) (b)

Figure 3.12: Simulated (a) refractive index and (b) absorption coefficient when the SNR was 50 dB.

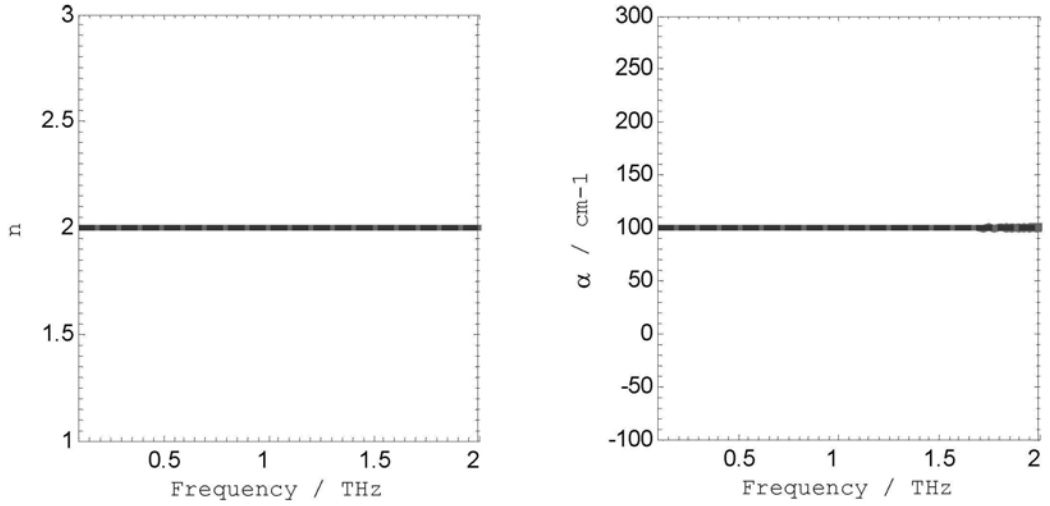

(a) (b)

Figure 3.13: Simulated (a) refractive index and (b) absorption coefficient when the SNR was 70 dB.

In Figure 3.13 the SNR was set to 70 dB and the simulation lines below 2 THz are almost the same as the set lines, which means the complex refractive index can be perfectly determined in the frequency range below 2 THz.

When we extract the complex refractive index of an object, we are particularly interested in their profiles in the frequency domain. For different frequency components, since the individual power is different, the SNR at each frequency would be different. From the spectrum of the mirror in Figure 2.3b, it is clear that the SNR value is decreasing as the frequency increases. The purpose of this simulation work is to get a rough idea on how the noise would affect the calculation accuracy.

In the simulation, since the signal and noise can be generated separately, it is easy to get the SNR of a single signal through the power ratio of the signal and the noise. However, in practice a detected waveform would inevitably be contaminated by the noise and they can hardly be separated. In other words, it is impossible to recover the real signal without any noise. This is why we typically estimate the SNR from multiple trials of detection. It should also be noted that to make the protocol simple, noise added to the reference and sample signals was exactly the same. However, in practice they may be different due to the difference between the air and sample. In this sense, the SNR values we discussed in the simulation may not be the same as in the case of practical estimation. But we did see from the simulation that when the noise level was increased, the accuracy for the complex refractive index would become problematic. More importantly, refractive index and absorption coefficient were similarly affected by the noise.

3.4.3 DR and the accuracy

With the above simulation, we qualitatively looked into the general impact of noise on the optical parameters. In this section, we aim to make a quantitative analysis of the accuracy of the results. To this end, we improved the simulation protocols and the sample spectrum was modeled with uniform power density. When a white noise was added to the sample, since the white noise power was also uniformly distributed, the resulted SNR at all frequency components would be very close to a constant value. Then this value was actually the DR we defined at the beginning of this

chapter. So in this way DR could be related to the accuracy of the results. The sample was the same as we defined in the last section. Once the sample spectrum was determined, the reference spectrum can be derived. Then the remaining steps were repeated as in the previous simulation and the refractive index and absorption coefficient could be extracted. For clarity, here we only show an example when DR was set to 30dB, as in Figure 3.14.

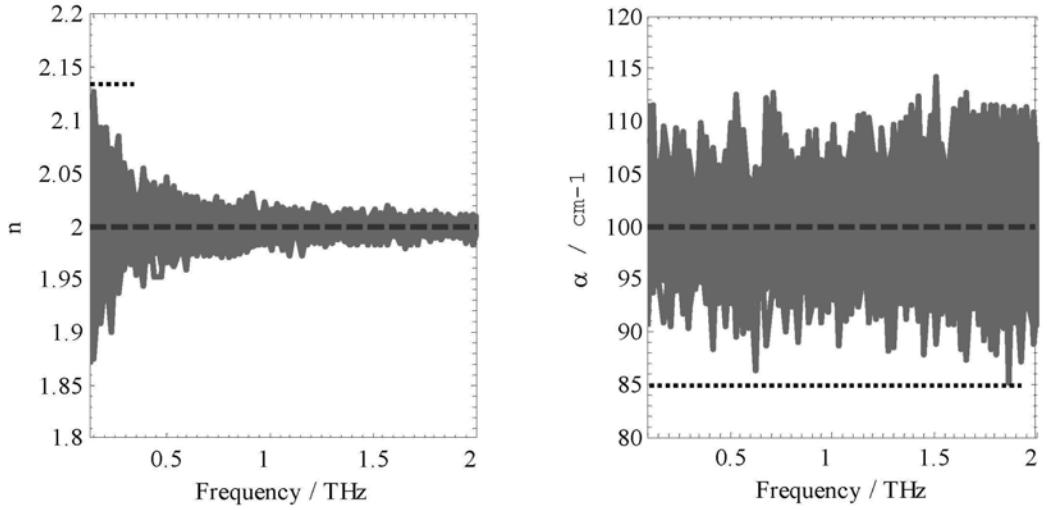

(a) (b)

Figure 3.14: Simulated (a) refractive index and (b) absorption coefficient when the DR was 30 dB.

We see that the difference in n decreases as frequency increases. This means when DR is the same, the calculated refractive index at a higher frequency is more accurate than that at a lower frequency. However, for α, No such clear trend can be seen. The black dotted lines indicate the maximum absolute differences (MAD). We define maximum percentage difference (MPD) as the ratio between MAD and the real value. Then we can use MPD values to represent the system accuracy. When DR was 30 db, MPD values for n and α were calculated to be 6.7% and 15%, respectively. By changing DR to different values, MPD values at different noise levels could be found, as shown in Table 3.2.

Table 3.2: MPD values at different noise levels

DR		10 dB	20 dB	30 dB	40 dB	50 dB	60 dB
MPD	n	100%	20%	6.7%	2.5%	1%	0.25%
	α	100%	45%	15%	5%	1.5%	0.5%

We further plot the above values in Figure 3.15 to show the relationship between MPD and DR. For a sample signal with a particular DR, the corresponding accuracy can be roughly estimated from this relationship, for example, when DR is 35 dB, the accuracy in terms of MPD is about 4.6% for n (or 10% for α). Similarly, when a given accuracy is allowed, the required DR can also be calculated.

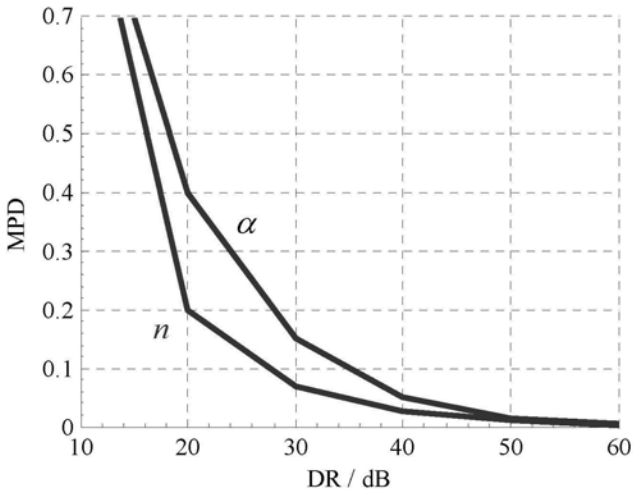

Figure 3.15: Relationship between MPD and DR.

In conclusion, from this simulation work, the percentage difference at a particular frequency was quantitatively related to its corresponding DR of the sample signal. This method can be used to examine the accuracy of the calculation as well as to determine the effective bandwidth of the system for different objects.

3.5 An improved approach to remove baseline artefacts

3.5.1 Introduction

Given the strong attenuation of terahertz radiation by water which is often a large fractional component of biological samples, it is more feasible to perform *in vivo* measurements for medical use in reflection geometry. To date, it has been difficult to extract accurate absorption data in reflection geometry as it is contained within the phase information of the measurement [59] which is sensitive to system artefacts. Previous work by Jepsen *et al* has shown that the frequency dependence of the DR may lead to artefacts in the absorption spectrum and obscure the interpretation of the experimental data [74]. In the beginning part of this chapter, we determined the SNR and DR of our imaging system and in Figure 3.16 it can be seen that the DR is deteriorating rapidly as the frequency increases. For the mirror since it is very reflective to terahertz radiation, the useable band can be up to 2 THz. However, for very absorbing samples the situation will be even worse due the strong attenuation (see plots of water and isopropanol in Figure 3.16) and the resulted effective frequency band will be very limited. Thus for accurate measurements of these samples when the DR is very low, the artefacts should be avoided as much as possible. Previously, it was found there were some differences between our results with those from other systems. We suspect that the discrepancies may be partially introduced from artefacts in our configuration. To this end, we have looked into this problem and developed a new method to remove the baseline artefacts.

3.5.2 Baseline artefacts

In reflection geometry, samples are typically placed on a sample window. The window is made of a material with minimal absorption at terahertz frequencies such as silicon or z-cut quartz. The pulsed terahertz radiation is focused onto the top surface of the sample window (see Figure 3.17a). As the incident THz pulse propagate across the image window, the reflected signal will be the superstition of two parts, namely the reflected pulses from the bottom and surface of the image

window, as illustrated in Figure 3.17b by A and B respectively. Since only pulse B reflects the sample properties, in the detection it is desired to get a clean pulse B without any interference from pulse A. Theoretically, these two pulses are generated at different times and thus they can be separated from the reflected signal by a time window. However, pulse A has an enduring signal or "ringing" which will extend into the region of reflection B (Figure 3.17c). Due to this overlap, the tail cannot be measured directly.

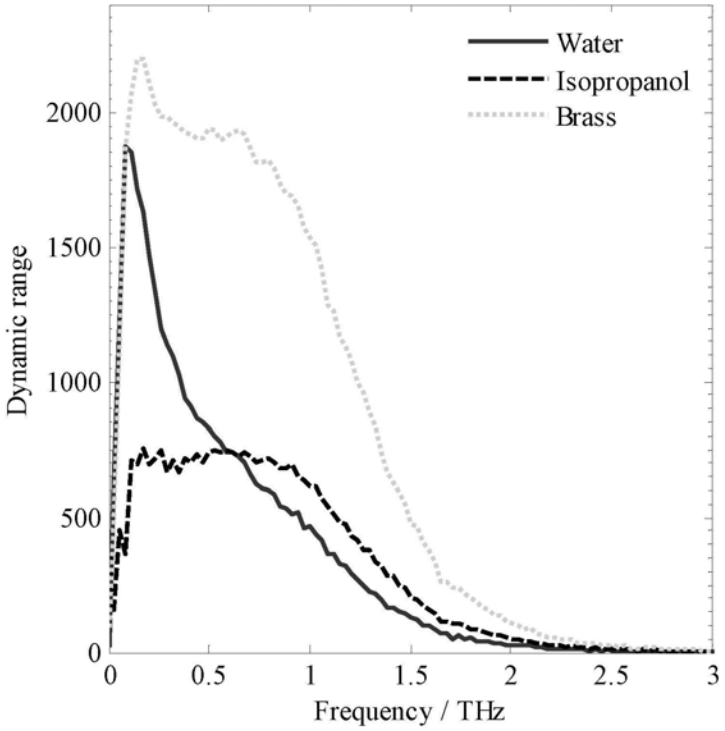

Figure 3.16: Dynamic range distributions over frequency.

Earlier work by Jepsen *et al* has shown how terahertz reflection spectroscopy could be used to characterize alcohol solutions inside bottles [75]. In their work, they use Fresnel equations to simulate expected sample reflections from the inside of the bottle. They report that the experiment reproduces the simulation quite well and that

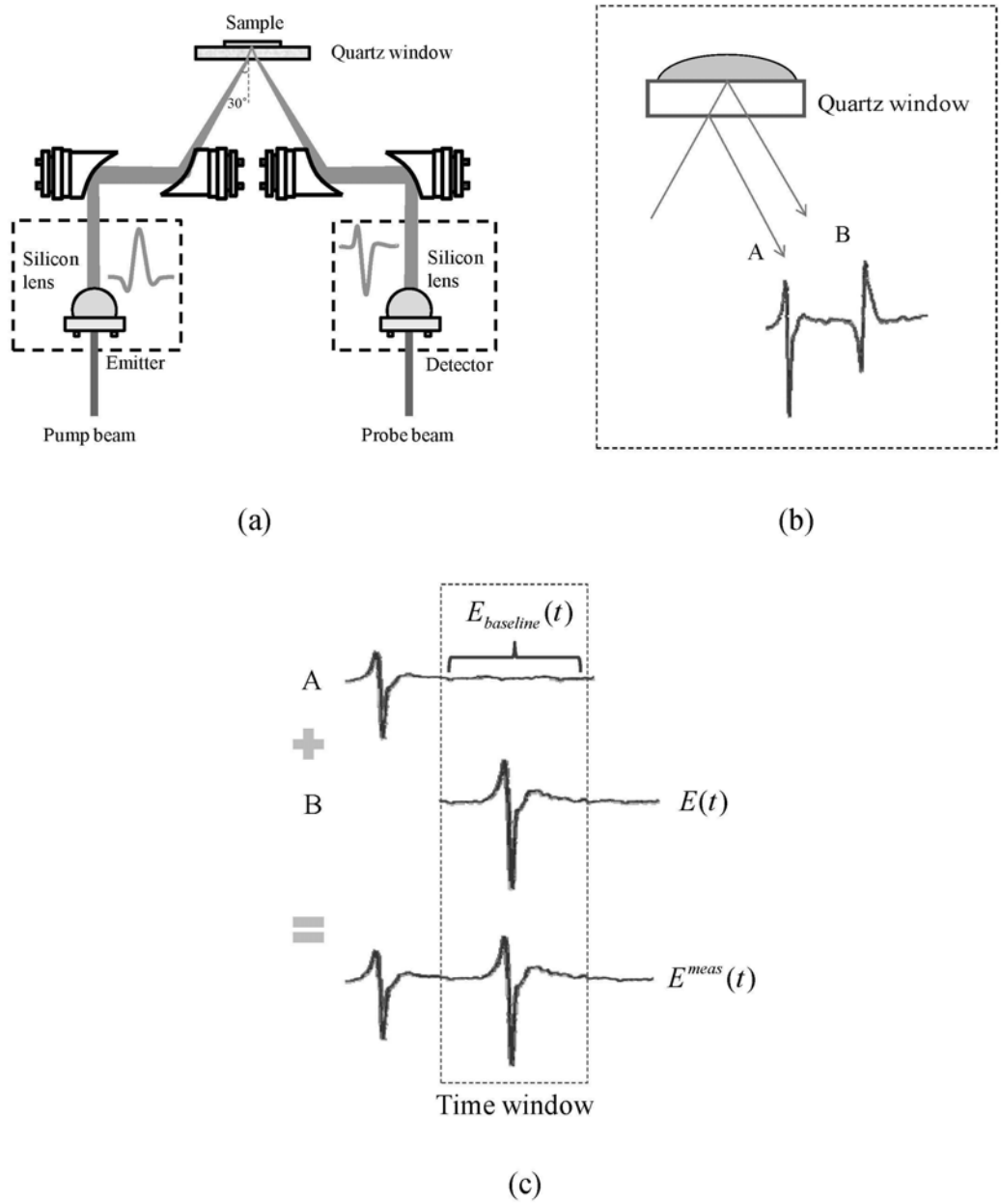

Figure 3.17: Schematic diagrams to illustrate the baseline artefacts. (a) Schematic diagram to illustrate how the terahertz beam is focused on to the quartz window and sample. (b) The resulting reflections of the incident terahertz light are depicted in the large dashed box. (c) The relation between the measured signal $E^{meas}(t)$, real signal $E(t)$ and baseline artefacts $E_{baseline}(t)$.

the experimental details left out of the simulation do not significantly influence the result [75]. In this part, we will exploit the difference between simulated and measured reflections to determine a baseline offset to correct for errors due to the "ringing". This baseline is then used to improve calculations of the complex refractive index in reflection geometry.

Methods to remove the effects of the ringing previously reported have taken a baseline measurement of the sample window with an identical window placed on top [60], in our case quartz, as illustrated in Figure 3.18 (b).

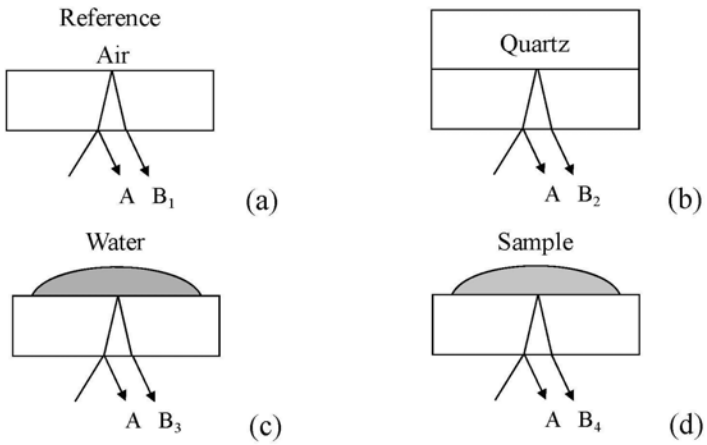

Figure 3.18: Schematic diagrams to illustrate the measurement configurations for reference (a), baseline (b), water (c) and sample (d) data acquisition. Pulse A is the baseline artefacts due to the lower surface of the imaging window. Pulses B_1, B_2, B_3, B_4 are reflected off the top surface of the imaging window.

Since the two windows are identical, there should be no reflection from the interface between the sample window and the second window. The resulting reflection should only represent the effects of the ringing and should be continuous and extend into the region over which to measure reflection A. We refer to this as the "baseline" measurement. However, in practice it is very difficult to achieve perfect contact between the two windows and consequently the measured signal in configuration Figure 3.18b is not only due to the ringing from reflection A but also contains a small reflection (B_2) due to the slight air gap between the windows (which causes a refractive index mismatch). Another possible approach would be to apply a thin layer of index matched liquid to the original window so as to prevent air gaps forming between the two windows. However, in practice it is not possible to perfectly match both the refractive index and absorption coefficient and so this method would also introduce some unwanted reflections. Additionally, in some applications (such as pharmacology) it may be advisable to avoid the use of liquids as any residues may interfere with the result.

Some reflection systems use a thicker window of higher refractive index (such as

silicon) to enforce a greater optical delay between the reflections on the lower and upper surfaces [76]. Additionally since the ringing has further to propagate before it interferes with the sample measurement, it is likely to be weaker. However, it would still be of significance for accurate characterization. In our system we require the window to be optically transparent to improve image registration, using a thicker quartz window could cause unwanted dispersion. In order to determine the sample properties accurately through reflection spectroscopy and imaging, we need to be able to measure the baseline more precisely and reliably. In this work we derive a new approach to achieve this goal. This method can also be easily applied to reflection systems with other angles of incidence or with different window properties.

3.5.3 Theory

Our novel method is to use accurate, room temperature, terahertz pulsed transmission spectroscopy (TPS) data of a standard material such as water to simulate the reflected terahertz pulse for a given input pulse. Pickwell *et al* have previously used double Debye theory in our finite difference time domain simulations of water [77]. In this part we use the measured frequency dependent optical properties of water in conjunction with a measured reference pulse and Fresnel equations to predict the reflection off water. We chose water for this as it will naturally make perfect contact with the quartz window. By comparing the simulated water reflection with the measured water reflection, the effect of the ringing can be determined and this ringing can then be accounted for in calculations of unknown samples such that the optical properties of these samples can be determined more accurately. This process is summarized schematically in Figure 3.19.

The measured electric fields of the pulses reflected off the quartz/air and quartz/water interfaces (corresponding to the reflections B_1 and B_3 in Figure 3.18) in

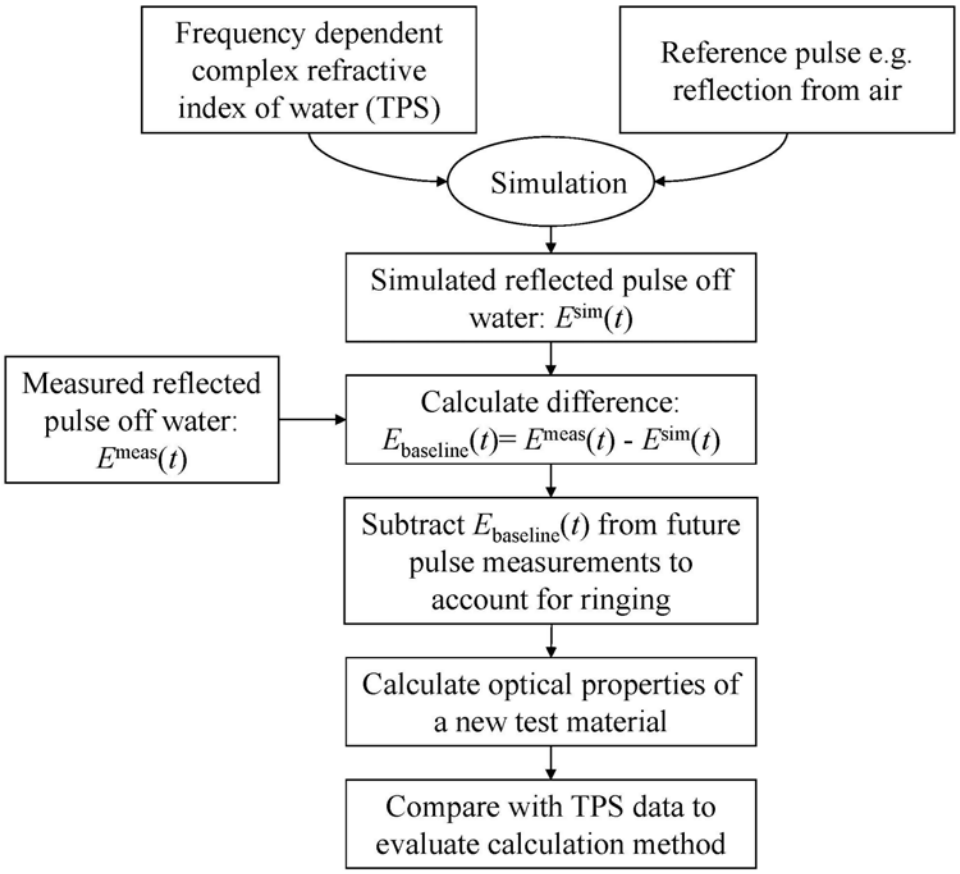

Figure 3.19: Flow chart to summarize the new baseline approach.

the time domain are notated by $E_{air}^{meas}(t)$ and $E_{water}^{meas}(t)$ respectively. The measured electric field is the superposition of the actual reflection due to the interface with the baseline reflection, $E_{baseline}(t)$, due to the ringing:

$$E_{air}^{meas}(t) = E_{air}(t) + E_{baseline}(t) \tag{3.3}$$

$$E_{water}^{meas}(t) = E_{water}(t) + E_{baseline}(t) \tag{3.4}$$

Where $E_{water}(t)$ and $E_{air}(t)$ are the actual reflections in the time domain off the quartz/water and quartz/air interfaces respectively. The reflected time domain pulses are Fourier transformed to obtain the corresponding frequency domain spectra, in this case $E_{water}(\omega)$ and $E_{air}(\omega)$.

For the actual reflected pulses, which are s-polarized in our system, the Fresnel equations and the ratio in chapter 2 can be used again. Here we define M as,

$$\begin{aligned} M &= \frac{E_{\text{water}}(\omega)}{E_{\text{air}}(\omega)} \\ &= \frac{\left(\tilde{n}_{\text{quartz}}\cos\theta_{\text{quartz}} - \tilde{n}_{\text{water}}\cos\theta_{\text{water}}\right)\left(\tilde{n}_{\text{quartz}}\cos\theta_{\text{quartz}} + \tilde{n}_{\text{air}}\cos\theta_{\text{air}}\right)}{\left(\tilde{n}_{\text{quartz}}\cos\theta_{\text{quartz}} + \tilde{n}_{\text{water}}\cos\theta_{\text{water}}\right)\left(\tilde{n}_{\text{quartz}}\cos\theta_{\text{quartz}} - \tilde{n}_{\text{air}}\cos\theta_{\text{air}}\right)} \end{aligned} \tag{3.5}$$

Where, $\tilde{n} = n(\omega) - i\frac{c}{2\omega}\alpha(\omega)$ is the frequency dependent complex refractive index of a medium with refractive index n and absorption coefficient α. The angle of incidence of the light entering the quartz is θ_{quartz}, and the angles of refraction in air and water are θ_{air} and θ_{water} respectively. Values for $\tilde{n}_{\text{air}}$ and θ_{air} are known. Spectroscopy data acquired in transmission geometry are used for calculating $\tilde{n}_{\text{quartz}}$ and $\tilde{n}_{\text{water}}$. The angles θ_{quartz} and θ_{water} can be calculated from Snell's law:

$$n_{\text{quartz}}\sin\theta_{\text{quartz}} = n_{\text{air}}\sin\theta_{\text{air}} = n_{\text{water}}\sin\theta_{\text{water}} \tag{3.6}$$

From the above three equations, we obtain the following formula for $E_{\text{baseline}}(\omega)$:

$$E_{\text{baseline}}(\omega) = \frac{E_{\text{water}}^{\text{meas}}(\omega) - M \cdot E_{\text{air}}^{\text{meas}}(\omega)}{1 - M} \tag{3.7}$$

Where $E_{\text{water}}^{\text{meas}}(\omega)$ and $E_{\text{air}}^{\text{meas}}(\omega)$ are the Fourier transforms of $E_{\text{water}}^{\text{meas}}(t)$ and $E_{\text{air}}^{\text{meas}}(t)$ respectively. The simulated $E_{\text{baseline}}(t)$ can then be calculated by taking the inverse Fourier transforms of $E_{\text{baseline}}(\omega)$ in (3.7). This simulated baseline is then used to calculate the actual reflected pulse:

$$E(t) = E^{\text{meas}}(t) - E_{\text{baseline}}(t) \tag{3.8}$$

The actual electric field is then used to obtain the complex refractive index of a test

material following the steps we introduced in Chapter 2.

3.5.4 Results and discussion

To test the above theory, we performed room temperature measurements of air, quartz, distilled water and isopropanol using our reflection terahertz imaging system. The liquid samples were placed on the quartz window to form a depth of at least 1 mm to ensure the reflection off the liquid/air interface was excluded from the detected signal.

For each measurement, a small area of the sample was raster scanned and a grid of pixels (25 by 25) was collected. These measurements were repeated four times and the mean values are used for this study.

Calculated baseline

Using the measurements of water and air, we calculated the simulated baseline using the theory above. The result is plotted in Figure 3.20 along with the measured baseline using the extra quartz window (as illustrated in Figure 3.18b). From the time domain waveforms, it can be seen that the intensities of both these two baselines are of the same order. However, considerable difference lies in their main pulses (from 15 to 25 ps).

Baseline validation

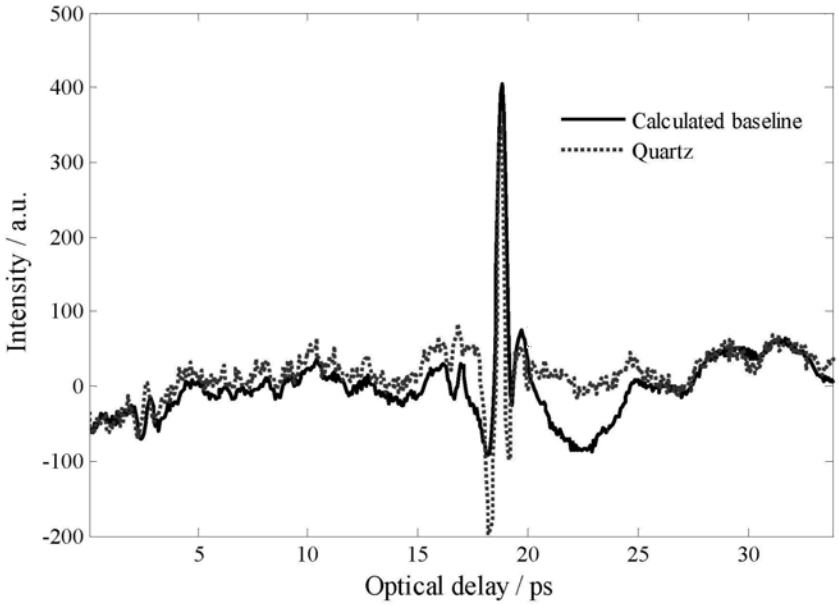

Figure 3.20: Time domain waveforms of the calculated baseline (using the proposed method) and the measured baseline (by measuring an additional quartz plate).

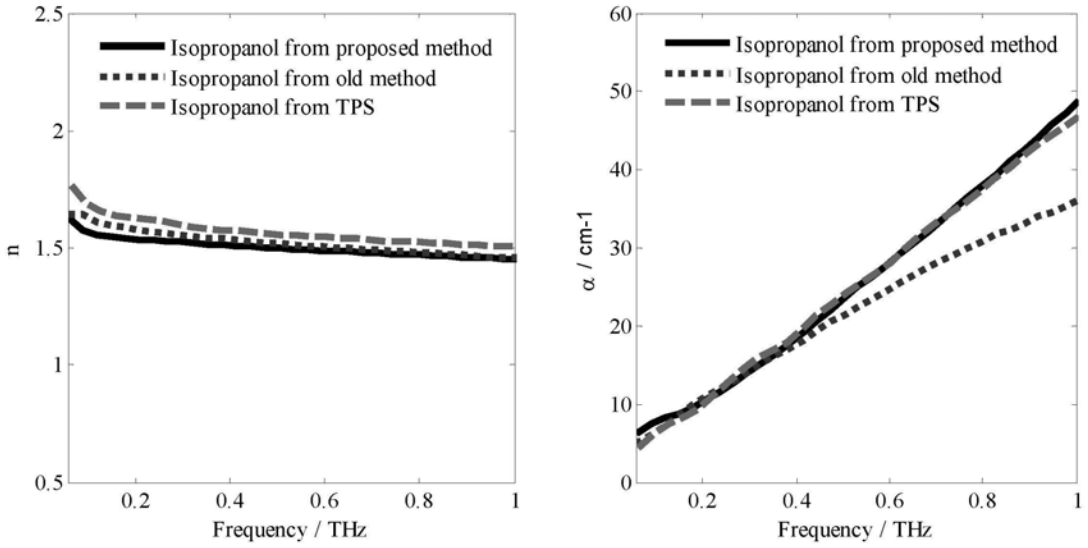

(a) (b)

Figure 3.21: The refractive index (a) and absorption coefficient (b) of isopropanol using our proposed baseline method and the old baseline method compared to those from TPS measurements.

We have calculated the optical properties of our test material, isopropanol, using the

new simulated baseline and compared them in Figure 3.21 to those obtained by the old baseline method (measured with the extra quartz window in place). Additionally, we have transmission spectroscopy data of the isopropanol which can be considered to be the most accurate data for the sample.

As we can see from Figure 3.21b, the absorption coefficient calculated using the new baseline method matches the TPS data much more closely than when the old baseline was used in the calculation. This is most likely to be because when calculating the optical properties in reflection geometry, the absorption coefficient is predominantly dependent on the phase information and this is very sensitive to the experimental setup and protocol. Since the water makes perfect contact with the quartz sample window, our method using the water data to determine the baseline has more accurate phase information than the baseline from placing a quartz window on top of the sample window and thus the absorption coefficient calculation is much improved and the frequency range of agreement with the TPS data is approximately doubled from 0.5 THz to up to 1 THz. This is also relevant to biomedical applications as the most interesting frequency range for tissue measurements has been shown to be up to 1 THz [41]. The improvement is not so pronounced for the refractive index data. In reflection geometry the refractive index is predominantly dependent on the amplitude rather than the phase and so is well determined in both our calculations. Conversely, the TPS refractive index is predominantly dependent on the phase information and so is potentially less reliable than the refractive index calculated in reflection geometry. However to compensate for this, the TPS data is acquired over a longer time delay with multiple averaging and so only a slight discrepancy is seen between the TPS data for both refractive index calculations in the frequency range below 1 THz.

The absorption coefficients of the proposal are replotted in a wider range (to 2 THz) as in Figure 3.22, in which DR profile of the isopropanol is also added. It is clear that DR in the region from 0.2 to 1 THz is about 42 dB. From Table 3.2 and Figure 3.15, we know the accuracy of absorption coefficient in this region can be as good as less than 5%. DR decreases rapidly in the frequency range above 1 THz and this will directly lead to a deteriorating accuracy. That is why we see a larger discrepancy in that region.

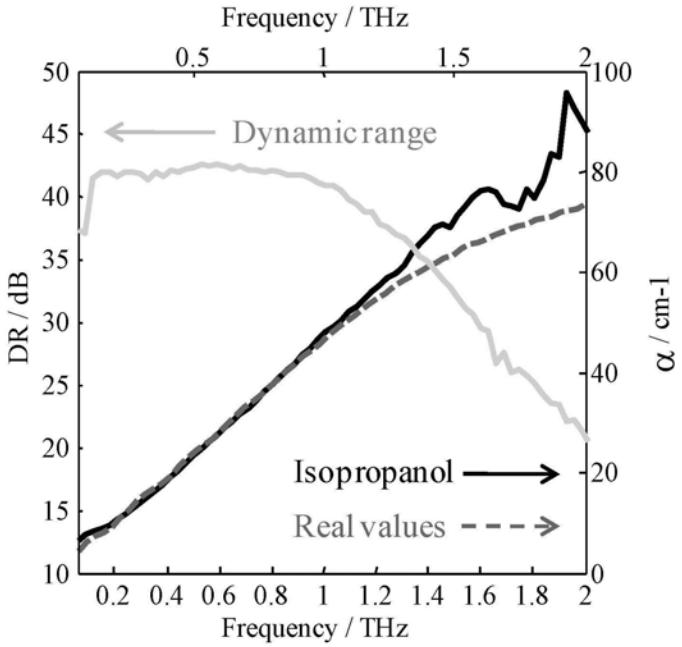

Figure 3.22: Absorption coefficient and corresponding dynamic range of isopropanol.

As we have mentioned, for terahertz pulsed imaging, the impulse function in the time domain is important for signal processing as well as terahertz image reconstruction. It is typically deconvolved from the measured sample and reference signals [40, 78]. The impulse response of a sample can also be improved by this new baseline method as in (3.9), where the Gaussian filter is applied to remove both the low and high frequency noise components as before.

$$\mathrm{FFT}(\text{Impulse function}) = \mathrm{FFT}(\text{filter}) \times \frac{\mathrm{FFT}(E_{\text{sample}}^{\text{meas}}(t) - E_{\text{baseline}}(t))}{\mathrm{FFT}(E_{\text{air}}^{\text{meas}}(t) - E_{\text{baseline}}(t))} \tag{3.9}$$

In conclusion, using dielectric parameters of water and air, we simulate the ringing artefacts introduced by the reflection off the lower surface of the image window. By incorporating this ringing effect in the calculation for refractive index and absorption coefficient, the accuracy can be significantly improved.

3.6 Summary

In this chapter, we evaluated the system performance from different angles and

proposed two novel algorithms to enhance the system accuracy. First, the SNR and DR were determined in the frequency domain. From the SNR and DR we can see the ideal usable band for our system is roughly below 2 THz. In the simulation, we investigated the noise impact on the optical parameters and developed a method to quantitatively assess the accuracy of the calculation.

By checking the time domain parameters, we evaluated the system variation. It was found that when the system performed a raster scanning, the signals varied significantly with location. Based on our observations, a new algorithm was developed. By relating both the reference and baseline with location, the system variation was successfully reduced by a factor of three. System artefacts introduced by time-gating techniques can greatly affect the calculations. To this end we proposed a new method to account for the ringing artefacts observed in terahertz pulsed reflection imaging due to the lower surface of the sample window required in the majority reflection imaging and spectroscopy systems. Using this baseline approach, accuracy of the absorption coefficient has been significantly improved. Through the simulation work, we found that both the refractive index and absorption coefficient were similarly affected by the SNR. It indicates that the baseline problem is another different issue which has little to do with the SNR. The straightforward protocol in the proposed method enables the reference measurements to be taken reliably and easily such that the effects of the ringing and subsequently other system artefacts can be determined and accounted for in calculations. In this way we can improve calculations of the complex refractive index in reflection geometry over a greater frequency range. With these improvements, we hope the system can allow more reliable characterization of complex objects such as biological tissues.

Chapter 4

Terahertz time-of-flight technique

4.1 Introduction

In the preceding parts, all the discussions are based the assumption that only the reflection from the window-sample interface is used in the algorithms. However, for a less absorbing substance with layered structures, later reflections indeed can be utilized for further characterizations. Generally when a THz pulse is incident on such a target, a train of pulses will be reflected back from various interfaces, namely the surface or sub surfaces. For each individual pulse in the detected signal, the amplitude and timing would be different and can be measured precisely. The principle of time of flight technique is to estimate the depth information of the internal dielectric profiles of the target through the time that is required to travel over a certain distance. This unique feature permits looking into the inside of optically opaque material and it has been used for THz 3D imaging. Among the earliest demonstrations of THz 3D imaging, Mittleman *et al* imaged a conventional floppy disk [23]. In their work the various parts inside the disk were identified and the discontinuous refractive index profile was derived. This method was further extended into terahertz reflection computed tomography [79, 80], where the target was rotated to provide back reflection from different angles. In a similar way to x-ray CT imaging, the filtered backprojection algorithm was applied to reconstruct the edge map of the target's cross-section.

4.2 Relation of the thickness, time and refractive index in our system

In the time-of-flight technique, one main task would be to retrieve the depth profile of the object. For a given layer, two reflections will be created by its top and bottom surfaces. In general, the depth information is determined by the temporal difference of these two reflections and the wave propagating velocity in it. However, this relation may take different forms in different system configurations.

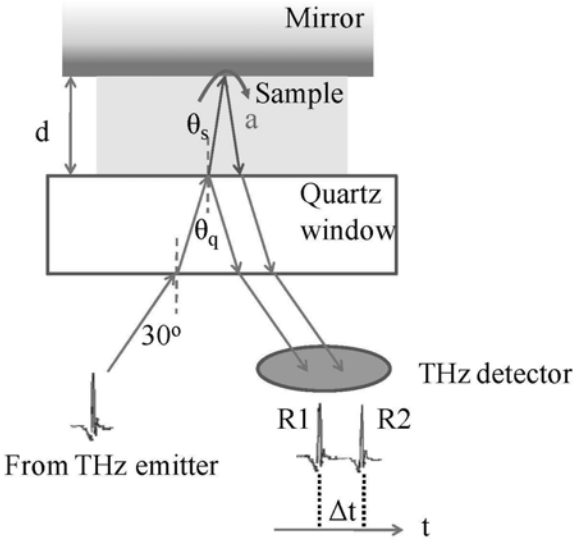

Figure 4.1: Diagram of the time-of-flight configuration in our system with the detector parallel to the quartz plate. (a) Photograph of the image window and the sample with a mirror on top. (b) Illustration of the optical path length and temporal differences.

Consider the configuration with a glass slide sandwiched by the image window and a mirror in our system as in Figure 4.1b. The detector was initially mistaken as parallel to the quartz window. This means that the optical lengths of the two pulses, namely A and B, from the bottom quartz bottom to the detector were the same. Thus, the only difference would be that pulse B had an extra path across the sample, namely a as indicated in Figure 4.1b. Then the travel time in the slide, Δt can be found:

$$\Delta t = \frac{a}{c / n_s} \tag{4.1}$$

Here c is the light velocity in vacuum and n_s is the refractive index of the slide. In the geometry, we can get a as,

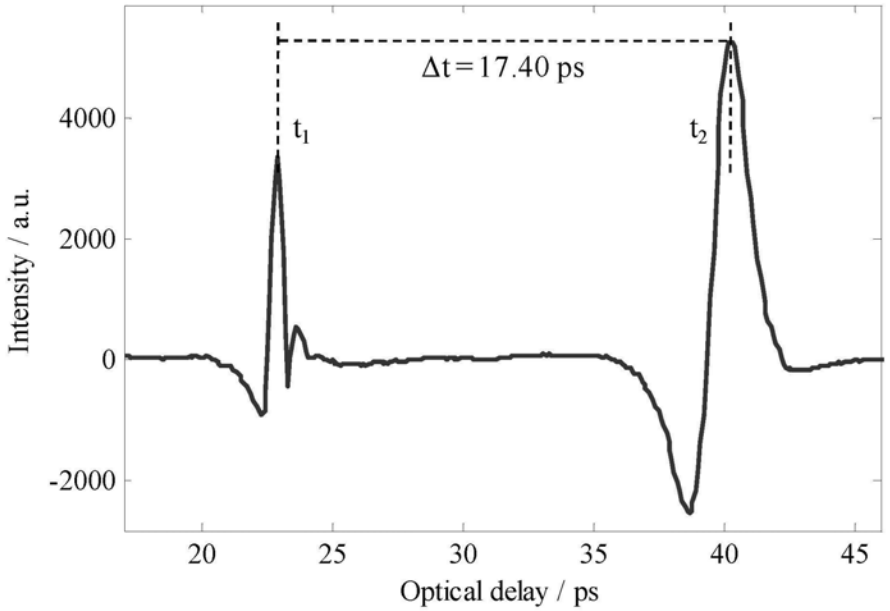

Figure 4.2: Waveform detected from the slide. The two peaks were reflected from the top and bottom surfaces of the slide and their time difference Δt can be used to calculate the thickness of the slide.

$$a = \frac{2d}{\cos\theta_s} \tag{4.2}$$

Here d is the thickness of the slide and θ_s is the angle of refraction in the slide. From (4.1) and (4.2) d can be related with a as,

$$d = \frac{\Delta t * c * \cos\theta_s}{2 * n_s} \tag{4.3}$$

In this equation, n_s has already been characterized, θ_s can be calculated from Snell's law as before and from the detected waveform the temporal difference can be obtained to be 17.40 ps (see Figure 4.2). Thus using (4.3) d can be calculated to be 0.99 mm. However, there is a considerate difference when comparing it with the real thickness 1.05, which was measured by a vernier caliper. This discrepancy was observed in similar tests of other objects. Thus, the equation for the thickness may not be in the right form.

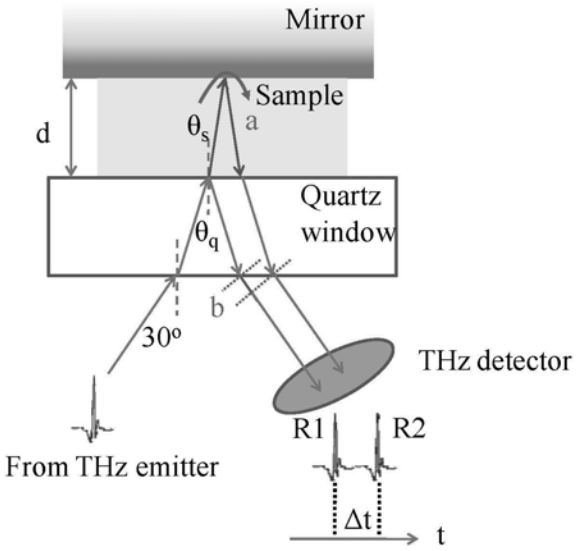

Figure 4.3: Diagram of the correct time-of-flight configuration in our system with the detector perpendicular to the outcoming THz beam.

After careful inspection, we found the detector is mounted perpendicular to the outcoming THz beam as shown in Figure 4.3. In the correct configuration, the temporal difference would be not only due to the path in the slide but also due to the optical length difference b. Thus in the new configuration the correct form of Δt should be,

$$\Delta t = \frac{a}{c/n_s} - \frac{b}{c/n_a} \tag{4.4}$$

Here n_a is the refractive index in the air and b can be further found from the geometry consideration,

$$a = 2d * \tan\theta_s * \sin 30° \tag{4.5}$$

By substituting (4.5) into (4.4), we can get,

$$d = \frac{\Delta t * c}{2 * n_s * \cos\theta_s} \tag{4.6}$$

This new equation was used to calculate the thickness and the result is 1.03 mm. Given the precision of the system, this time the result is thought to be in reasonable agreement with the slide's real value. Comparing (4.3) and (4.6), we can see that a factor of the square of $\cos\theta_s$ is corrected.

4.3 Feasibility study of burn assessment

4.3.1 Burn diagnosis

Burn wounds are common in daily life and nearly two million burn injuries are reported each year in the United States [81]. During the diagnoses and treatments of the severe injuries, burn depth assessment is a significant step. In hospitals, this is primarily done by clinical subjective evaluation and other auxiliary imaging methods, such as thermography [82], Indocyanine Green Video (ICG) angiography [83], Laser Doppler Imaging (LDI) and Laser Doppler perfusion Imaging (LDPI) [84]. These conventional imaging modalities have some limitations and weaknesses [85]. For example, ointments and wound dressings can significantly reduce the accuracy of depth measurements in the above techniques. A reliable non-invasive method that can accurately assess the burn depth would greatly facilitate clinicians' diagnosis.

Since the THz waves can penetrate several hundreds of microns into the skin and most of the burn injuries are superficial, this opens up the possibility of employing terahertz techniques for burn assessment. Several studies for this purpose have been reported [4, 69, 86]. The waveforms and optical parameters of the burned wounds were investigated and terahertz images have shown contrast between burn-damaged tissue and healthy tissue. Their results indicate that terahertz imaging may be promising in evaluating skin burn severity, especially for characterizing burn areas. As we pointed out, the time of flight technique is able to reveal the depth profile thus could be used to evaluate burn depth. However, none of them tried to focus on the depth aspect. In this part, I will present our pilot study and look into the feasibility of doing so.

4.3.2 Materials and methods

Normal skin comprises three different layers: the stratum corneum, epidermis, and dermis (see Figure 4.4). Because of the limited ability of penetration in skin tissues, we do not see the reflection from the epidermis/dermis interface. However, we are able to see the reflection from the stratum corneum/epidermis interface on the palm of the hand and are thus able to measure the depth of stratum corneum. Such research and results have been well reported [40]. In this part, we measure the

thickness of the stratum corneum on a healthy palm beneath a plaster to determine the feasibility of measuring the depth of a burn beneath a dressed wound.

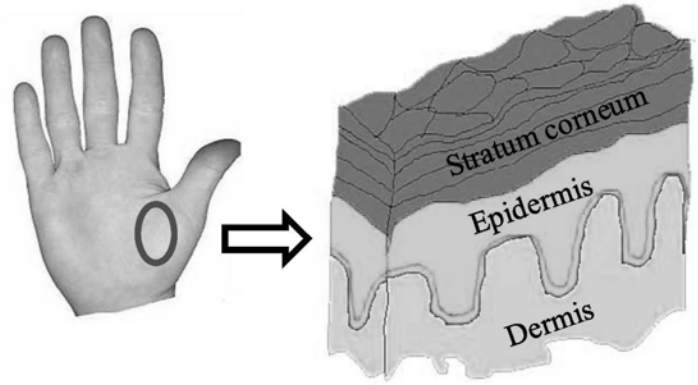

Figure 4.4: Superficial structure of the palm consisting of three layers. Only pulses reflected off the stratum corneum can be seen by our THz system.

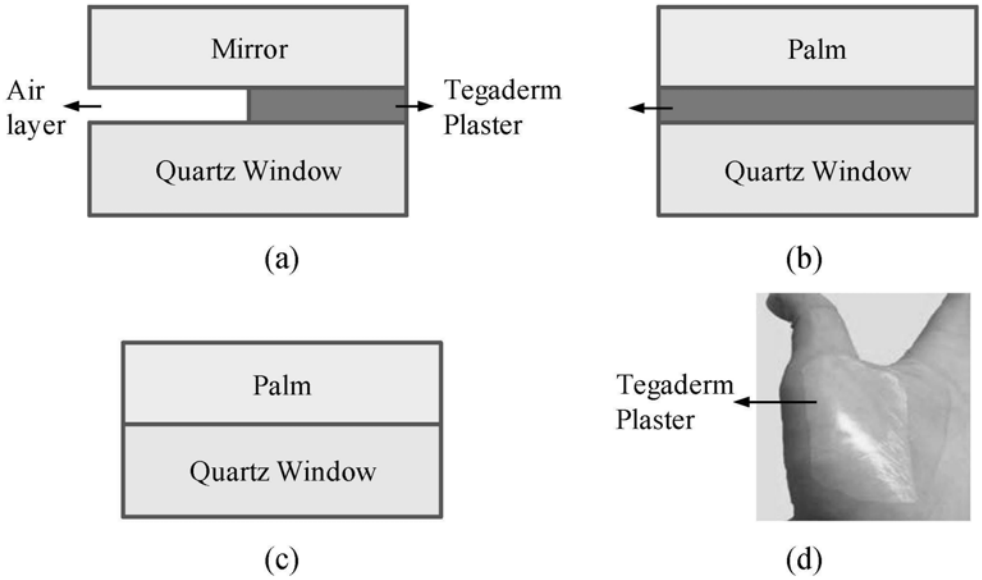

Figure 4.5: Measurement geometry for (a) palm only, (b) palm and plaster, (c) Plaster and air gap with mirror and (d) optical picture of palm and plaster.

To study the effects of a plaster, we first measured the palm *in vivo* directly against the quartz imaging plate (Figure 4.5a), and then beneath a plaster (Figure 4.5b). Lastly, the properties of the plaster layer were investigated. The plaster used was a Tegaderm^{TM} plaster (from Nexcare 3M^{TM}, US), as this can be used as a burns dressing. To measure the refractive index of the plaster, it was carefully stuck to the quartz window as illustrated in Figure 4.5c. Since the thickness of a single plaster

layer is beyond the resolution of our system we put five layers of plaster together.

When a terahertz pulse reaches a boundary between two media of different refractive index, part of the pulse will be reflected back and part of it will be transmitted. Reflections from different depths will have different optical time delays; these time delays along with refractive index information can be used to estimate the layer thickness. For each layer, the relationship between thickness, optical delay and the refractive index is given by the corrected equation (4.6). Processed dada type was used in the calculations.

4.3.3 Results

Palm

Firstly, the palm on the quartz window was measured. The processed time-domain waveform is shown in Figure 4.6. In the figure, there are 2 troughs, which correspond to the top and bottom surface of the stratum corneum. The optical delay between them was about 2.43 ps, as denoted by t in Figure 4.6. Using the above equation to calculate the thickness of this layer, and assuming the refractive index of the stratum corneum is 2 [40], the estimated thickness is 188 μm. It can be seen there is also a small peak before the troughs and this is thought to be due to surface dryness on the stratum corneum. This is also consistent with previous work [40].

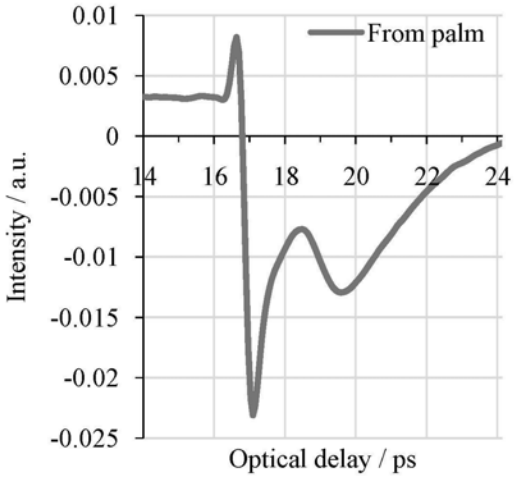

Figure 4.6: Measured pulse from the palm. The two troughs were reflected off the top and bottom surfaces of the stratum corneum respectively.

$$d = \frac{\Delta t * c}{2 * n_s * \cos\theta_s} \tag{4.7}$$

the plaster and not the quartz. It is the properties of the plaster that are affecting the peak and first trough, and so in the next step we shall determine the refractive index of the plaster. However, the two troughs are still clear and can be used to calculate the thickness of the stratum corneum – in this case the optical delay is 2.30 ps which corresponds to a thickness of 178 μm.

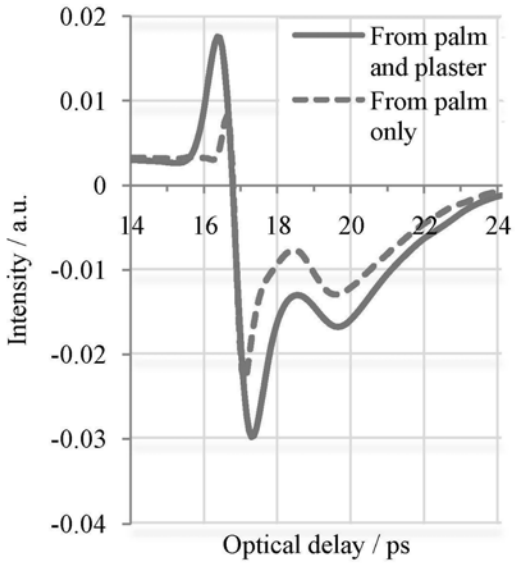

Figure 4.7: Measured pulses from palm and the plaster layer.

Therefore, although the first peak and trough are altered in intensity, the two troughs can still be used to calculate the thickness of the stratum corneum with reasonable accuracy.

Tegaderm plaster

In this step, we determine the properties of the plaster in order to understand why the peak and first trough intensities are affected. We were unable to resolve a single layer of the plaster, so five layers were stuck together to form a plaster layer and then a mirror was placed on top, with part of the mirror over-hanging (Figure 4.5c). With this geometry the waveform reflected from the air gap/mirror can be measured to calculate the thickness of the five layers of plaster. The optical delay between the reflection from the top surface of the quartz window and the mirror, when passing

through the air was 1.38 ps which, from equation (4.6), corresponds to a distance of 239 μm. Therefore the thickness of a single layer of plaster is approximately 47.8 μm.

The Fresnel equation, given by (4.8), was used to determine the refractive index of the plaster.

$$R = \frac{n_q \cos\alpha - n_p \cos\beta}{n_q \cos\alpha + n_p \cos\beta} \tag{4.8}$$

Where n_q and n_p represent the refractive index of the quartz and the plaster respectively; α is the angle of incidence at the quartz-plaster interface; and β is the angle of refraction in the plaster. R is the reflection coefficient of the quartz-plaster boundary and is given by:

$$R = \frac{I_2}{I_1} \tag{4.9}$$

Where, I_1 and I_2 are the intensities of the incident and reflected pulses respectively. In this experiment, I_1 was measured by putting a mirror on the quartz window, while I_2 was measured with plaster only as the sample.

The angles of incidence were calculated using Snell's law and noting that the angle of incidence in free space at the bottom surface of the quartz is 30°:

$$n_p \sin\beta = n_q \sin\alpha = n_{air} \sin 30^\circ \tag{4.10}$$

Since the measured reflected intensities had a small variation, the estimated range of the refractive index of the plaster was from 1.54 to 1.66, with a typical value (mean value) of 1.62.

Table 4.1: Comparison of the calculated thickness of SC

This work (by TPI) thickness (optical delay)	E. Pickwell [40] (by TPI)	M. Egawa [87] (by Raman spectroscopy)
188±20 μm (2.43±0.20 ps) 178±12 μm (2.30±0.13 ps)	170±8 μm	173±40 μm

4.3.4 Discussion

Table 4.1 provides a comparison between the measured thickness of the stratum corneum and those reported by TPI and Raman spectroscopy. Our results are slightly greater than them. This is likely due to the fact that thickness of the stratum corneum may vary from one people to another. Additionally, from the work by Egawa *et al* [87] it can be seen that even for the same palm, the thickness can vary a lot in different locations. In our measurements, the sampling period is about 0.066 ps, which corresponds to a theoretical axial precision of 6.5 um (in this case, the refractive index is 2). Taking this into consideration, the discrepancy between the measurements is acceptable.

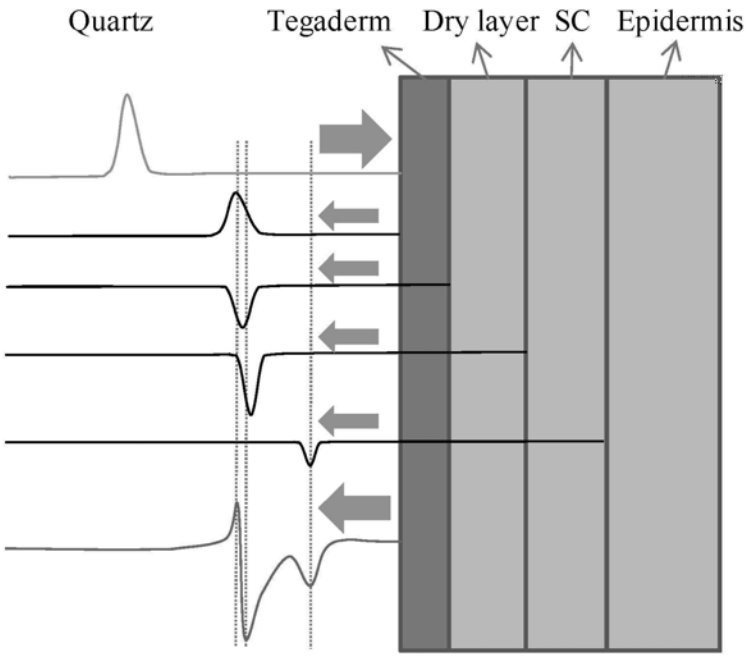

Figure 4.8: Schematic representation of the reflections off the plaster layer and the palm.

To understand the measurement of the plaster and palm together, we can theoretically divide the system into four layers, i.e. the plaster, dry layer on the skin surface, stratum corneum and the epidermis, as shown in Figure 4.8. In each interface of two adjacent layers, there will be a reflected pulse. As a result, for each interface, in the detected waveform there should be either a peak or a trough representing it. So for the measurements in the second step of the plaster and palm, the total number of the peaks and troughs should be four. But in Figure 4.7, we can only see three. The reason for this is that the reflection from the plaster-dry layer

interface constructively interferes with the reflection from the dry layer-stratum corneum interface. The two reflections are so close together (due to the dry layer being so thin) that they cannot be resolved and we just see one trough, but of lower intensity. The reflections interfere constructively because at both interfaces the pulse is entering a medium of higher refractive index and so they both experience the same phase change. Our measurement of the refractive index of the plaster (1.62) is consistent with this as we are assuming the refractive index of the stratum corneum is 2 and that the refractive index of the dry layer is only slightly lower than 2. Finally, the reason we see a higher intensity peak in the plaster-palm measurement, is that like the reflection from quartz to the surface dryness layer, the reflection from the quartz-plaster interface does not have a phase change (as it is from a higher to lower refractive index), so we still see a peak. However, the layer of plaster is around 47.8 μm which is thicker than the surface dryness layer and so the reflection is able to become more established before the next reflection, which deconstructively interferes (as the pulse is reflected from a region of higher refractive index). Thus the plaster enables a higher intensity peak to form.

In conclusion, we have used terahertz pulsed imaging to measure the thickness of the stratum corneum on the palm of the hand beneath a Tegaderm^{TM} plaster *in vivo*. In addition, we have calculated the refractive index and thickness of the plaster.

These results show that terahertz light is able to penetrate through wound dressings to reveal the skin depth information. This therefore indicates that terahertz imaging is likely to be able to detect and measure changes to the stratum corneum and epidermis which could for example, be caused by burns.

4.4 Refractive index with multiple layers

In the preceeding section,the time information was used to calculate the thickness of the stratum corneum. In this section, we will try to extract the refractive index profile for an object with layered structure. To this end, we have designed an experimental configuration as in Figure 4.9, where a plastic petri dish will be used to hold another sample such that their combination forms a two-layer structure. In order to make the results comparable, water and isopropanol were selected as the samples inside the dish.

4.4.1 Refractive index and thickness

In this section, we will first resolve the refractive index and the thickness of the dish. Then the dish's refractive index will be used to characterize the refractive indices of water and isopropanol.

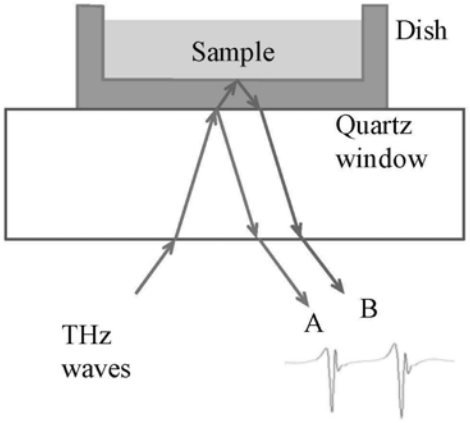

Figure 4.9: Schematic diagram of the layered structure.

The first step is to determine the properties of the bottom layer, namely the dish. To do this, a reference signal was first taken with nothing on the image window (see the top plot in Figure 4.10). Then the empty dish was placed on top of the image window and the corresponding detected signal is plotted as the middle one (titled by dish in Figure 4.10). For clarity, an offset was added to the reference signal. Clearly there are two pulses measured from the dish. It is easy to know that they were created by the top and bottom surfaces of the dish. Since only the first pulse was of interest, a time window was applied to these two signals, as indicated by the dashed rectangle in Figure 4.10. Parts within this window were used as reference and sample signal, respectively. In this way, the refractive index of the dish can be easily obtained, ranging from 1.58 to 1.52 over the evaluated band, as plotted in Figure 4.11. This refractive index was then used in the following step and for the sake of simplicity, 1.55 was used in the calculation. Together with the temporal difference (8.71 ps) of the two pulses from the dish, the thickness of the dish can be calculated to be 872 μm, which is consistent with 881μm measured by a micrometer.

In the second step, water was added into the dish and the a measurement was taken

(see the bottom plot in Figure 4.10). Another time window, indicated by the solid rectangle in Figure 4.10, was applied to it to generate the sample signal. Correspondingly, the second pulse from the dish signal was used as reference this time. In this configuration, the transmitted pulse from the quartz window was thought to be the incident light and dish acted as an image window. Thus the refractive index of the water can be calculated using the theory in Chapter 2. The results are plotted in Figure 4.12a. Meanwhile, results of water using the method introduced in Chapter 2 and the one from TPS are given for comparison.

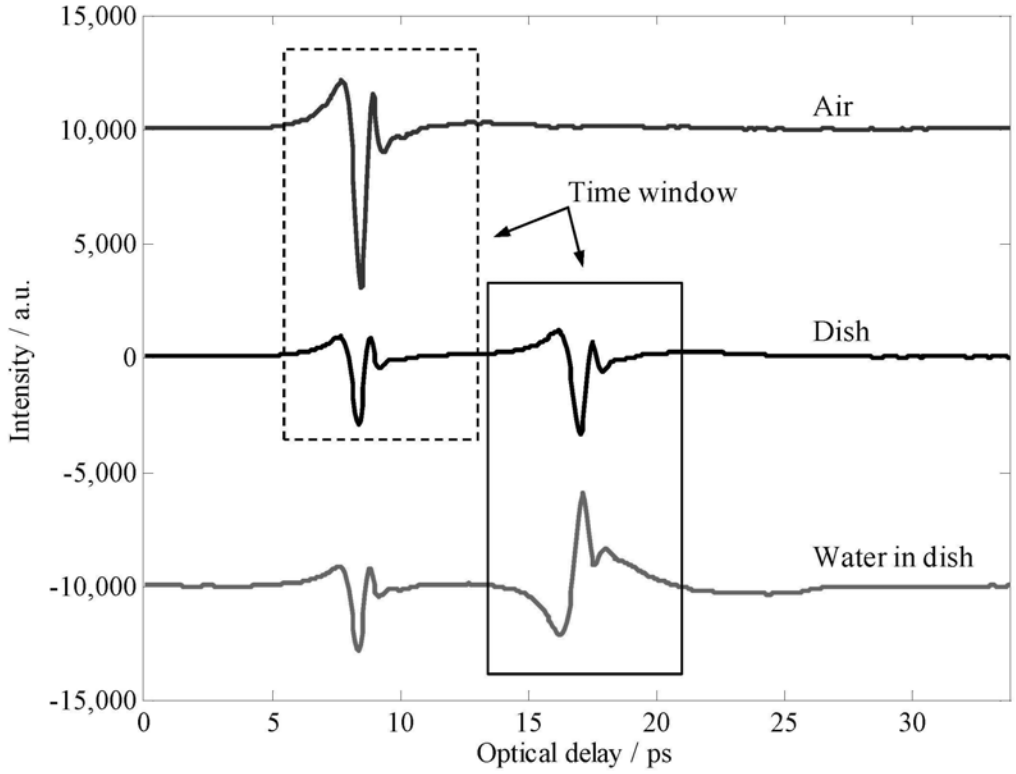

Figure 4.10: Detected temporal waveforms from different measurements.

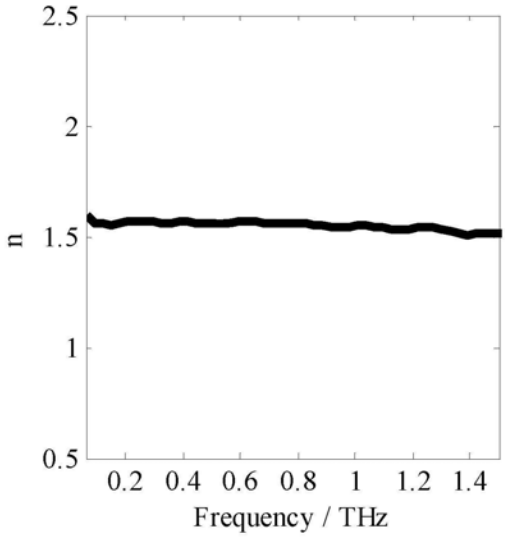

Figure 4.11: Refractive index of the plastic dish.

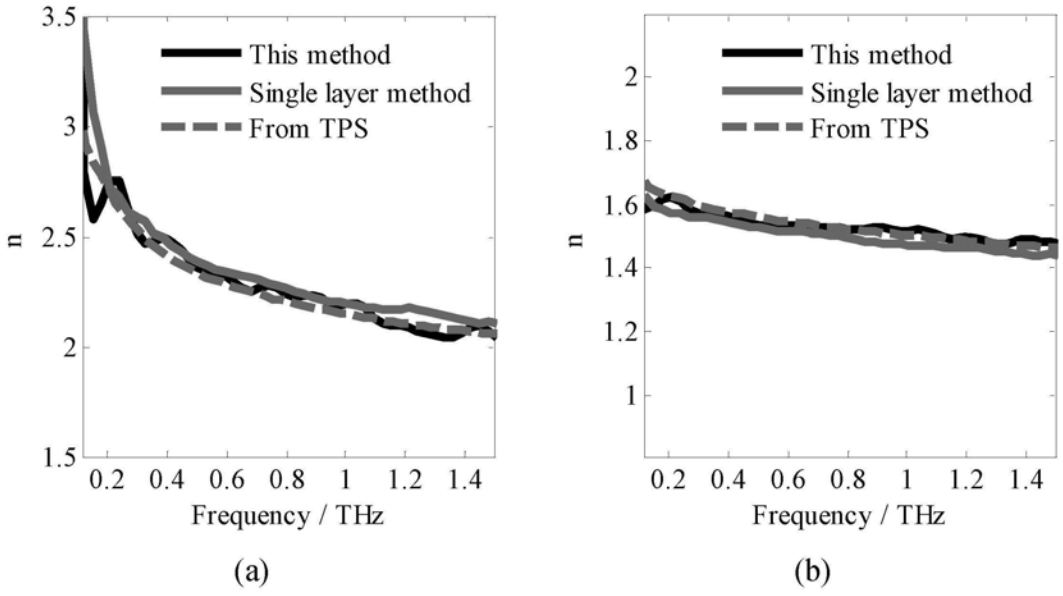

Figure 4.12: Results by different methods for (a) refractive index of water and (b) refractive index of isopropanol.

To further validate this method, we tested isopropanol again and the refractive indices are shown in Figure 4.12b. It can be seen that for both water and isopropanol In Figure 4.12, good agreement can be found with these three different methods.

4.4.2 Absorption coefficient

Meanwhile, the absorption coefficients of each layer were also investigated. Plastic

has been found to be quite transparent to THz waves, which means the absorption in the THz band would be very small and negligible. However, the absorption coefficient from the dish, which we have not shown here, was not as expected. It is mostly likely due to the fact that we used a common petri dish and its surfaces were not flat, which may have introduced some phase errors in the detected signals and consequently it led to the failure of resolving the absorption coefficient.

After water was added in the dish, with the dish acting as the image window we could calculate the absorption coefficient of water. In the calculation, the absorption of dish was neglected. The results from water were given in Figure 4.13. It can be seen that absorption from this method is greater than the that from TPS. We attribute the difference to two reasons. One is that the dish's absorption coefficient was ignored, but in practice it is not zero. The other possible reason would be due to similar artefacts as the baseline artefacts in the quartz-sample configuration in the dish/water configuration. A further study is needed to account these two factors such that the absorption coefficient of the two layers can be well determined with the designed configuration.

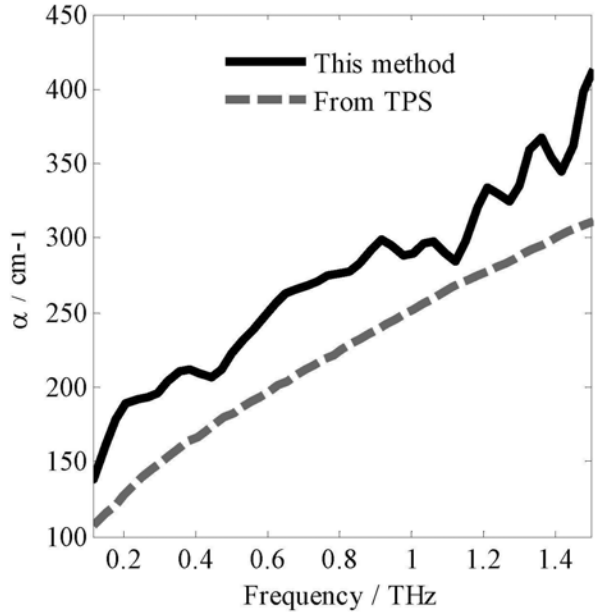

Figure 4.13: Refractive index of the water.

In conclusion, with this experiment we have demonstrated that TPI is able to reveal the inner structure, in not only detecting the thickness profile of the layers, but also

resolving the complex refractive index profile.

4.5 Summary

To summarize, this chapter has investigated the time-of-flight methods and the relationship between the time information, thickness and the refractive index of a sample has been correctly established in our system. It was first implemented to resolve the superficial structure of a palm. The thickness of the stratum corneum was estimated to be the same before and after a plaster layer was added to the palm surface. Through this pilot investigation, we believe TPI can be a promising tool to estimate the burn severity beneath a banding layer. In the second step, we designed an experiment to characterize a two-layered sample. Both the depth profile and the frequency dependant refractive index of the sample were resolved. These results suggest that the time-of-flight technique can be useful to reveal the inner structures in less-absorbing objects.

Chapter 5

Medical applications of terahertz imaging

Having refined the theories and experimental methods in previous chapters, this chapter applies these methods to biological samples. This chapter begins with some background information on THz applications of biological sample of interest. In Section 5.3, a selection of normal tissues excised from laboratory rats are studied. In Section 5.4, TPI is used to further study diseased and normal liver samples. In the data analysis, different parameters such as pulsed amplitude and width in the time domain and refractive index and absorption coefficient in the frequency domain are quantified and compared. In addition, we will also use statistical methods to determine whether the differences of these values are significant.

5.1 Background to THz applications of biological tissues

The entire THz band is found to be severely absorbed by water [88]. This makes water particularly interesting when using terahertz techniques to investigate biological objects as these samples usually have a large fraction of water. It has been shown that there is a significant difference between the responses of THz radiation to cancerous tumors and normal tissues [89]. This property has already been further utilized to create THz images with interesting image contrast that is generally absent in images from current X-ray, NMR, OCT and other medical modalities. Yet the exact reason of this difference is not known. Evidence from PET and MRI studies indicates that tumors have increased water content [90, 91]. Therefore, it is suspected that changes in water content may play an important role. A study by Knobloch *et al*

also suggested that the origin could be partially due to a difference in chemical composition [48]. To explore the full potential of THz imaging and spectroscopy for diagnostic applications, a profound understanding of the origin of the observed difference in the terahertz regime is essential.

Recently there has been an increasing interest of using terahertz to study biological tissues and indeed a number of studies have been reported. However, as can be seen in Table 1.1, the vast majority of the previous investigations relating to biological tissues have been done in transmission geometry. In this geometry, the samples need to be specially prepared, for example by cutting them into very thin slices after lyophilization in a domestic freezer such that THz measurements can be done. Such sample manipulations before measurements sometimes can make the measured optical properties (for example the absorption coefficient) of the tissues quite different from those when they are measured fresh [49]. To keep the tissues unaffected, the best way should be to measure them in living organisms. However, for the time being due to the limited penetration depth of THz radiation in tissues, it is impossible to perform measurements in transmission mode. A more feasible alternative method would be using a THz system in reflection geometry. Indeed such geometry has already been used to study human skin cancers *in vivo* [41]. It can also be applied to other superficial areas such as breast tumor [42]. Similar to the case in transmission mode, *in vivo* investigation of those deeper parts in the body is currently hindered by the penetration limitation. Nevertheless, *ex vivo* measurements can be done in reflection geometry shortly after excision without much preparation. This means that unlike in transmission geometry, the tissue samples can be measured with minimum detriment to samples.

5.2 Methods and protocols

Despite the previously reported work on biological tissues, to date there is still a lack of systematic studies on the experimental protocols and data processing methods. In this thesis we have been aiming to develop a general protocol for using terahertz imaging to study fresh biological tissues. In the protocol we have proposed (as summarized the flow chart in Figure 5.1), the whole process can be generally divided into four steps: sample preparation, sample measurement, data selection and data

analysis. In the following subsections, more details of these steps will be discussed with an example when we measured tissues from different rat organs.

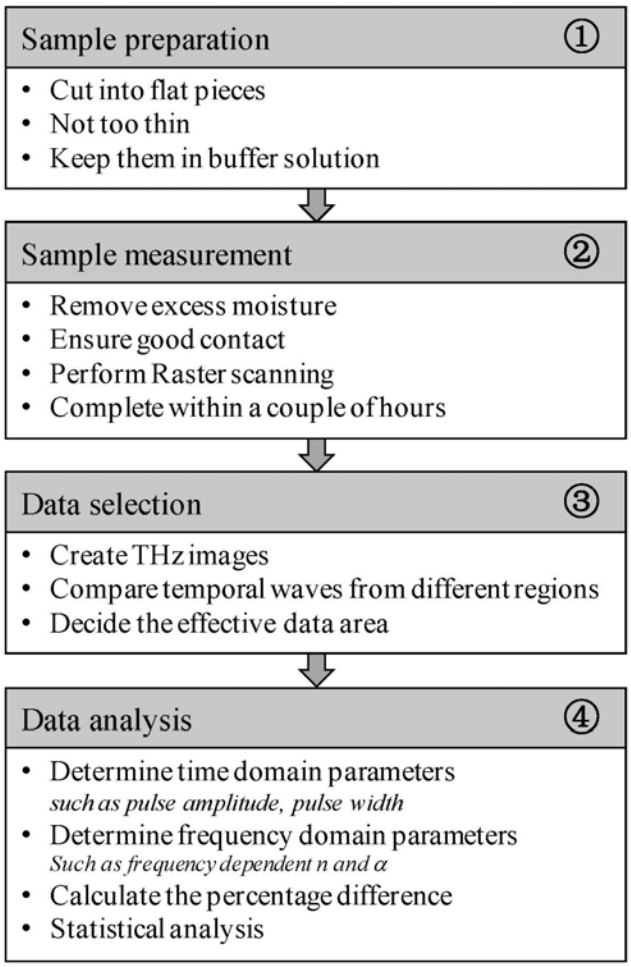

Figure 5.1: A general protocol for studying biological tissues with THz imaging.

5.2.1 Sample preparation

Laboratory rats share a high degree of homology with humans. In addition to their calmness and ease of handling, they can be inexpensively and easily maintained in laboratories. Therefore, they are commonly used for a variety of medical research purposes. Indeed, other animal tissues like chicken, pork, and beef as well as human tissues from autopsy have been prepared for THz experiments (as cited in table 1.1). In this chapter, all the tissue samples we used were from laboratory rats. Nine-month-old female Sprague–Dawley rats were used in this study. The

experimental protocol was approved by the institutional Animal Experiment Ethics Committee. The rats were bred at the Laboratory Animal Services Centre of the Department of Diagnostic Radiology and Organ Imaging. They were housed at 22°C under a 12-hour light, 12-hour dark cycle while receiving a standard commercial rat chow (Prolab RMH 2500, PMI Nutrition International LLC, Brentwood, USA) and water diet *ad libitum*. For specimen sampling, they were killed with over-dose of pentobarbital. When we used THz to study healthy tissues, to obtain meaningful comparisons, ten rats were measured on five successive days.

All the organ samples we studied were prepared by Department of Diagnostic Radiology and Organ Imaging and kept in Krebs-Henseleit solution (KHS) to prevent rapid deterioration and maintain their natural hydration levels. Then they were taken to our lab and sliced using a scalpel blade. Special attention was paid to ensure the samples were sliced into flat sections such that they could make good contact with the quartz platform in the measurements. To avoid later reflections after the quartz/sample, the typical slice thickness was several millimeters.

5.2.2 Sample measurements

For each organ sample, two different slices were selected for measurements. Before a section was put on the image window for data collection, it was first placed on a paper tissue and trundled until no obvious KHS drops could be observed on its surface. This was important because the results in areas with KHS drops could be dominated by the solution rather than the tissue itself. Then the samples were carefully placed on top of the image window. As the thin tissue sections had been kept in the solution before, in most cases, they were soft and thus could naturally make good contact with the window. Sometimes the samples were not flatly cut and it was recommended to press the sections gently for example by a pair of tweezers before they were measured. All the measurements in our study were performed by the reflection system (TPI imaga 1000, illustrated in Figure 2.1). When a section was ready for measurement, raster scanning of the sample in the x-y plane could be conducted for data acquisition. The scanned area could vary with the tissue size and its position on the window. In the measurements of healthy organs, for each sample an area of 10 mm by 10 mm was imaged, with 75 and 80 steps in the x and y axes

respectively. Thus a total of 6000 pixels were obtained in an image. For each pixel, a point measurement, analogous to an ultrasound A scan, contained 512 data points over 47 ps, as plotted in Figure 5.2d. The raw sample data represent the impulse function of the sample convolved with the reference data. So that the sample impulse function could be extracted at each pixel, a reference image of air was taken with the same imaging parameters as each sample image. The whole process was finished within a couple of hours of excision.

5.2.3 Data selection

The sample impulse functions were then obtained by performing deconvolution as detailed in Chapter 2 as well as in our previous work [40, 92]. For brevity, the impulse functions will subsequently be referred to as waveforms. THz images were constructed by plotting, for example, the waveform maximal or minimal values at each pixel (E_{max}, E_{min}, as illustrated in Figure 5.2f) and using a false color scheme to represent the pulse intensity (An example image of a heart sample is given in Figure 5.2d, where E_{max} is plotted). These images were useful for data selection.

For the fresh organs, it was difficult to make sure all the sections were absolutely flat. This meant that despite our careful preparation, some areas did not make perfect contact with the quartz window (for instance in a heart sample, air gap could be created by the heart chamber part, see Figure 5.2b and c). Signals from such areas are easy to identify as the reflected waveform is very different – illustrated by the dashed line in Figure 5.2e. These waveforms were not included in the tissue characterization calculations. Similarly, areas that were not effectively covered by samples could be determined and waveforms from these regions should also be excluded. Additionally, as can be seen in Figure 5.2d, there are some edge zones in the image, for example areas in the vicinity of the boundary lines of the air gap (corresponds to the central part in the image) and the outside boundary of the sample. Waveforms from these areas were usually not reliable and thus should be avoided. Consequently, only data from inside the black line in Figure 5.2d were thought to be effective. Typically there were about ten thousand pixels of data for each organ type.

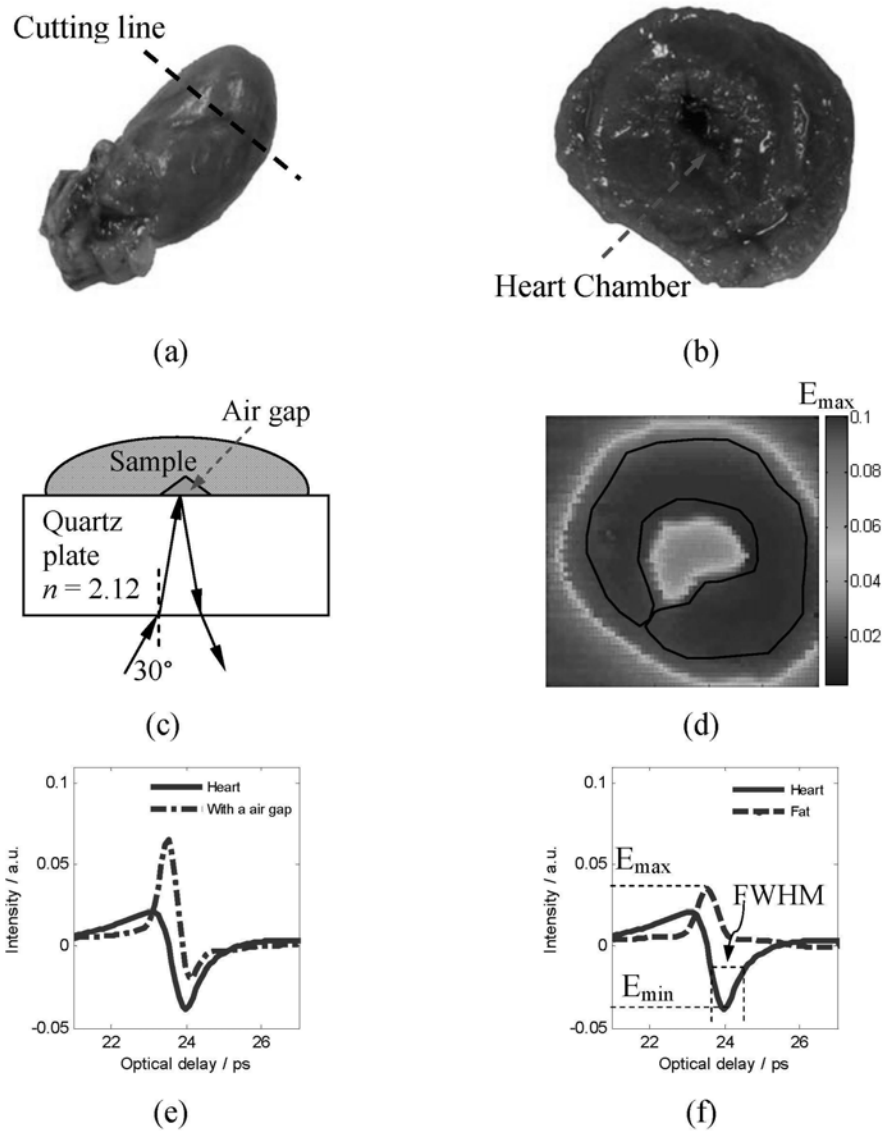

Figure 5.2: Diagram showing the experimental protocols. (a) Photograph of a heart sample with the dashed line indicating the how it was sliced. (b) Optical image of the sliced heart sample. (c) Measurement geometry in this study showing the air gap (indicated by the yellow triangle) due to bad contact of the heart chamber and the quartz window. (d) THz image of the heart sample (E_{max} is plotted). Data from the area of interest (indicated by the black path) are used for analysis. (e) Waveform from the heart with perfect contact (solid line) and a waveform from a point with bad contact (dash-dotted line, with a greater peak before the trough). The reference signal, a 512 data set over 47 ps. (f) Typical time domain waveforms, from the heart (solid line) and abdominal fat (dashed line). E_{max} and E_{min} are the maximal and minimal values of the intensities. FWHM stands for the full width at half maximum (or minimum).

5.2.4 Data analysis

As we have outlined in Chapter 2, from the acquired THz raw data many parameters can be obtained for analysis. Among the time domain parameters, the pulse

amplitude and the full width at half maximum (FWHM) are thought to be highly related to the refractive index and absorption coefficient [61]. Therefore, both of them were used for time domain analysis. Then in the frequency domain, we mainly focused on the frequency-dependent refractive index and absorption coefficient. For each parameter, the mean values, standard deviations and the 95% confidence intervals were calculated. Then percentage differences in these parameters were quantified. Finally, two sample *t*-tests were used to assess the statistical significance.

5.3 Healthy tissues

Based on the methods and protocols discussed above, we investigated several types of healthy organ tissues, including liver, kidney, heart muscle, leg muscle, pancreas and abdominal fat tissues. The main purpose of this work is to determine the ability of TPI to differentiate between freshly harvested tissue types in reflection geometry. Also, through this full scale investigation, we hope the methods and protocols we proposed can be validated and standardized to facilitate THz imaging of biological tissues.

5.3.1 Results

In this section, first we will show the time domain waveforms measured from the six different types of tissue. Then results for their frequency dependent dielectric properties will be presented, including their refractive index, n and absorption coefficient, α.

Time domain waveforms

Figure 5.3 illustrates the time domain waveforms reflected off the top surface of the quartz plate, namely the interface between the tissue and plate. Due to differences between the tissue types, pulse shapes of these reflections are quite different from each other.

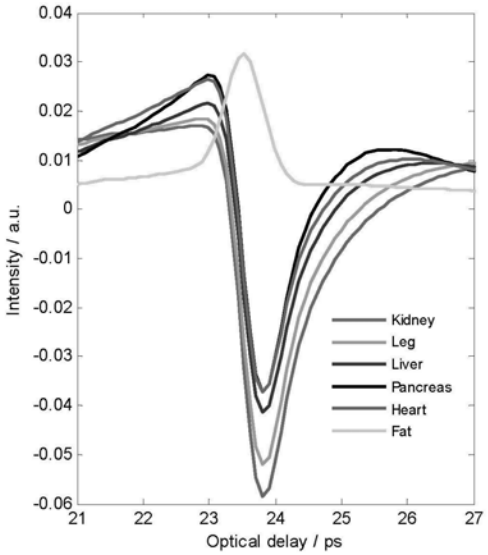

Figure 5.3: Time domain waveforms of the tissues measured.

Table 5.1: Amplitude and FWHM of the main reflection off the tissues, with the amplitude in descending order. Mean stands for the mean value obtained from data from all the ten rats for a particular organ and STD stands for the corresponding standard deviation.

	Amplitude (a.u.)		FWHM (ps)	
	Mean	(STD)	Mean	(STD)
Kidney	-0.0584	(0.0021)	0.7508	(0.0382)
Leg	-0.0520	(0.0055)	0.7185	(0.0408)
Liver	-0.0413	(0.0048)	0.6431	(0.0597)
Pancreas	-0.0372	(0.0037)	0.5455	(0.0697)
Heart	-0.0372	(0.0049)	0.5879	(0.0724)
Abdominal Fat	0.0329[a]	(0.0080)	0.8274	(0.3781)

[a] E_{max} was used for abdominal fat, and E_{min} for the other tissues.

Table 5.1 summarizes the mean and standard deviation of the pulse amplitude and FWHM, with the amplitude value in descending order. In terms of the reflected amplitude, the pancreas and heart are very similar to each other. However, their FWHM are quite different. Two sample t-tests were used to determine if differences

in mean amplitude and FWHM were statistically significant ($p<0.05$) among all these tissues. Results show that except for the amplitude between the pancreas and heart, significant differences among the tissues can be seen in both the amplitude and FWHM.

When light is reflected off a more dense medium, a 180° phase change will occur. As can been seen in Figure 5.3, compared to abdominal fat, waveforms reflected off the other 5 tissues all have a 180° phase change. Using this phase change information, we can deduce that n of abdominal fat is less than that of the quartz plate (n_{quartz} is 2.12), while n of the other tissues are generally greater than 2.12 over the bandwidth measured. This is in agreement with their calculated values shown in Figure 5.4b.

Frequency dependent n and α

Using the theory previously given in Chapter 2, the frequency dependent refractive index, n and the absorption coefficient, α of the tissues were calculated. Graphs of n and α are shown in Figure 5.4. All the results are the mean values of the ten rats and error bars represent the 95% confidence intervals. Due to bandwidth limitations and attenuation at higher frequencies, the effective frequency range for analysis in this study is 0.2-1.4 THz. In all the measurements the frequency resolution is about 0.021 THz. To make the plots clear after adding the error bars and for a better presentation in the statistical analysis, we select the data points with a step length of 0.1 THz.

From the plots of α in Figure 5.4a, differences between all the tissues can be seen and are consistent over most of the frequency range. Figure 5.4b illustrates the results of the n for all organ types. Some differences in n are subtle and some lines intersect each other (this will be further discussed in the following section). However, some samples are clearly different and to highlight this we plot them separately in Figure 5.5.

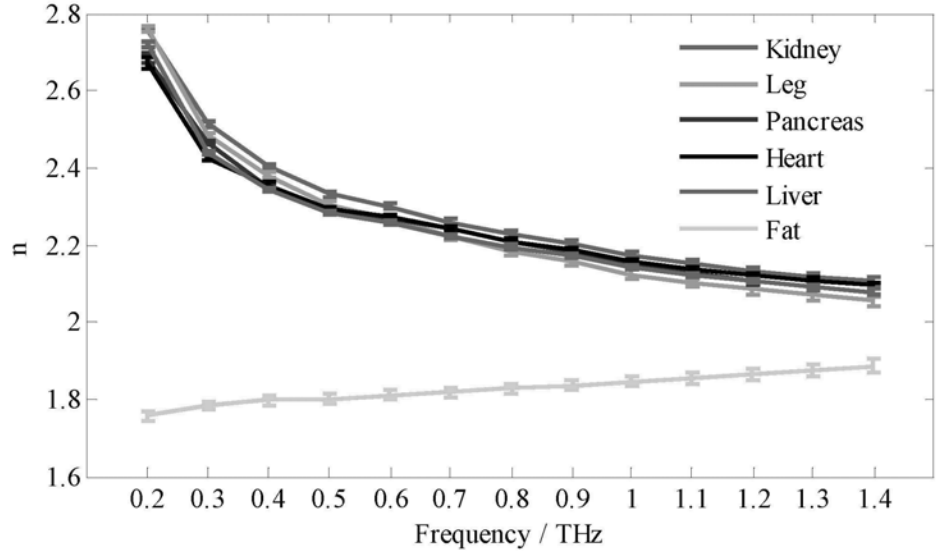

(a)

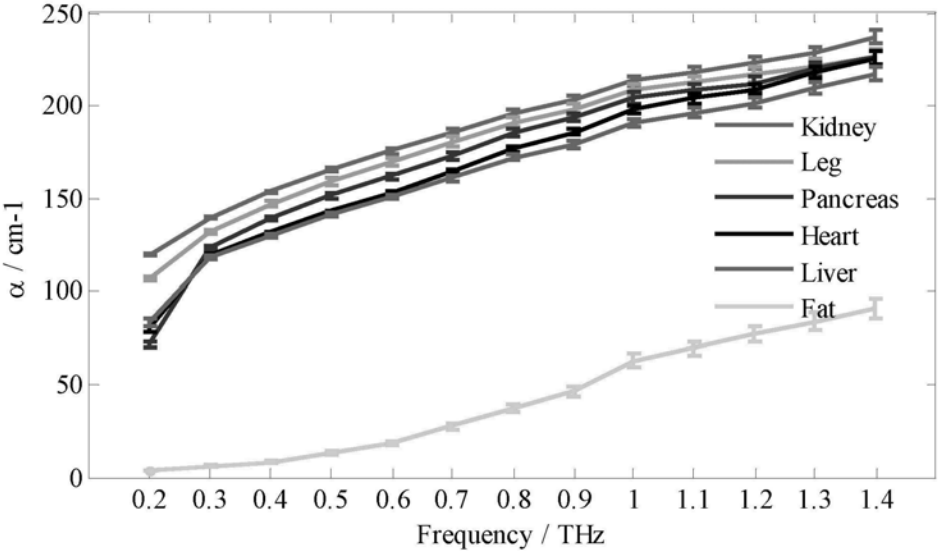

(b)

Figure 5.4: (a) Mean absorption coefficients of all the tissue samples. (b) Mean refractive indices of all the tissue samples. Error bars represent 95% confidence intervals.

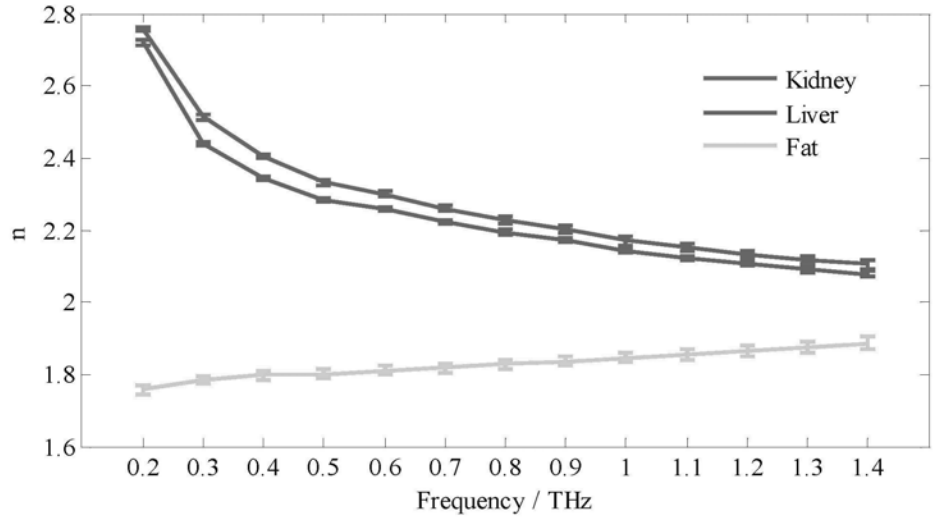

(a)

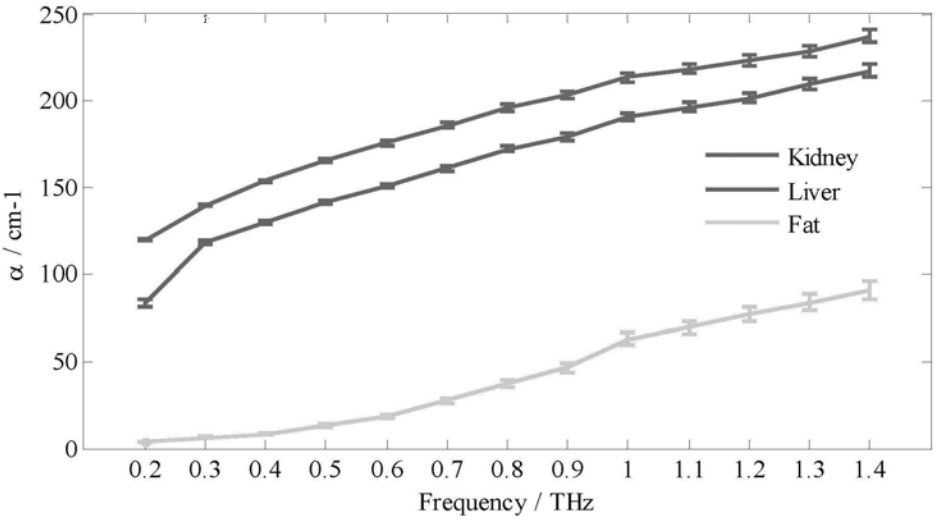

(b)

Figure 5.5: (a) Mean absorption coefficients of kidney, liver and abdominal fat. (b) Mean refractive indices of all the tissue samples. Error bars represent 95% confidence intervals.

We compare our results to those measured in transmission by Png *et al* [49]. Png *et al* also measured fresh samples of rat liver and kidney. However, their samples were nitrogen-dried or lyophilized in order to obtain data above the noise floor of their system. These processes significantly reduced the absorption of the sample and thus we see clear differences between our data and theirs. For instance, we measured the absorption coefficient of fresh liver at 1 THz to be 180 cm^{-1}, whereas their corresponding measurements were 45 cm^{-1} for the nitrogen-dried sample and 35 cm^{-1}

for the lyophilized sample. For some samples, the duration of nitrogen drying was of the order of several days (as the process was continued until no improvement in the THz signal was observed). Their reported absorption coefficient measurement of liver (175 cm^{-1} at 1 THz) after two and a half hours of nitrogen drying is in close agreement with ours of fresh liver (180 cm^{-1}): this was the point at which their sample measurement first came above the noise floor and is before the nitrogen drying had dramatically reduced the absorption coefficient.

Statistical analysis of n and α

By plotting α and n against frequency, a rough indication of the differences between the measured tissues has been provided. In this section, we will further present those quantitative values and test the results using statistical methods.

Using the absorption coefficient data plotted in Figure 5.4a, we now sort these tissues with α in descending order namely: kidney, leg muscle, pancreas, heart muscle, liver and abdominal fat. To make a thorough comparison of the differences between the six tissue types, they are divided into five pairs, each pair consisting of two different tissues. The difference for a given pair is calculated as the relative difference in percentage, for example, in the pair with kidney and leg muscle, their difference in α would be defined as $(\alpha_{kidney} - \alpha_{leg})/\alpha_{leg} \times 100$ and is denoted by K-M in the table. Therefore, when we compare the samples in descending order in this way, we expect the sign of the percentage difference to always be positive if the differences are consistent across the whole frequency range.

Table 5.2 gives the percentage difference of α over the selected frequencies as mentioned earlier. As can been seen, nearly all the decimals are positive except the two in the second row (0.2 THz). This means that for all the five pairs, the absorption of the first tissue is consistently greater than that of the second over frequencies above 0.2 THz. We observed that the percentage differences between the first four pairs are small, usually within a few percentage points. Therefore to determine whether the differences were significant we conducted a two sample t-test at each frequency point as in the time domain. The t-tests found that there were statistically significant differences for all the combinations in Table 5.2 apart from eight elements (marked with an asterisk). Significant differences can still be observed in the H-L

pair, despite the small percentage differences because significance is not merely dependent on the magnitude of the relative differences but also on the standard deviation. The high values in the last row (liver and abdominal fat) indicate the large differences between the tissue properties which are also evident from Figure 5.4a.

Table 5.2: Estimated percentage difference of α (e.g., for group K-M, it is calculated as ($\alpha_{kidney} - \alpha_{leg}$)/$\alpha_{leg}$×100) over the selected frequencies. The capitals K, M, P, H, L, and F stand for kidney, leg muscle, pancreas, heart muscle, liver, and abdominal fat respectively.

Group	Frequency (THz)												
	0.2	0.3	0.4	0.5	0.6	0.7	0.8	0.9	1.0	1.1	1.2	1.3	1.4
K-M	11.89	5.88	4.70	4.12	3.34	2.84	2.45	2.51	2.31	2.86	3.03	3.34	4.89
M-P	48.94	6.73	5.30	5.15	4.92	4.42	3.20	2.29	2.04*	1.68*	2.29*	0.78*	0.02*
P-H	-10.61	3.32	5.77	5.84	5.86	5.39	4.85	4.33	3.20	2.36	1.59*	0.87*	0.14*
H-L	-4.22	1.26	1.26	1.37	1.28	1.99	2.71	3.62	3.92	3.96	3.57	4.02	3.82
L-F	2153	1788	1509	1006	731	484	362	286	204	182	161	150	139

Therefore, for the majority of the samples consistent relative percentage differences in α can be seen between the tissues over the tested terahertz band from 0.2-1.4 THz.

Table 5.3: Estimated percentage difference of n (e.g., for group K-M, it is calculated as ($n_{kidney} - n_{leg}$)/n_{leg}×100) over the selected frequencies. The capitals K, M, P, H, L, and F stand for kidney, leg muscle, pancreas, heart muscle, liver, and abdominal fat respectively.

Group	Frequency (THz)												
	0.2	0.3	0.4	0.5	0.6	0.7	0.8	0.9	1.0	1.1	1.2	1.3	1.4
K-M	-0.21	1.21	0.99	1.29	1.33	1.58	1.89	2.00	2.19	2.30	2.32	2.32	2.41
M-P	2.94	0.68	1.29	0.82	-0.09	-0.78	-1.07	-1.15	-1.10	-1.04	-0.99	-1.14	-1.05
P-H	0.45	1.67	-0.15	-0.34	-0.19	-0.04	-0.08	-0.17	-0.40	-0.47	-0.68	-0.69	-0.88
H-L	-1.82	-0.51	0.39	0.38	0.68	0.81	0.67	0.68	0.59	0.59	0.65	0.83	0.85
L-F	54.84	36.59	30.52	26.82	24.80	22.37	20.05	18.36	16.08	14.43	12.94	11.49	10.10

Table 5.4: Testing results of n over the selected frequencies. A '√' indicates a significant difference between the mean refractive index ($p<0.05$) and a '×' indicates a non-significant difference ($p<0.05$). The capitals K, M, P, H, L, and F stand for kidney, leg muscle, pancreas, heart muscle, liver, and abdominal fat respectively.

Group	Frequency (THz)												
	0.2	0.3	0.4	0.5	0.6	0.7	0.8	0.9	1.0	1.1	1.2	1.3	1.4
K-M	×	√	√	√	√	√	√	√	√	√	√	√	√
M-P	√	√	√	√	×	√	√	√	√	√	√	√	√
P-H	×	√	×	×	×	×	×	×	×	√	√	√	√
H-L	√	√	√	√	√	√	√	√	√	√	√	√	√
L-F	√	√	√	√	√	√	√	√	√	√	√	√	√

Similarly, analysis of n was performed. Table 5.3 shows the percentage differences of n for the tissues and Table 5.4 illustrates the corresponding results of the two sample t-tests. A tick in Table 5.4 represents that the difference is significant while a cross would indicate a non-significant difference. Unlike Table 5.2 (in which the signs were nearly all positive), the signs in Table 5.3 are more complicated. However, from the percentage values and testing results of K-M and L-F pairs, we can conclude that the differences for these two pairs are consistent over the frequency range above 0.2 THz. According to our previous discussion on the sign of the values, the change of the signs in the middle three pairs in table 3 indicates that the refractive index values are crossing each other. From this point of view, differences in refractive index for the M-P, P-H and H-L pairs are not as consistent as those in absorption. However, for certain frequencies we can find statistically significant differences between all five pairs, namely at 0.3 THz and 1.1 to 1.4 THz.

5.3.2 Discussions

Until now little work has been done to thoroughly explain the origin of differences in refractive index and absorption coefficient. Here we try to understand the different absorption coefficients of organs by their water contents. Fatty tissues consist of a wide group of compounds that are largely insoluble in water. Generally, the water content in a fat tissue is less than 30% [93], which is much less than those in other

organ tissues such as liver, heart, pancreas, muscle and kidney. This is consistent with our findings in that among the investigated tissues, absorption coefficients from abdominal fat tissues are the smallest. In Table 5.2 we see that values of percentage differences for the first 4 pairs are actually very small, generally less than 6% except for a couple of cases. It means that the frequency dependent absorption coefficient profiles of the two tissues in each pair are very close, which may also indicate similar water content in the tissues. Indeed there have been several studies of the water content in the abovementioned organs. However, due to the difference in water content definitions and evaluation methods as well as the testing objects, it is very difficult to find out an exact relation between their water contents for these different organs. Peters *et al* studied the organ weights and water levels of rat with various daily restrictions of food intake [94]. In their work 14 different organ tissues were investigated, including heart, kidney, liver and muscle from abdominal wall. From their data as shown in Figure 5.8, they found that the water levels of kidney, heart and liver in descending order, which is similar to the relationship of the absorption coefficient for these three organs in our results. The water level of muscle from abdominal wall was reported to be between those from heart and liver, and this relationship was in agreement with the findings in a work by Shirley *et al* [95], where heart, gracilis muscle and liver samples from cattle. Whereas in our calculations, the plot (in Figure 5.4) of absorption coefficient of leg muscle were found to be sitting in between those of kidney and liver. One possible reason could be that the muscle tissues in our study and theirs were excised from different parts. We have not been able to find appropriate data of the pancreas to make such comparisons. The above discussions have been made from the view of water content. Indeed, it has been suggested that differences in chemical compositions may also result in alterations of optical properties and this can be an indication for further work to understand the origin of those differences.

The typical thickness of the sliced tissues was a couple of centimeters. This helped avoid later reflections after the quartz/tissue interface as the signal was attenuated sufficiently. It should be noted that in the calculation of the complex refractive index, the thin tissue sections were assumed to be homogeneous with depth such that the theory in Section 2.3.2 can be used. In the sample preparation, all the sliced tissues

were carefully selected to ensure the homogeneousness of the measured parts. Further considerations of the variability with depth would need to be made for inhomogeneous tissue samples.

5.3.3 Conclusion

In this part, we measured the terahertz properties of freshly harvested healthy rat organ samples in reflection geometry. For the time domain reflection pulses, the amplitude and FWHM values were significantly different for all organs measured apart from the amplitudes of pancreas and heart samples.

TABLE 2

Weights and water levels of organs in the summer control group fed ad libitum

Organ or tissue	Weight [1]	Water level [2]
	%	%
Adrenal glands	0.0263 ± 0.0021 [3]	71.73 ± 1.51
Brain	0.926 ± 0.066	78.18 ± 0.23
Gastrointestinal tract		
Cardiac stomach	0.132 ± 0.012	76.34 ± 0.39
Pyloric stomach	0.390 ± 0.034	76.57 ± 0.53
Small bowel	0.990 ± 0.082	79.94 ± 1.03
Cecum	0.323 ± 0.041	78.79 ± 0.81
Colon	0.536 ± 0.044	79.30 ± 0.51
Heart	0.345 ± 0.013	77.09 ± 0.50
Kidneys	0.777 ± 0.052	77.41 ± 0.21
Liver	4.281 ± 0.364	71.09 ± 0.61
Lungs	0.655 ± 0.182	78.92 ± 0.55
Muscle (abdom. wall)	1.311 ± 0.214	74.56 ± 1.09
Ovaries	0.0285 ± 0.0046	78.04 ± 0.77
Skin	19.99 ± 1.01	64.27 ± 2.04
Spleen	0.359 ± 0.080	76.53 ± 0.32
Submaxillary glands	0.136 ± 0.013	75.10 ± 0.76
Thymus gland	0.0914 ± 0.0141	78.12 ± 1.03
Residual carcass	53.34 ± 1.46	66.99 ± 1.34

[1] Measured as % of autopsy body weight.
[2] Measured as % wet weight.
[3] Mean ± SD.

Figure 5.6: Weights and water levels of organs in the summer control group fed *ad libitum*. Water levels in heart, kidneys, liver, muscle were used for understanding the differences observed in THz region in our discussion (Cited from Peters' work [94]).

In the frequency domain we found that the percentage differences in n and α were small, but mostly statistically significant. Interestingly, differences in α were larger and more consistent over the frequency range than those in n. This suggests that the strong attenuation of tissue samples can be used advantageously to enhance image contrast.

In conclusion, with our reflection system it is possible to characterize the tissues in

both time and frequency domains. The statistically significant differences found using TPI enable us to differentiate between all the tissue types investigated. These early results are useful for the development of clinical protocols and for advancing the understanding of contrast mechanisms in biological terahertz imaging.

5.4 Healthy and diseased tissues

5.4.1 Introduction

Terahertz spectroscopy has already been demonstrated to be promising in characterizing different chemical components [96-98]. Apart from structural deformations, chemical changes in biological objects can also be caused by illnesses. If terahertz imaging can be effectively used to characterize such changes, it would be of great benefit to clinicians. Having used TPI to study different healthy tissues, in this section, we will continue to explore the potential of TPI in distinguishing between healthy and diseased liver tissues.

Hepatocellular carcinoma (HCC) is the fifth most common cancer worldwide and its incidence is increasing and will likely to continue for decades[99]. It is found that about 80% patients with HCC have cirrhosis [100]. Resection of HCC has become a safe operation with very low operative mortality as a result of advances in surgical techniques. However, the 1-year, 3-year and 5-year probabilities of HCC recurrence after resection were reported to be 19%, 54% and 70%, respectively [101]. Known risk factors for recurrence include cirrhosis of the liver, chronic active hepatitis, hepatitis C virus infection, high number of nodules affected, vascular invasion and disrupted tumor capsule. Compared with non-cirrhotic cases, resections in cirrhotic livers can be technically more challenging. Of more concern is the problem of reliably estimating the functional capacity of a cirrhotic liver and its propensity to develop new malignant lesions [102]. Hepatic cirrhosis is a serious condition due to chronic liver disease. In the development of cirrhosis, as the liver cells become damaged and die, scar tissues will gradually develop. This irreversible fibrosis of the parenchyma will cause the liver to lose its ability to function well. An earlier paper has reported differences in dielectric parameters between the normal and cirrhotic

areas in the microwave region [103]. This indicates that the formation of new structures in the liver during the cirrhosis process may lead to changes of the dielectric properties.

5.4.2 Samples and experimental probe system

Normal and cirrhotic liver samples from Sprague–Dawley rats were taken and studied *ex vivo*. In both the normal and diseased groups, the same protocol as discussed in section 5.2.1 was used for sample preparation.

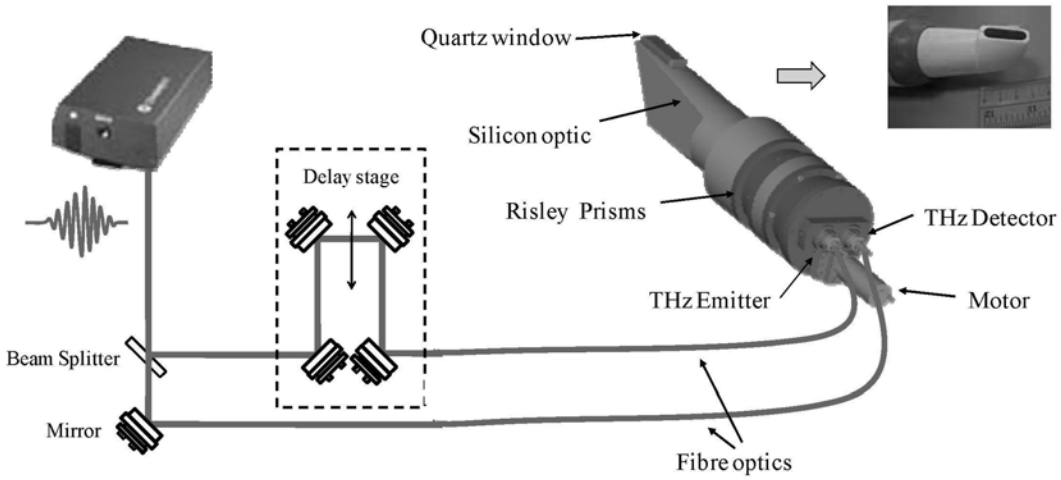

Figure 5.7: Schematic diagram of the hand-held probe system. The THz emitter, detector and the motor have been integrated into the probe.

TeraView Ltd. (Cambridge, UK) has recently developed a handheld THz probe system, which is based on the previously described flatbed platform (TPI Imaga 1000, see figure 2.1) with a mobile probe connected to it by fiber optics cables. The probe allows easier access to objects that cannot easily be placed on the imaging platform. A schematic diagram of the structure of this probe system is given in Figure 5.7. It employs the same TI:Sapphire laser as in our previous system (TPI Imaga 1000). Using optical fibers inside the electric cable, the ultrafast femtosecond pulses from the laser are guided down to the probe, where photoconductive antennas are integrated for both THz emission and detection. The emitted THz beam is focused to the probe tip (a 1cm by 1.5cm z-cut quartz plate), where samples can be measured. In this measurement, the probe was fixed such that sections of liver

tissues can be measured on top of the quartz plate (as illustrated by the inset photograph in Figure 5.7). Temporal waveforms were obtained from multiple line scans.

For each group, several different slices were selected and measured separately. The first measurements were taken of the freshly harvested liver tissues. Then, the samples were fixed for 24 hours in 10% formalin solution and measured again. The frequency dependent complex refractive indices were calculated. The detailed theory can be found in Chapter 2 as well as in our earlier paper [104].

5.4.3 Results

Figure 5.8 shows the refractive index, n and absorption, α of the cirrhotic and normal groups, indicated by the bold and thin lines respectively. The solid and dashed lines represent results of the fresh samples and those after formalin fixation. For the fresh tissues, both n and α from the cirrhotic group are greater than that of the control group. We attribute the increased absorption coefficient in the cirrhotic samples to a difference in water content between normal liver and cirrhotic liver [105]. This increase is also in agreement with the findings in microwave region [103]. After fixing in formalin, the tissues in the two groups have lower water content than before. This is why we see a decrease in their n and α. However, there is still a clear difference between the normal and cirrhotic samples. Since the water levels in these two kinds of tissues are expected to be similar after fixation, this slighter difference may be due to the differences in the tissue structure and composition.

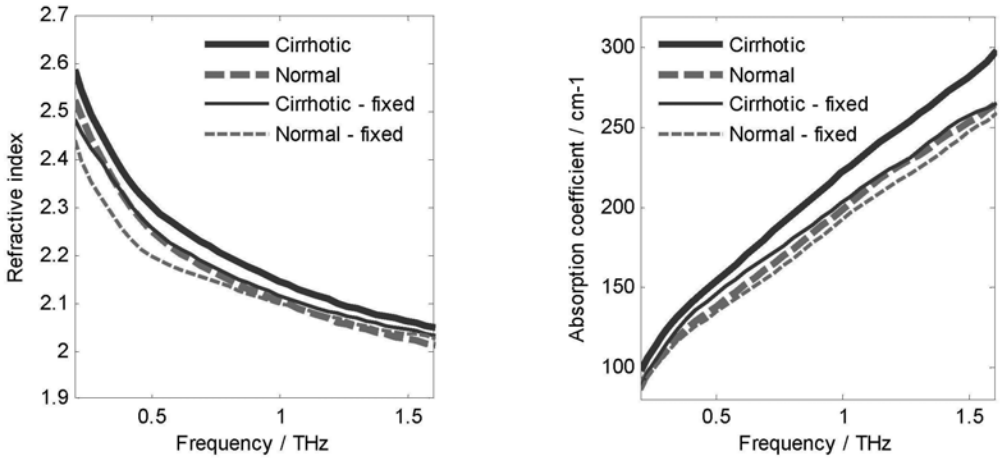

Figure 5.8: (a) Refractive indices and (b) absorption coefficients of the liver tissues.

To further understand the origin of the observed differences in the dielectric properties, the samples were examined histologically using Hematoxylin and eosin staining. From microscopy pictures (see Figure 5.9, original magnification: ×100), severe fibrotic changes were found in the cirrhotic liver, this may have also contributed to the greater absorption coefficient since fibrous tissue is highly absorbent of terahertz radiation.

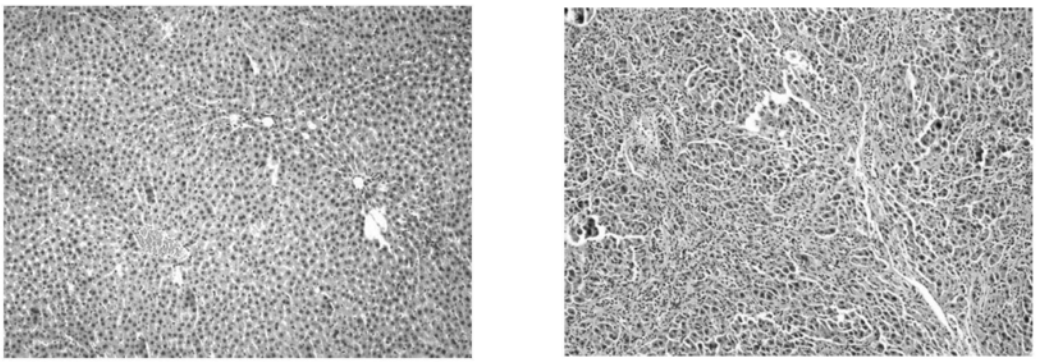

(a) (b)

Figure 5.9: Microscopy pictures (×100) of samples from (a) normal liver and (b) liver with cirrhosis

5.4.4 Conclusion

In conclusion, we have calculated the *ex vivo* frequency dependent refractive index and absorption coefficient of normal and cirrhotic liver tissues. To the best of our knowledge, this is the first study to characterize rat liver cirrhosis in the terahertz region. Higher refractive index and absorption coefficient were found in the liver of cirrhosis in comparison with the control group. This relationship could still be seen after fixation in formalin despite some decrease in the values. These preliminary results suggest that TPI can differentiate liver with cirrhosis from normal liver not only by the water content but also by the inner structure and composition. Further work needs to be done to more precisely relate the observed differences in the terahertz band with histological findings.

5.5 Summary

We have applied terahertz pulsed imaging for *ex vivo* studies of fresh biological

tissues. We first investigated six types of rat tissues, all of which were excised from healthy rat organs. Different parameters in the time domain and frequency domain were calculated. Using these results we were able to quantitatively characterize the tissue differences and distinguish between them. From statistical analysis of a large pool of data, we saw those differences were significant. Based on the tissue water content reported by other authors, we tried to understand the origin of the observed differences. In the second experiment, both healthy and diseased liver tissues were studied by a probe system. Differences in the optical parameters were observed between the normal and cirrhotic liver tissues. In this chapter, methods and protocols for fresh tissue measurements have also been studied.

Chapter 6

Conclusions and future work

6.1 Conclusions

The aim of this work was to refine the existing techniques and develop new terahertz methods such that terahertz imaging can be reliably used for biomedical applications, particularly for the purpose of tissue characterization. By focusing on the reflection configuration in our imaging system, a number of key issues concerning the system accuracy were addressed.

6.1.1 Angle of incidence

Due to the non-normal angle of incidence of the THz beam in a reflection system, it is more cumbersome to extract the optical parameters. In our imaging system, this angle is 30 and before this study it was neglected in our data analysis. In chapter 2, we refined the algorithms and incorporated the angle of incidence such that both the frequency dependent refractive index and absorption can be simultaneously resolved in an analytical way. Our solution did not need to calculate the phase angles or involving any iteration steps. Hence it could be easily implemented, for example, for real time imaging. This algorithm was tested by measurements of water and air. The resulting complex refractive index was compared with that from a spectroscopy machine. The good agreement proved the validity of the new algorithm. Meanwhile, we also calculated the refractive index and absorption coefficient using the old algorithm which failed to account the angle of incidence. By comparing the calculated refractive indices from these two different algorithms, we found that the angle of incidence had a larger impact on materials with lower refractive index.

6.1.2 SNR sensitivity

In Chapter 3, the system performance was evaluated in terms of the signal to noise

ratio and dynamic range. Both of SNR and DR decreased as the frequency increased, which meant that the signal quality was deteriorating at the higher frequencies. Through simulation work, we found that both the refractive index and absorption coefficient were similarly affected by noise. We further developed a method to quantitatively evaluate the accuracy from the DR values of the sample signal.

6.1.3 Position variability

From the raw data collected by a raster scanning, we found a significant variation in the amplitudes over the locations in the x-y plane. Based on the similar trends observed in the sample, reference and baseline signals, we developed a new data acquisition protocol, in which reference and baseline were imaged with the same parameters as in a sample measurement. Hence, all the sample, reference and baseline signals could be spatially aligned in the new data processing algorithm. Consequently, the intensity variation was successfully reduced by a factor of three.

6.1.4 Ringing artefacts

Typical reflection systems with an image window usually suffer from ringing artefacts due to the lower surface of the window. In our system it was previously addressed by measuring an additional quartz plate on top of sample window. This method was very dependent on the cleanness status of the plate and the cleaning process was usually tedious. Using optical parameters of water and air, we were able to determine the ringing effects and then account for them in subsequent calculations. Improved accuracy provided further validation of our theories and methods.

6.1.5 Time-of-flight formula

In Chapter 4, we studied the time-of-flight technique. In samples with distinctive layers, layer thicknesses had be converted from temporal differences between different reflected pulses. Based on tests of a glass slide with well defined thickness and refractive index, we investigated into the time of flight formula in our system. The relationship between the temporal difference, layer thickness and refractive index was correctly established, in which a factor of the square of $\cos\theta_s$ (angle of refraction in the sample medium) was corrected. Using it we designed an experiment

to resolve the thickness of the stratum corneum in a palm. Results showed that TPI could be employed to assess the burn wounds. In another experiment, we investigated a two-layered sample and both the depth profile and the frequency dependent refractive indices of the layers were determined.

6.1.6 Characterization of fresh tissue

In Chapter 5, we presented TPI *ex vivo* results of rat tissues. By large-scale measurements of a number of healthy tissues, different parameters in both the time and frequency domains were determined. Differences in these parameters were confirmed by *t*-tests to be statistically significant. Based on this systematic study, protocols for fresh tissue measurements including tissue preparation, data acquisition, data selection and post-processing methods were investigated. Our ultimate goal is to establish TPI as a reliable tool that can be used for disease diagnosing. Thus, we further employed TPI to study infectious tissues. Refractive indices and absorption coefficients in cirrhotic livers were found to be consistently greater than those in normal livers.

6.2 Suggestions for future work

6.2.1 Further refinement of algorithms

In chapter 3, we proposed an approach to remove the baseline artefacts due to the lower surface of the quartz window. However, etaloning effects [106-108] in the quartz layer have not been accounted for in the algorithms. In addition, our algorithms for optical parameter extraction were based on the assumption that later reflections after the quartz/sample interface could not be detected. They are applicable in measurements of homogenous and strongly absorbing objects like fresh tissues with high water content. However, for samples with fine structures, for instance surface layers in the palm as shown in the feasibility study in Chapter 4, there would be multiple reflections reflected off the thin layers sample. Sometimes they superimpose to each other and consequently and can hardly be separated from each other. Therefore, more theoretical work and simulation need to be done to study this effect.

In chapter 4, when we characterized the thickness of a specified layer, we supposed the optical parameters in the first layer (the one contacted with quartz window) were independent on frequency. In this way the temporal differences could be easily obtained from the pulse shapes and the refractive index in the time-of-flight formula could be treated as a constant value. In practice, they could be dependent on frequency. Thus, this theory needs to be further improved such that it can be applied to samples with frequency dependant properties.

6.2.2 Further studies at imaging levels

This thesis has been largely focusing on refining the current techniques. The power of THz images in revealing imaging contrast has not been explored. Although raster scanning was used in our measurements, it was mostly treated as a means for collecting large data sets to remove background noises, and THz images were only created for data selection purpose. In the future, if research is successful, terahertz imaging could be used to characterize tissue properties and act as an accurate tool to determine the margins of a diseased area. Thus it would be important to systematically study data processing and analyzing methods at imaging levels.

6.2.3 Understanding the origin of differences

TPI was demonstrated to be able to characterize differences between tissues. To date, the exact reason of these differences is not clear. Although we found some clues to understand them, for example, from their different water content, structures and chemical components, they still need to be further validated. Once they can be related with histological examinations, theoretical models may be developed for clinic purposes, for example to predict the water level of a tissue or concentration of a particular chemical composition.

6.2.4 Efforts towards *in vivo* applications

To date, *in vivo* measurements have been limited to surface areas such as superficial skin. The main challenge is the strong attenuation of THz in biological objects. Improvements can be expected by building high power and high SNR THz sources. To enable the power of THz imaging in diagnosing deeper parts in the body, one

possible way would be employ TPI intra-operatively to facilitate surgeries. To this end, it is essential to develop a probe system that can access patients more easily.

6.3 Concluding remarks

THz imaging is still in its early stage of development but, as this thesis has shown, has great potential to be a valuable imaging technique in the future. In the past decade, THz imaging application in biomedical fields have drawn extensive interests and advances related to theories, experimental protocols, imaging methods and accuracy of results have been achieved. But there is still a long way to go before it can be clinically used.

References

[1] E. F. Nichols, "A method for energy measurements in the infra-red spectrum and the properties of the ordinary ray in quartz for waves of great wave length," *Physical Review (Series I),* vol. 4, pp. 297-313, 1897.

[2] H. Rubens and E. F. Nichols, "Heat rays of great wave length," *Physical Review (Series I),* vol. 4, pp. 314-323, 1897.

[3] D. H. Auston, "Picosecond optoelectronic switching and gating in silicon," *Applied Physics Letters,* vol. 26, pp. 101-103, 1975.

[4] D. M. Mittleman, M. Gupta, R. Neelamani, R. G. Baraniuk, J. V. Rudd, and M. Koch, "Recent advances in terahertz imaging," *Applied Physics B-Lasers and Optics,* vol. 68, pp. 1085-1094, 1999.

[5] X. C. Zhang, "Terahertz wave imaging: horizons and hurdles," *Physics in Medicine and Biology,* vol. 47, pp. 3667-3677, 2002.

[6] P. H. Siegel, "Terahertz technology in biology and medicine," *Ieee Transactions on Microwave Theory and Techniques,* vol. 52, pp. 2438-2447, 2004.

[7] V. P. Wallace, P. F. Taday, A. J. Fitzgerald, R. M. Woodward, J. Cluff, R. J. Pye, and D. D. Arnone, "Terahertz pulsed imaging and spectroscopy for biomedical and pharmaceutical applications," *Faraday Discussions,* vol. 126, pp. 255-263, 2004.

[8] W. Withayachumnankul, G. M. Png, X. X. Yin, S. Atakaramians, I. Jones, H. Y. Lin, B. S. Y. Ung, J. Balakrishnan, B. W. H. Ng, B. Ferguson, S. P. Mickan, B. M. Fischer, and D. Abbott, "T-ray sensing and imaging," *Proceedings of the Ieee,* vol. 95, pp. 1528-1558, 2007.

[9] E. R. Brown, K. A. Mcintosh, K. B. Nichols, and C. L. Dennis, "Photomixing up to 3.8-Thz in Low-Temperature-Grown Gaas," *Applied Physics Letters,* vol. 66, pp. 285-287, 1995.

[10] Y. U. Jeong, B. C. Lee, S. K. Kim, S. O. Cho, B. H. Cha, J. Lee, G. M. Kazakevitch, P. D. Vobly, N. G. Gavrilov, V. V. Kubarev, and G. N. Kulipanov, "First lasing of the KAERI compact far-infrared free-electron laser driven by a magnetron-based microtron," *Nuclear Instruments & Methods in Physics Research Section a-Accelerators Spectrometers Detectors and Associated Equipment,* vol. 475, pp. 47-50, 2001.

[11] J. H. Smet, C. G. Fonstad, and Q. Hu, "Intrawell and interwell intersubband transitions in multiple quantum wells for far-infrared sources," *Journal of Applied Physics,* vol. 79, pp. 9305-9320, 1996.

[12] X. C. Zhang, X. F. Ma, Y. Jin, T. M. Lu, E. P. Boden, P. D. Phelps, K. R. Stewart, and C. P. Yakymyshyn, "Terahertz optical rectification from a nonlinear organic-crystal," *Applied Physics Letters,* vol. 61, pp. 3080-3082,

1992.

[13] R. Huber, F. Tauser, A. Brodschelm, M. Bichler, G. Abstreiter, and A. Leitenstorfer, "How many-particle interactions develop after ultrafast excitation of an electron-hole plasma," *Nature,* vol. 414, pp. 286-289, 2001.

[14] H. G. Roskos, M. C. Nuss, J. Shah, K. Leo, D. A. B. Miller, A. M. Fox, S. Schmittrink, and K. Kohler, "Coherent submillimeter-wave emission from charge oscillations in a double-well potential," *Physical Review Letters,* vol. 68, pp. 2216-2219, 1992.

[15] K. McClatchey, M. T. Reiten, and R. A. Cheville, "Time resolved synthetic aperture terahertz impulse imaging," *Applied Physics Letters,* vol. 79, pp. 4485-4487, 2001.

[16] N. Karpowicz, H. Zhong, J. Z. Xu, K. I. Lin, J. S. Hwang, and X. C. Zhang, "Comparison between pulsed terahertz time-domain imaging and continuous wave terahertz imaging," *Semiconductor Science and Technology,* vol. 20, pp. S293-S299, 2005.

[17] R. H. Clothier and N. Bourne, "Effects of THz exposure on human primary keratinocyte differentiation and viability," *Journal of Biological Physics,* vol. 29, pp. 179-185, 2003.

[18] E. Berry, G. C. Walker, A. J. Fitzgerald, N. N. Zinov'ev, M. Chamberlain, S. W. Smye, R. E. Miles, and M. A. Smith, "Do in vivo terahertz imaging systems comply with safety guidelines?," *Journal of Laser Applications,* vol. 15, pp. 192-198, 2003.

[19] O. Zeni, G. P. Gallerano, A. Perrotta, M. Romanò, A. Sannino, M. Sarti, M. D'Arienzo, A. Doria, E. Giovenale, A. Lai, G. Messina, and M. R. and Scarfì, "Cytogenetic observations in human peripheral blood leukocytes following in vitro exposure to THz radiation: a pilot study," *Health Phys,* vol. 92, 2007.

[20] B. M. Fischer, M. Walther, and P. U. Jepsen, "Far-infrared vibrational modes of DNA components studied by terahertz time-domain spectroscopy," *Physics in Medicine and Biology,* vol. 47, pp. 3807-3814, 2002.

[21] S. W. Smye, J. M. Chamberlain, A. J. Fitzgerald, and E. Berry, "The interaction between Terahertz radiation and biological tissue," *Physics in Medicine and Biology,* vol. 46, pp. R101-R112, 2001.

[22] B. Ferguson and X. C. Zhang, "Materials for terahertz science and technology," *Nature Materials,* vol. 1, pp. 26-33, 2002.

[23] D. M. Mittleman, S. Hunsche, L. Boivin, and M. C. Nuss, "T-ray tomography," *Optics Letters,* vol. 22, pp. 904-906, 1997.

[24] M. Vanexter, C. Fattinger, and D. Grischkowsky, "Terahertz time-domain spectroscopy of water-vapor," *Optics Letters,* vol. 14, pp. 1128-1130, 1989.

[25] D. Grischkowsky, S. Keiding, M. v. Exter, and C. Fattinger, "Far-infrared time-domain spectroscopy with terahertz beams of dielectrics and semiconductors," *Journal of the Optical Society of America B,* vol. 7, pp. 2006-2015, 1990.

[26] B. B. Hu and M. C. Nuss, "Imaging with terahertz waves," *Optics Letters,* vol. 20, pp. 1716-&, 1995.

[27] X. C. Zhang, "Three-dimensional terahertz wave imaging," *Philosophical Transactions of the Royal Society of London Series a-Mathematical Physical and Engineering Sciences,* vol. 362, pp. 283-298, 2004.

[28] S. Hunsche, M. Koch, I. Brener, and M. C. Nuss, "THz near-field imaging," *Optics Communications,* vol. 150, pp. 22-26, 1998.

[29] H. T. Chen, R. Kersting, and G. C. Cho, "Terahertz imaging with nanometer resolution," *Applied Physics Letters,* vol. 83, pp. 3009-3011, 2003.

[30] Z. P. Jiang and X. C. Zhang, "Single-shot spatiotemporal terahertz field imaging," *Optics Letters,* vol. 23, pp. 1114-1116, 1998.

[31] A. B. Ruffin, J. Decker, L. Sanchez-Palencia, L. Le Hors, J. F. Whitaker, T. B. Norris, and J. Van Rudd, "Terahertz imaging via time reversal using single-cycle pulses," *Ultrafast Electronics and Optoelectronics, Proceedings,* vol. 49, pp. 90-92, 2001.

[32] M. Chee, R. Yang, E. Hubbell, A. Berno, X. C. Huang, D. Stern, J. Winkler, D. J. Lockhart, M. S. Morris, and S. P. A. Fodor, "Accessing genetic information with high-density DNA arrays," *Science,* vol. 274, pp. 610-614, 1996.

[33] P. H. Bolivar, M. Brucherseifer, M. Nagel, H. Kurz, A. Bosserhoff, and R. Buttner, "Label-free probing of genes by time-domain terahertz sensing," *Physics in Medicine and Biology,* vol. 47, pp. 3815-3821, 2002.

[34] Y. C. Shen, P. C. Upadhya, E. H. Linfield, and A. G. Davies, "Temperature-dependent low-frequency vibrational spectra of purine and adenine," *Applied Physics Letters,* vol. 82, pp. 2350-2352, 2003.

[35] Y. C. Shen, P. C. Upadhya, E. H. Linfield, and A. G. Davies, "Vibrational spectra of nucleosides studied using terahertz time-domain spectroscopy," *Vibrational Spectroscopy,* vol. 35, pp. 111-114, 2004.

[36] B. M. Fischer, M. Hoffmann, H. Helm, R. Wilk, F. Rutz, T. Kleine-Ostmann, M. Koch, and P. U. Jepsen, "Terahertz time-domain spectroscopy and imaging of artificial RNA," *Optics Express,* vol. 13, pp. 5205-5215, 2005.

[37] C. J. Strachan, T. Rades, D. A. Newnham, K. C. Gordon, M. Pepper, and P. F. Taday, "Using terahertz pulsed spectroscopy to study crystallinity of pharmaceutical materials," *Chemical Physics Letters,* vol. 390, pp. 20-24, 2004.

[38] J. A. Zeitler, D. A. Newnham, P. F. Taday, C. J. Strachan, M. Pepper, K. C. Gordon, and T. Rades, "Temperature dependent terahertz pulsed spectroscopy of carbamazepine," *Thermochimica Acta,* vol. 436, pp. 71-77, 2005.

[39] B. E. Cole, R. Woodward, D. Crawley, V. P. Wallace, D. D. Arnone, and M. Pepper, "Terahertz imaging and spectroscopy of human skin, in-vivo," *Proc. SPIE–Int. Soc. Opt. Eng.,* vol. 4276, pp. 1-10, 2001.

[40] E. Pickwell, B. E. Cole, A. J. Fitzgerald, M. Pepper, and V. P. Wallace, "In vivo study of human skin using pulsed terahertz radiation," *Physics in Medicine and Biology,* vol. 49, pp. 1595-1607, 2004.

[41] V. P. Wallace, A. J. Fitzgerald, E. Pickwell, R. J. Pye, P. F. Taday, N. Flanagan, and T. Ha, "Terahertz pulsed spectroscopy of human basal cell carcinoma,"

Applied Spectroscopy, vol. 60, pp. 1127-1133, 2006.

[42] A. J. Fitzgerald, V. P. Wallace, M. Jimenez-Linan, L. Bobrow, R. J. Pye, A. D. Purushotham, and D. D. Arnone, "Terahertz pulsed imaging of human breast tumors," *Radiology,* vol. 239, pp. 533-540, 2006.

[43] E. Pickwell-MacPherson, T. Lo, A. Fitzgerald, E. Provenzano, S. Pinder, A. Purushotham, and V. P. Wallace, "Application of finite difference time domain methods to terahertz spectroscopy measurements of breast cancer," in *Proc. Microwave Symposium, 2007. IEEE/MTT-S International*, 2007, pp. 1379-1381.

[44] D. Crawley, C. Longbottom, V. P. Wallace, B. Cole, D. Arnone, and M. Pepper, "Three-dimensional terahertz pulse imaging of dental tissue," *Journal of Biomedical Optics,* vol. 8, pp. 303-307, 2003.

[45] D. M. Mittleman, R. H. Jacobsen, and M. C. Nuss, "T-ray imaging," *Ieee Journal of Selected Topics in Quantum Electronics,* vol. 2, pp. 679-692, 1996.

[46] D. D. Arnone, C. M. Ciesla, A. Corchia, S. Egusa, M. Pepper, J. M. Chamberlain, C. Bezant, E. H. Linfield, R. Clothier, and N. Khammo, "Applications of Terahertz (THz) technology to medical imaging," *Terahertz Spectroscopy and Applications 11,* vol. 3828, pp. 209-219, 1999.

[47] P. Y. Han, G. C. Cho, and X. C. Zhang, "Time-domain transillumination of biological tissues with terahertz pulses," *Optics Letters,* vol. 25, pp. 242-244, 2000.

[48] P. Knobloch, C. Schildknecht, T. Kleine-Ostmann, M. Koch, S. Hoffmann, M. Hofmann, E. Rehberg, M. Sperling, K. Donhuijsen, G. Hein, and K. Pierz, "Medical THz imaging: an investigation of histo-pathological samples," *Physics in Medicine and Biology,* vol. 47, pp. 3875-3884, 2002.

[49] G. M. Png, J. W. Choi, B. W.-H. Ng, S. P. Mickan, D. Abbott, and X.-C. Zhang, "The impact of hydration changes in fresh bio-tissue on THz spectroscopic measurements," *Physics in Medicine and Biology,* vol. 53, pp. 3501-3517, 2008.

[50] H. Hoshina, A. Hayashi, N. Miyoshi, F. Miyamaru, and C. Otani, "Terahertz pulsed imaging of frozen biological tissues," *Applied Physics Letters,* vol. 94, pp. -, 2009.

[51] P. C. Ashworth, E. Pickwell-MacPherson, S. E. Pinder, E. Provenzano, A. D. Purushotham, M. Pepper, and V. P. Wallace, "Terahertz spectroscopy of breast tumors," in *Proc. Infrared and Millimeter Waves, 2007 and the 2007 15th International Conference on Terahertz Electronics. IRMMW-THz. Joint 32nd International Conference*, 2007, pp. 603-605.

[52] T. Loffler, K. Siebert, S. Czasch, T. Bauer, and H. G. Roskos, "Visualization and classification in biomedical terahertz pulsed imaging," *Physics in Medicine and Biology,* vol. 47, pp. 3847-3852, 2002.

[53] B. Ferguson, S. Wang, D. Gray, D. Abbott, and X. C. Zhang, "Identification of biological tissue using chirped probe THz imaging," *Microelectronics Journal,* vol. 33, pp. 1043-1051, 2002.

[54] R. M. Woodward, V. P. Wallace, D. D. Arnone, E. H. Linfield, and M. Pepper, "Terahertz pulsed imaging of skin cancer in the time and frequency domain," *Journal of Biological Physics,* vol. 29, pp. 257-261, 2003.

[55] E. Berry, A. J. Fitzgerald, N. N. Zinov'ev, G. C. Walker, S. Homer-Vanniasinkam, C. D. Sudworth, R. E. Miles, J. M. Chamberlain, and M. A. Smith, "Optical properties of tissue measured using terahertz pulsed imaging," *Medical Imaging 2003: Physics of Medical Imaging, Pts 1 and 2,* vol. 5030, pp. 459-470, 2003.

[56] A. J. Fitzgerald, E. Berry, N. N. Zinov'ev, S. Homer-Vanniasinkam, R. E. Miles, J. M. Chamberlain, and M. A. Smith, "Catalogue of human tissue optical properties at terahertz frequencies," *Journal of Biological Physics,* vol. 29, pp. 123-128, 2003.

[57] M. X. He, A. K. Azad, S. H. Ye, and W. L. Zhang, "Far-infrared signature of animal tissues characterized by terahertz time-domain spectroscopy," *Optics Communications,* vol. 259, pp. 389-392, 2006.

[58] S. Nakajima, H. Hoshina, M. Yamashita, C. Otani, and N. Miyoshi, "Terahertz imaging diagnostics of cancer tissues with a chemometrics technique," *Applied Physics Letters,* vol. 90, pp. -, 2007.

[59] E. M. Vartiainen, Y. Ino, R. Shimano, M. Kuwata-Gonokami, Y. P. Svirko, and K. E. Peiponen, "Numerical phase correction method for terahertz time-domain reflection spectroscopy," *Journal of Applied Physics,* vol. 96, pp. 4171-4175, 2004.

[60] R. M. Woodward, B. E. Cole, V. P. Wallace, R. J. Pye, D. D. Arnone, E. H. Linfield, and M. Pepper, "Terahertz pulse imaging in reflection geometry of human skin cancer and skin tissue," *Physics in Medicine and Biology,* vol. 47, pp. 3853-3863, 2002.

[61] A. J. Fitzgerald, E. Berry, R. E. Miles, N. N. Zinovev, M. A. Smith, and J. M. Chamberlain, "Evaluation of image quality in terahertz pulsed imaging using test objects," *Physics in Medicine and Biology,* vol. 47, pp. 3865-3873, 2002.

[62] T. Loffler, T. Bauer, K. J. Siebert, H. G. Roskos, A. Fitzgerald, and S. Czasch, "Terahertz dark-field imaging of biomedical tissue," *Optics Express,* vol. 9, pp. 616-621, 2001.

[63] E. Berry, J. W. Handley, A. J. Fitzgerald, W. J. Merchant, R. D. Boyle, N. N. Zinov'ev, R. E. Miles, J. M. Chamberlain, and M. A. Smith, "Multispectral classification techniques for terahertz pulsed imaging: an example in histopathology," *Medical Engineering & Physics,* vol. 26, pp. 423-430, 2004.

[64] B. M. Fischer, "*Broadband THz time-domain spectroscopy of biomolecules*," *PhD thesis*: *University of Freiburg*, 2005.

[65] C. Rønne, "*Intermolecular liquid dynamics studied by THz-spectroscopy*," *Ph.D thesis*: *Aarhus University*, 2000.

[66] C. Ronne, L. Thrane, P. O. Astrand, A. Wallqvist, K. V. Mikkelsen, and S. R. Keiding, "Investigation of the temperature dependence of dielectric relaxation in liquid water by THz reflection spectroscopy and molecular dynamics simulation," *Journal of Chemical Physics,* vol. 107, pp. 5319-5331, 1997.

[67] A. Poppe, L. Xu, F. Krausz, and C. Spielmann, "Noise characterization of Sub-10-fs Ti : sapphire oscillators," in *Proc. Meeting on Ultrafast Optics*, Monterey, California, 1998, pp. 179-184.

[68] L. Duvillaret, F. Garet, J. F. Roux, and J. L. Coutaz, "Analytical modeling and optimization of terahertz time-domain spectroscopy experiments using photoswitches as antennas," *Ieee Journal of Selected Topics in Quantum Electronics,* vol. 7, pp. 615-623, 2001.

[69] D. M. Mittleman, R. H. Jacobsen, and M. C. Nuss, "T-ray imaging," *Selected Topics in Quantum Electronics, IEEE Journal of,* vol. 2, pp. 679-692, 1996.

[70] G. Zhao, R. N. Schouten, N. van der Valk, W. T. Wenckebach, and P. C. M. Planken, "Design and performance of a THz emission and detection setup based on a semi-insulating GaAs emitter," *Review of Scientific Instruments,* vol. 73, pp. 1715-1719, 2002.

[71] S. Jay and R. C. Alan, "Noise reduction in THz systems using THz interferometry," in *Proc. Conference on Lasers and Electro-Optics/International Quantum Electronics Conference and Photonic Applications Systems Technologies*, 2004.

[72] B. Ferguson and D. Abbott, "De-noising techniques for terahertz responses of biological samples," *Microelectronics Journal,* vol. 32, pp. 943-953, 2001.

[73] M. Naftaly and R. Dudley, "Methodologies for determining the dynamic ranges and signal-to-noise ratios of terahertz time-domain spectrometers," *Optics Letters,* vol. 34, pp. 1213-1215, 2009.

[74] P. U. Jepsen and B. M. Fischer, "Dynamic range in terahertz time-domain transmission and reflection spectroscopy," *Optics Letters,* vol. 30, pp. 29-31, 2005.

[75] P. U. Jepsen, J. K. Jensen, and U. Møller, "Characterization of aqueous alcohol solutions in bottles with THz reflectionspectroscopy," *Opt. Express,* vol. 16, pp. 9318-9331, 2008.

[76] C. Ronne and S. R. Keiding, "Low frequency spectroscopy of liquid water using THz-time domain spectroscopy.," *Journal of Molecular Liquids,* vol. 101, pp. 199-218, 2002.

[77] E. Pickwell, B. E. Cole, A. J. Fitzgerald, V. P. Wallace, and M. Pepper, "Simulation of terahertz pulse propagation in biological systems," *Applied Physics Letters,* vol. 84, pp. 2190-2192, 2004.

[78] V. P. Wallace, E. MacPherson, J. A. Zeitler, and C. Reid, "Three-dimensional imaging of optically opaque materials using nonionizing terahertz radiation," *J. Opt. Soc. Am. A,* vol. 25, pp. 3120-3133, 2008.

[79] J. Pearce, H. Choi, D. M. Mittleman, J. White, and D. Zimdars, "T-ray reflection computed tomography," *2005 Conference on Lasers & Electro-Optics (CLEO), Vols 1-3,* pp. 2120-2122, 2005.

[80] J. Pearce, H. Choi, D. M. Mittleman, J. White, and D. Zimdars, "Terahertz wide aperture reflection tomography," *Opt. Lett.,* vol. 30, pp. 1653-1655, 2005.

[81] U. F. Administration, "http://www.usfa.dhs.gov/statistics/quickstats/index.sh

tm."

[82] M. I. Liddington and P. G. Shakespeare, "Timing of the thermographic assessment of burns," *Burns,* vol. 22, pp. 26-28, 1996.

[83] J. M. Still, E. J. Law, K. G. Klavuhn, T. C. Island, and J. Z. Holtz, "Diagnosis of burn depth using laser-induced indocyanine green fluorescence: a preliminary clinical trial," *Burns,* vol. 27, pp. 364-371, 2001.

[84] F. W. H. Kloppenberg, G. I. J. M. Beerthuizen, and H. J. ten Duis, "Perfusion of burn wounds assessed by Laser Doppler Imaging is related to burn depth and healing time," *Burns,* vol. 27, pp. 359-363, 2001.

[85] L. Devgan., S. Bhat., S. Aylward., and R. Spence., "Modalities for the assessment of burn wound depth," *J Burns Wounds.,* vol. 5, pp. 7-15, 2006.

[86] Z. D. Taylor, R. S. Singh, M. O. Culjat, J. Y. Suen, W. S. Grundfest, H. Lee, and E. R. Brown, "Reflective terahertz imaging of porcine skin burns," *Opt. Lett.,* vol. 33, pp. 1258-1260, 2008.

[87] M. Egawa, T. Hirao, and M. Takahashi, "In vivo estimation of stratum corneum thickness from water concentration profiles obtained with Raman spectroscopy," *Acta Dermato-Venereologica,* vol. 87, pp. 4-8, 2007.

[88] L. Thrane, R. H. Jacobsen, P. Uhd Jepsen, and S. R. Keiding, "THz reflection spectroscopy of liquid water," *Chemical Physics Letters,* vol. 240, pp. 330-333, 1995.

[89] R. M. Woodward, V. P. Wallace, R. J. Pye, B. E. Cole, D. D. Arnone, E. H. Linfield, and M. Pepper, "Terahertz Pulse Imaging of ex vivo Basal Cell Carcinoma," vol. 120, pp. 72-78, 2003.

[90] M. Bruehlmeier, U. Roelcke, P. Blauenstein, J. Missimer, P. A. Schubiger, J. T. Locher, R. Pellikka, and S. M. Ametamey, "Measurement of the extracellular space in brain tumors using 76Br-Bromide and PET." vol. 44, 2003, pp. 1210-1218.

[91] E. K. Rofstad, E. Steinsland, O. Kaalhus, Y. B. Chang, B. Hovik, and H. Lyng, "Magnetic-resonance-imaging of human-melanoma xenografts in-vivo - proton spin-lattice and spin-spin relaxation-times versus fractional tumor water-content and fraction of necrotic tumor-tissue," *International Journal of Radiation Biology,* vol. 65, pp. 387-401, 1994.

[92] S. Y. Huang, E. MacPherson, and Y. T. Zhang, "A new data processing approach to reduce variations in terahertz pulsed imaging," in *Proc. 5th International Summer School and Symposium on Medical Devices and Biosensors*, 2008, pp. 243-245.

[93] M. DiGirolamo and J. L. Owens, "Water content of rat adipose tissue and isolated adipocytes in relation to cell size." vol. 231, 1976, pp. 1568-1572.

[94] J. M. Peters and E. M. Boyd, "Organ weights and water levels of rat following reduced food intake," *Journal of Nutrition,* vol. 90, pp. 354-&, 1966.

[95] R. L. Shirley, D. D. Hargrove, F. Palting, J. F. Easley, J. W. Carpenter, and M. Koger, "Water, phosphorus, calcium, ash and protein of the heart, liver and muscle of hereford, brahman and hereford-brahman cross-bred cattle." vol.

22, 1963, pp. 393-395.

[96] Y. Watanabe, K. Kawase, T. Ikari, H. Ito, Y. Ishikawa, and H. Minamide, "Component spatial pattern analysis of chemicals using terahertz spectroscopic imaging," *Applied Physics Letters,* vol. 83, pp. 800-802, 2003.

[97] D. Bigourd, A. Cuisset, F. Hindle, S. Matton, R. Bocquet, G. Mouret, F. Cazier, D. Dewaele, and H. Nouali, "Multiple component analysis of cigarette smoke using THz spectroscopy, comparison with standard chemical analytical methods," *Applied Physics B: Lasers and Optics,* vol. 86, pp. 579-586, 2007.

[98] P. U. Jepsen, U. Møler, and H. Merbold, "Investigation of aqueous alcohol and sugar solutions with reflection terahertz time-domain spectroscopy," *Opt. Express,* vol. 15, pp. 14717-14737, 2007.

[99] F. X. Bosch, J. Ribes, M. Diaz, and R. Cleries, "Primary liver cancer: Worldwide incidence and trends," *Gastroenterology,* vol. 127, pp. S5-S16, 2004.

[100] U. C. Nzeako, Z. D. Goodman, and K. G. Ishak, "Hepatocellular carcinoma in cirrhotic and noncirrhotic livers - A clinico-histapathologic study of 804 North American patients," *American Journal of Clinical Pathology,* vol. 105, pp. 65-75, 1996.

[101] J. M. Llovet, J. Fuster, J. Bruix, and B. C. L. C. Grp, "Intention-to-treat analysis of surgical treatment for early hepatocellular carcinoma: Resection versus transplantation," *Hepatology,* vol. 30, pp. 1434-1440, 1999.

[102] M. Lanthaler, M. Biebl, A. Weissenbacher, R. Margreiter, and H. Nehoda, "Recurrence after liver resection for hepatocellular carcinoma in cirrhotic and noncirrhotic patients," *Chirurgische Gastroenterologie,* vol. 24, pp. 51-54, 2008.

[103] A. P. O'Rourke, M. Lazebnik, J. M. Bertram, M. C. Converse, S. C. Hagness, J. G. Webster, and D. M. Mahvi, "Dielectric properties of human normal, malignant and cirrhotic liver tissue: in vivo and ex vivo measurements from 0.5 to 20 GHz using a precision open-ended coaxial probe," *Physics in Medicine and Biology,* vol. 52, pp. 4707-4719, 2007.

[104] S. Y. Huang, Y. X. J. Wang, D. K. WYeung, A. T. Ahuja, Y. T. Zhang, and E. Pickwell-MacPherson, "Tissue characterization using terahertz pulsed imaging in reflection geometry," *Physics in Medicine and Biology,* vol. 54, pp. 149-160, 2009.

[105] V. Velebny, E. Kasafirek, and J. Kanta, "Desmosine and isodesmosine contents and elastase activity in normal and cirrhotic rat-liver," *Biochemical Journal,* vol. 214, pp. 1023-1025, 1983.

[106] W. Withayachumnankul, B. Ferguson, T. Rainsford, S. Mickan, and D. Abbott, "Direct Fabry-Perot effect removal," *Fluctuation and Noise Letters,* vol. 6, pp. L227-L239, 2006.

[107] T. D. Dorney, R. G. Baraniuk, and D. M. Mittleman, "Material parameter estimation with terahertz time-domain spectroscopy," *Journal of the Optical Society of America A,* vol. 18, pp. 1562-1571, 2001.

[108] M. Naftaly and R. E. Miles, "A method for removing etalon oscillations from THz time-domain spectra," *Optics Communications,* vol. 280, pp. 291-295, 2007.